Charged Colloids and Interfaces: Interaction and Phase Behaviour

Dissertation

zur Erlangung des akademischen Grades
"Doktor der Naturwissenschaften" (Dr. rer. nat.)
an der Universität Konstanz
Fachbereich Physik

vorgelegt von

Emmanuel Chinedu Mbamala

Konstanz, 2002

Datum der mündlichen Prüfung: 20.02.2003

Referent: Herr PD Dr. H.H. von Grünberg
Referent: Herr Prof. Dr. W. Dieterich

Zusammenfassung

Die vorliegende Arbeit untersucht geladene, kugelförmige Teilchen (Kolloide oder Makroionen) in einer Suspension zusammen mit kleinen Ionen (Mikroionen). Diese Suspensionen grenzen an Substrate mit oftmals anderer Dielektrizitätskonstante als die der Suspension. Wir betrachten dabei hauptsächlich die Wechselwirkung der Kolloide mit der Grenzfläche (Wand-Kolloid-Potential), sowie die Wechselwirkung der Kolloide untereinander (Kolloid-Kolloid-Potential) in Anwesenheit von verschiedenen Grenzflächen. Ausgehend von diesen Wechselwirkungen untersuchen wir Struktur und Phasenverhalten von Kolloiden an einer Grenzfläche. Dazu benutzen wir die Poisson-Boltzmann (PB) Theorie und Monte-Carlo-Simulationen. Unsere Ergebnisse können wir wie folgt zusammenfassen:

Ausgehend von der linearisierten PB-Theorie für eine punktförmige Ladung nahe einer Grenzfläche, betrachten wir effektive Wand-Kolloid-Potentiale für ein System von Makroionen in einer mikroionischen Lösung der Dielektrizitätskonstante ϵ und der Abschirmkonstante κ, sowie einer dielektrischen Wand mit der Konstanten ϵ'. Durch Renormalisierung der Gesamtladung Z des Kolloids berücksichtigen wir seine endliche Größe. Besondere Beachtung finden hierbei sog. "confinement" Effekte, also Effekte, die durch die räumliche Einschränkung durch die Wand verursacht werden, und Bildladungseffekte, die durch Sprünge der Dielektrizitätskonstante an der Wand hervorgerufen werden. Mit Hilfe der exakten Gouy-Chapman-Lösung für einen Elektrolyten vor einer geladenen Wand und den Potentialen, die im Rahmen der linearen Theorie gewonnen wurden, können wir näherungsweise Wand-Kolloid-Potentiale erhalten, die in einem gewissen Parameterbereich Gültigkeit haben, in dem die Nichtlinearität der PB-Gleichung wichtig wird. Die Gültigkeitsbereiche für die verschiedenen Parameter dieser Potentiale werden systematisch untersucht, indem wir sie mit Potentialen vergleichen, die durch exakte numerische Simulation der PB-Gleichung erhalten worden sind. Die Messbarkeit der genäherten effektiven Potentiale wird demonstriert

durch einen Vergleich mit einem TIRM (Total internal reflection microscopy) Experiment, wo gute Übereinstimmung gefunden werde. Sowohl für ungeladene als auch für geladene feste Wände mit $\epsilon' \leq \epsilon$ ist das effektive Wand-Kolloid-Potential für alle Abstände des Kolloids von der Wand immer repulsiv. Ein Zellenmodell mit der nichtlinearen PB-Theorie für eine kolloidale Suspension vor einer ungeladenen Wand zeigt jedoch, dass im selben Fall ($\epsilon' \leq \epsilon$) ein Ungleichgewicht zwischen echter Ladung und Bildladung des Systems zu einer netto attraktiven Kraft auf das Kolloid führen kann. Unser Zellenmodell zeigt weiterhin, dass die effektive Ladung der Makroionen in der Nähe der Wand reduziert wird.

Wenn wir uns nun an einer Luft-Wasser-Grenzfläche befinden, kann das Kolloid in die "Wand" eindringen. Wir zeigen, dass das effektive Wand-Kolloid-Potential, welches eine elektrostatische Barriere für die Adsorption eines Kolloids aus der Lösung an die Grenzfläche darstellt, durch Erhöhung der Salzkonzentration beträchtlich verringert werden kann. Dies kann ein Einfangen der Kolloide an der Luft-Wasser-Grenzfläche einleiten. Wir zeigen allerdings auch, dass dieses "trapping" an der Grenzfläche eher durch die Oberflächenspannung als durch die Elektrostatik dominiert wird.

Für die Luft-Wasser-Grenzfläche betrachten wir im Rahmen der linearen Debye-Hückel-Theorie die Paarpotentiale geladener Kolloide, die an dieser Grenzfläche gefangen sind. Wir zeigen, dass eine zusätzliche Substrat-Grenzfläche, parallel und sehr nah an der Luft-Wasser-Grenzfläche, die Paarwechselwirkung in einer bestimmten Art und Weise beeinflussen kann, die von der Dielektrizitätskonstante des Substrats relativ zu der von Wasser abhängt. Anschliessend verwenden wir die Paarpotentiale in einer Ein-Komponenten Monte-Carlo-Simulation, um ein Flüssig–Fest Phasendiagramm in der $[L : \phi_{\text{surf}}]$-Parameterebene zu erhalten. L ist dabei der Abstand zwischen den Grenzflächen und ϕ_{surf} ist der Bedeckungsgrad der Kolloide. Als wichtigstes Ergebnis ergibt sich dabei: Ein Substrat, dessen dielektrische Konstante sehr viel kleiner ist, als die des Lösungsmittels, z. B. Luft, verstärkt die repulsive Paarwechselwirkung und führt bei abnehmendem L dementsprechend zu einer Kristallisation bei Dichten, bei denen in Abwesenheit des Substrats das System in flüssiger Form vorliegt. Ein Substrat, dessen dielektrische Konstante hingegen sehr viel grösser ist als die des Lösungsmittels, z.B. ein Metall, verhält sich gerade umgekehrt. Wir erweitern unsere Untersuchungen auf Parameterbereiche, die passend für globuläre Proteine sind, mit dem Ergebnis, dass ein Substrat vom erstem Typ ($\epsilon' \ll \epsilon$) nur dann einen positiven Einfluss auf die Kristallisation hat, wenn L sehr klein wird, d. h. von derselben Grössenordnung, wie die Proteingrösse, und die Bedeckungsgrade zudem sehr hoch sind.

Abschliessend diskutieren wir den Gültigkeitsbereich unserer verschiedenen Studien und zeigen zukünftige Entwicklungsmöglichkeiten auf.

Summary

This thesis presents studies concerned with the effects on charged colloidal spherical particles (colloids or macroions) suspended in solutions of small ions (microions), due to the presence of interfacial substrates which often have different dielectric constants as that of the suspension. We consider mainly, interaction potentials of these colloids with the interfacial walls (wall–colloid potentials) and also interactions among themselves (colloid–colloid potentials) in the presence of one or more similar or dissimilar interfaces. We also investigate the structural and phase behaviour of these interfacial colloids, resulting from the interaction potentials. As tools for these studies, we work within the framework of Poisson-Boltzmann (PB) theories and Monte-Carlo (MC) simulations. The various studies and results can be summarized as follows:

Starting from the linearized PB theory for a point-charge near an interface, we first consider effective wall–colloid potentials for a system of a macroion in a microionic solution of dielectric constant ϵ and screening constant κ, and a charged or uncharged dielectric planar wall of dielectric constant ϵ'. The finite size of the colloidal macroion is then accounted for, by a renormalization of the macroion total charge Z. We emphasize the role of confinement and image-charge effects due to the spatial and dielectric discontinuities introduced by the wall. Using the Gouy-Chapman exact solution for an aqueous electrolyte next to a charged wall and potentials derived in the linear theory, we obtain approximate wall–colloid potentials that are valid also in some parameter regime where the non-linearity of the PB equation becomes important. The range of validity in the various system parameters of these potentials are systematically investigated by comparing them with potentials based on the exact numerical solution of the PB equation. The measurability of the approximate effective potentials is demonstrated by comparison with a TIRM (Total internal reflection microscopy) experiment with good agreement. For both neutral and charged hard walls, for which $\epsilon' \leq \epsilon$, the effective wall–colloid potential is always repulsive for all wall–colloid separation distances. A non-linear PB cell model scheme for a colloidal suspension near a neutral hard wall, however, shows that for the same case ($\epsilon' \leq \epsilon$), an imbalance between the real and image charges of the system can lead to a net attractive force on the colloid due to the interfacial wall. Our cell model methods further reveal that the effective charge of colloidal macroions is reduced near a dielectric wall.

When the interfacial wall is an air-water interface the colloid can penetrate the wall. We show that the effective wall–colloid repulsive potential which constitutes an electrostatic barrier to adsorption of the macroion from the bulk to the interface can be lowered considerably by increased salt concentration. This can initiate trapping of the colloid at the air-water interface. We show also that the trapping is however

dominated by surface tension forces rather than electrostatics.

Still on air-water interface, we consider, within the linear Debye-Hückel theory, the pair interaction potentials of charged colloidal particles assumed trapped at this interface. We show that introducing additional substrate interfaces parallel and very close to the air-water interface can affect the pair potentials in a particular way, depending on the dielectric constant of the substrate relative to water. We then apply the pair potentials in a *one-component* Monte-Carlo simulation to obtain fluid – crystal phase diagrams in the $[L : \phi_{\text{surf}}]$ parameter plane, where L is the separation distance between the two interfaces and ϕ_{surf} is the surface fraction of the interfacial colloids. The main result is as follows: A substrate whose dielectric constant is much smaller than that of the solvent, e.g. air, enhances the repulsive pair interaction, and consequently induces crystallization with decreasing L at densities where the system particles exhibit fluid order in the absence of the substrate. A substrate whose dielectric constant is much larger than that of the solvent, e.g. metal, behaves in the opposite way. We extend the investigation to parameters appropriate for globular proteins with the result that the substrate, even if of the former type can facilitate crystallization only when L becomes very thin, being comparable to the protein particle size, and at much higher surface fractions.

Finally, we identify some shortcomings of the various studies and suggest possible ways to improvement in future studies.

Contents

List of abbreviations

Abbreviation	Definition (*Remark*)	Reference
AFM	Atomic force microscope	P. 66
AWA	Air-water-air (*system of interfaces*)	P. 81
AWM	Air-water-metal	P. 81
AWW	Air-water-water	P. 81
AW	Air-water (*only*)	P. 81
BS	Bulk scheme	P. 113, Fig. 5.5
BSC	Bispherical coordinate (*system*)	P. 17
BVP	Boundary value problem	P. 15
DH	Debye-Hückel	
DLVO	Dejaguin-Landau-Verwey-Overbeek (*potential*)	
IS	Interface scheme	P. 113, Fig. 5.5
MBP	Many-body primitive (*model*)	P. 101
MC	Monte-Carlo	
MD	Molecular dynamics	
NVT	(*constant*) Number, Volume and Temperature	
PB	Poisson-Boltzmann	
TIRM	Total internal reflection microscopy	P. 7, P. 44
TOC	Toroidal coordinate (*system*)	
TSC	Tangent-sphere coordinate (*system*)	
2D	Two-dimensional	

x

List of symbols

Symbol	Definition	Reference
a	Radius of a colloidal particle	Fig. 2.1
b	A length scale in the BSC and TOC systems	eq. (2.6)
c_s	Bulk salt concentration	eq. (1.4)
d_c	Counterion diameter	eq. (5.22)
d_m	Macroion diameter	eq. (5.22)
e	The elementary charge	
E_s	Surface energy	eq. (3.14)
$\vec{F}$	Vector force on a colloidal particle	eq. (2.55)
g_∞	DH charge renormalization factor in the bulk	eq. (2.32)
g_h	DH charge renormalization factor close to the wall	eq. (2.35)
$g(r)$	Pair correlation function (2D)	eq. (4.29)
$g_B(r)$	Bond-orientational correlation function	eq. (4.30)
G	Region of the aqueous electrolyte half-space	Fig. 2.1, eq. 2.1
$G_<$	Region of the dielectric substrate half-space	Fig. 2.1, eq. 2.1
∂G_c	The colloid-electrolyte boundary surface	Fig. 2.1, eq. 2.1
∂G_w	The wall-electrolyte boundary surface	Fig. 2.1, eq. 2.1
h	Wall–colloid separation distance	Fig. 2.1
$\tilde{h}$	$(= h/a)$ Reduced wall–colloid separation distance	P. 59
$\vec{\vec{I}}$	Unit tensor	eq. (2.56)
L	The air-water-substrate separation distance	Fig. 4.1
k_B	Boltzmann constant	
$\mathbf{n}_c$	Unit outward normal vector: colloid	eq. 2.1, Fig. 2.1
$\mathbf{n}_w$	Unit outward normal vector: wall (interface)	eq. 2.1, Fig. 2.1
$\vec{\vec{T}}$	Stress tensor	eq. (2.55), eq. (2.55)
T	The absolute temperature	
U^i	Pair potential of system i, $i \equiv$ AW, AWM, etc.	Chapter 4: eq. (4.16)
U	Total configurational internal energy	Chapter 5: eq. (5.20)
v_{vdw}	van-der-Waals interaction potential	eq. (1.1)
$V(h)$	Interaction potential	eq. (3.2)
V_{DJG}	Derjaguin-based effective interaction	eq. (2.52)
V_{GCH}	Gouy-Chapmann-based effective interaction	eq. (2.51)
V_{LIN}	Interaction in purely linear theory	eq. (2.46)
V_{St}	Interaction for uncharged wall in linear theory	eq. (2.26)
V_{ad}	Adsorption barrier	eq. (3.12)
V_{de}	Desorption barrier	eq. (3.13)
Z	Total number of elementary charges	Fig 2.1
Z_h	Z as function of interface–colloid distance h	Fig. 3.3, eq. 3.7
Z^*	Effective charge	eq. (5.29)

Symbol	Definition	Reference
β	$(= 1/k_BT)$ The thermal energy	eq. (1.4)
χ	Coupling between two dielectric media	eq. (2.18)
$\tilde{\chi}$	-do-	eq. (2.17)
$\tilde{\chi}_{12}$	-do-	eq. (4.12)
$\tilde{\chi}_{32}$	-do-	eq. (4.13)
ΔA	Free energy difference	eq. (5.30)
ΔU	Internal energy difference	Fig. 5.7
ϵ, ϵ'	Water and substrate dielectric constants	Chapters 2, 3 & 5
ϵ_1, ϵ_2, ϵ_3	Air, water and substrate dielectric constants	Chapter 4
ϕ, ϕ_h	The normalized electrical potential	eq. (1.4),eq. (2.11)
ϕ^{GC}	Gouy-Chapmann potential	eq. (2.4)
ϕ_{surf}	Surface fraction of macroions	P. 87
ϕ_{vol}	Volume fraction of macroions	eq. (5.6)
Φ_c	Colloid surface potential	eq. (2.47)
Φ_w	Wall surface potential	eq. (2.48)
Φ_6	Bond orientational order parameter	eq. (4.28)
γ_c, γ_w	Relating to Φ_c and Φ_w respectively	eq. (2.49)
γ_{aw}	Air–water surface tension	eq. (3.14)
γ_{pw}, γ_{pa}	Particle–water and particle–air surface tensions	eq. (3.14)
κ	The inverse screening length	eq. (1.8)
$\tilde{\kappa}$	κa	eq. (3.17), P. 59
λ_B	Bjerrum length	eq. (1.9)
$\tilde{\lambda}_B$	λ_B/a	P. 59, eq. (5.7)
Λ_T	The thermal wavelength	P. 20
Λ	Coulomb coupling parameter	eq. (4.27)
μ_s	Electrolyte ions chemical potential	P. 15
Π	Osmotic pressure	eq. (2.56)
ρ	Volume charge density per charge, e	eq. (1.3), eq. (5.1)
σ	Colloid surface charge density per charge e	Fig. 3.1, eq. (3.1)
$\tilde{\sigma}$	Reduced colloid surface charge density	P.59, eq. (5.7)
σ_c	Colloid surface charge density per charge e	eq. (2.1)
σ_w	Wall surface charge density per e	eq. (2.1)
ς_c	Reduced colloid surface charge density	eq. (2.2)
ς_w	Reduced wall surface charge density	eq. (2.2)
Ω, Ω_h	The grand potential	eq. (2.9)
ψ	Electrical potential	eq. (1.2)
ψ_6	Local bond-orientational order parameter	eq. (4.30)
Ψ	Eigenfunctions	eq. (4.6)

1

General introduction

1.1. Colloid basics

Suspensions or solutions of colloidal particles have been described by Overbeek [1] as the *world of neglected dimensions*. In a colloidal suspension, the solute particles (also referred frequently here as colloids) are sufficiently small not to be affected significantly by gravitational forces but large enough compared to the solvent molecules. The size range of colloidal particles have been set arbitrarily as $\sim$ 1nm (10^{-9}m) to $\sim$ 10μm (10^{-5}m). The much larger size of colloidal particles and as a result much lower number concentration relative to particles in ordinary solutions lead to the marked deviations in properties of the former from the latter type of solutions. They include, very low osmotic pressures, very low solute diffusion coefficients, and very low freezing point depressions. In addition, colloids do not pass through dialysis membranes and the solutions are often turbid and scatter light.

Colloidal suspensions exist in great varieties. Some common examples are: paints pigments in an organic solvent, casein agglomerates in milk, clay platelets in a river, soap in water, e.t.c. Colloids find many applications in both basic science and technology. Brownian motions, light scattering, long range forces (e.g. electrostatic and van-der-Waals forces), nucleation, crystal growth, bio-chemical systems (e.g. DNA, RNA, proteins, membranes), fractals, e.t.c, are some areas of research that have benefited from studies in colloid science. The industrial importance of colloids arises from the fact that many products are colloidal suspensions or derivatives of colloidal suspensions. They are found in many chemical, pharmaceutical, food and cosmetics products, e.g., paints, magnetic-tapes, micro-emulsions, dairy products, foams,detergents etc.

1.2. Colloidal stabilization and phases

Particles in colloidal suspension can be made to exhibit various phases, from dilute *gas* to *solid* crystal, analogous to phases in atomic or simple molecular systems. The much slower dynamics to equilibrium, of the colloidal particles compared to atoms or molecules in the ordinary systems makes it possible for direct experimental investigation of structural and phase changes in colloidal suspensions, such as nucleation, crystallization, clustering, aggregation, e.t.c. These phases and orders can easily be obtained by the combination of the effects of varying particles densities, strength and range of the interaction potentials between the particles.

The most basic interaction potential between all types of colloidal particles is that related to the van-der-Waals forces, whose origin is due to fluctuating dipoles in neutral bodies [2, 3]. The van-der-Waals interaction potential between two spherical particles of diameter σ whose centers are separated by a distance r is given by, [4]

$$v_{\mathrm{vdW}}(r) = -\frac{A}{12}\left[\frac{\sigma^2}{r^2-\sigma^2} + \left(\frac{\sigma}{r}\right)^2 + 2\ln\left(1-\frac{\sigma^2}{r^2}\right)\right] \quad ; r > \sigma \tag{1.1}$$

The strength of this is given by the Hamaker constant A which depends on the dielectric functions of the particles and the solvent. The potential $v_{\mathrm{vdW}}(r)$ varies as $-r^{-6}$ at large distances and as $-(r-\sigma)^{-1}$ as r becomes comparable with the diameter σ, where it develops a deep minimum.

A system where the van-der-Waals interactions are the only dominant forces will eventually lead to aggregation, flocculation or coagulation and eventual settling of the particles. Therefore other compensating repulsive interaction forces are needed to stabilize the suspension. To this end, two methods (and a combination of the two) are commonly employed, namely charge and steric stabilization (see Figs 1.1 and 1.2). In the latter method, short polymer brushes are adsorbed on the colloids' surfaces dispersed usually in apolar solvents (Fig. 1.1). The brushes cause short range repulsions between the particles, which may balance or exceed the van-der-Waals attractions.

In charge stabilized systems, the colloidal particles have or can be made to have ionizable surface groups. In a polar solvent (e.g. water), they aquire net surface charges and a large number of counterions (microions) are released into the solution to form a layer of charges around each particle (Fig. 1.2). This layer charges and the colloidal surface charges constitute what is frequently called the electric double layer (EDL). The EDL results in long-range electrostatic repulsive forces that keep distances between the charged colloids outside the range of the van-der-Waals attractive dispersion forces. Ref. [2] is strongly recommended for a comprehensive theory of the EDL. In general, the stability of charged colloids in aqueous media is highly sensitive

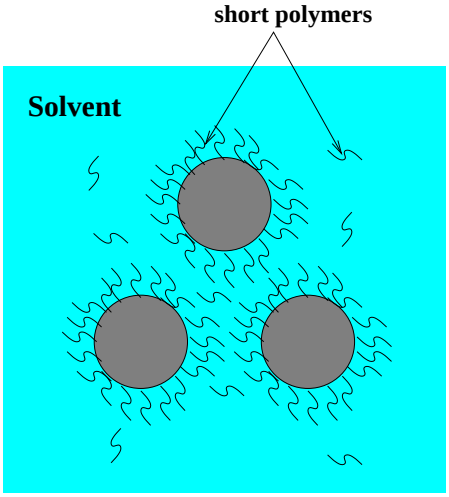

Figure 1.1: Steric stabilization: short polymer brushes are formed around the colloid particles which prevent the particles from coming too close together.

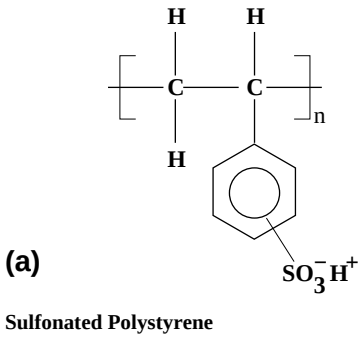

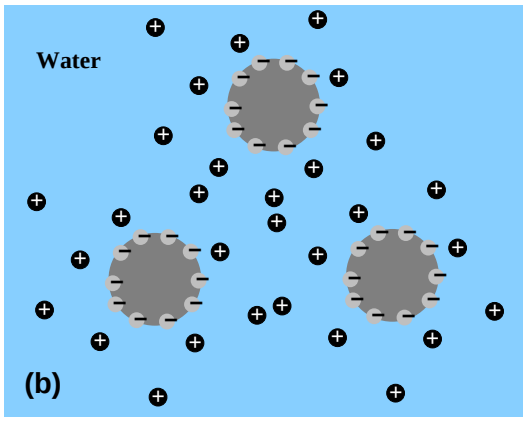

Figure 1.2: Charge stabilization: (a) A sulfonated polystyrene of n-monomers with the ionizable surface group, SO_3H. Polystyrene particles have very high monodispersity and are used very frequently in colloid experiments. (b) In a polar solvent such as water, the surface group dissociates leaving fixed SO_3^- on the particle surface and releasing H^+ as mobile counterions.

to the presence of added electrolytes (e.g. salt ions). Addition of electrolytes have been known to cause coagulation and flocculation followed by settling in an otherwise stable suspension. Although in most applications undesirable, salting effects has been used to study aggregation kinetics and the resulting fractal shapes of the aggregates. We will also show, as part of the work in this thesis that near dielectric interfaces such as the air-water, addition of electrolytes can initiate trapping of colloid particles at the interface, useful for studies in two-dimensions.

The present thesis is concerned mainly with systems of charge stabilized colloidal suspension for a number problems relating to this type of colloids. A major tool used throughout the studies here is the Poisson-Boltzmann (PB) equation which is the starting point of the theories of the EDL, and hence the need to introduce it in the next section.

1.3. The Poisson-Boltzmann equation and theories

The basic equation for the determination of the electrical properties of a system of charges in a medium of uniform dielectric constant, ϵ is the Poisson equation which states that;

$$\nabla^2\psi(\mathbf{r}) = -\frac{4\pi\varrho(\mathbf{r})}{\epsilon}, \tag{1.2}$$

where $\psi(\mathbf{r})$ is the local electrical potential at a point $\mathbf{r}$ from an arbitrary origin, $\varrho(\mathbf{r})$ is the local charge density for a system of M ionic species,

$$\varrho(\mathbf{r}) = \sum_i^M ez_i\rho_i(\mathbf{r}) \tag{1.3}$$

where for each ion type i, $\rho_i(\mathbf{r})$ is the charge density per unit elementary charge, e, z_ie is the charge on an ion with z_i the number (valency with $\pm$ sign) of the unit charges. $\epsilon(\mathbf{r})$ is the local dielectric constant of the medium.

The space charge is formed, if e.g., a reference charge is taken as positive, by an excess of negative ions attracted and accumulated in the neighbourhood of the ion, while inversely, the positive ions are repelled and pushed away from it. The effect of these electric forces is counteracted by the random thermal motion of the ions, which gives the diffuse charge layer its spatial extension. In order to take this thermal equilibrium into consideration, the concentrations ρ_i are expressed as Boltzmann distributions, where it is assumed that $\rho_i(\mathbf{r})$ at a given point can be calculated from the average value of the electric potential $\psi(\mathbf{r})$ at the same point, thus;

$$\rho_i(\mathbf{r}) = c_s\mathrm{e}^{-z_i\phi(\mathbf{r})}, \tag{1.4}$$

where c_s is the bulk ion (salt) concentration, $\phi = e\beta\psi$ is the normalized electrical potential with $\beta = 1/k_BT$ the inverse thermal energy; k_B being the Boltzmann constant and T, the absolute temperature. Substituting eq. (1.4) in eq. (1.2) we obtain the Poisson-Boltzmann (PB) equation:

$$\nabla^2\phi(\mathbf{r}) = -\frac{4\pi\beta e^2}{\epsilon}\sum_i^M c_sz_i\mathrm{e}^{-z_i\phi(\mathrm{r})} \tag{1.5}$$

The assumption that we can describe the actual bulk charge distribution in terms of the average potential $\phi(\mathbf{r})$ makes the PB equation an example of a mean field approximation.

It is expedient to consider only monovalent symmetric electrolytes where $z_+ = +1$ and $z_- = -1$. Then the summation in eq. (1.5) is simply,

$$\begin{aligned} \textstyle\sum_{i=\pm} c_s z_i \mathrm{e}^{-z_i\phi(\mathbf{r})} &= c_s \mathrm{e}^{-\phi(\mathbf{r})} - c_s \mathrm{e}^{+\phi(\mathbf{r})} \\ &= \rho_+ - \rho_- = -2\sinh\phi(\mathbf{r}). \end{aligned} \tag{1.6}$$

Using eq. (1.6) in eq. (1.5) we obtain,

$$\nabla^2\phi(\mathbf{r}) = \kappa^2 \sinh\phi(\mathbf{r})\,. \tag{1.7}$$

$$\kappa^2 = 8\pi c_s \lambda_B\,, \tag{1.8}$$

where κ is the Debye screening constant and

$$\lambda_B = e^2\beta/\epsilon \tag{1.9}$$

is the Bjerrum length, defined as the distance at which the interaction between two unit charges is $1/\beta$. The bulk dielectric constant ϵ has been employed instead of the local $\epsilon(\mathbf{r})$. Equation (1.7) is the form of the non-linear PB equation used in most of the work reported in this thesis. The fixed charges, e.g. charges of a colloidal particle or a wall surface enter the problem through the boundary conditions specific for the particular problem, as we see in the following chapters.

If the electric potential is so small that $\phi(\mathbf{r})$ is everywhere much smaller than one, eq. (1.7) may be linearized by expanding the sine hyperbolic function up the linear term in ϕ to get,

$$\nabla\phi(\mathbf{r}) = \kappa^2\phi(\mathbf{r}). \tag{1.10}$$

Equation (1.10) is the well known starting point in the Debye-Hückel (DH) theory for strong electrolytes which deals with the calculation of the electric potential in the ionic atmosphere around a reference ion. However, very close to a highly charged colloidal particle where $\phi \gg 1$, the use of eq. (1.10) becomes a highly questionable approximation. Nevertheless, eq. (1.10) has continued to find relevance in problems of charged colloids, especially since the *bare charge* of a colloidal particle can be renormalized to a much smaller *effective charge*. [5]

In most of the problems investigated in the present work, eqs (1.7) and (1.10) along with the appropriate boundary conditions form various sets of boundary value problems (BVP) which have been solved in most cases by numerical methods and in some cases analytically with tolerable approximations. In some cases we have also employed conventional Monte-Carlo (MC) simulation techniques [6, 7], to verify or compliment results with the PB-BVP formalism.

1.4. Effect of interfacial walls

We here introduce the main subject of this thesis — the effect of interfacial walls on macroionic colloidal suspensions. In particular, we are interested in how the colloidal macroions in microionic solutions behave very close to interfacial walls formed by substrates that may or may not have the same dielectric properties as the suspension. The usual bulk behaviour (absence of dielectric interfaces) is expected to change significantly when the macroions are in close proximity to a neutral or charged interfacial wall, immersed in, or confining the suspension to a half-space. Examples are; electrodes, container walls, air, probes, e.t.c. The expected change in behaviour near such

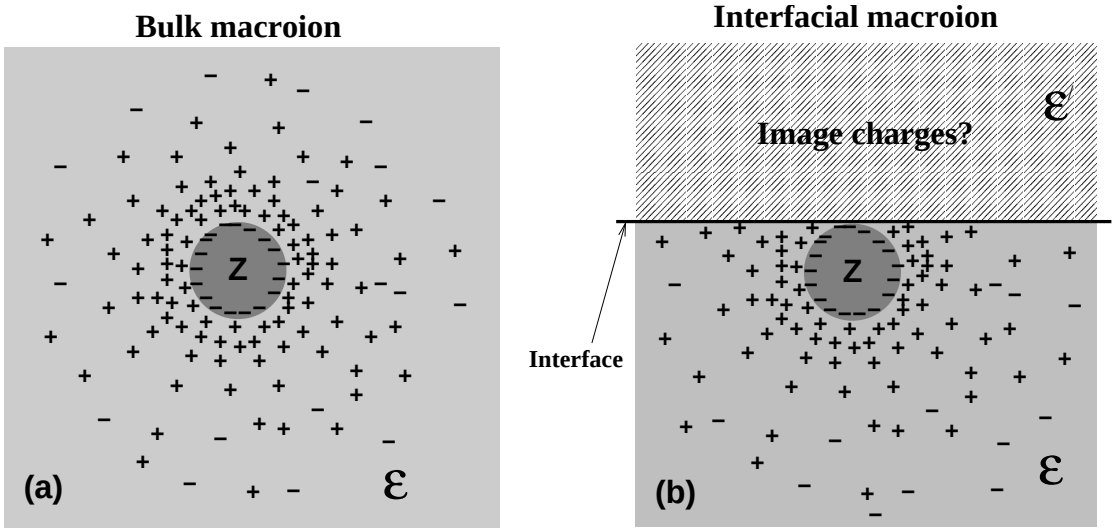

Figure 1.3: (a) A macroion in the solvent bulk with spherical EDL. (b) A macroion at an interface; the spherical EDL is distorted and there may be image-charges in the ϵ'-halfspace whose sign and magnitude depend on the ratio ϵ'/ϵ.

interfacial walls becomes obvious from the following considerations (see Fig. 1.3):

- The particles no longer just interact with themselves but also with the walls — the interaction may be significant if the wall is charged.
- Charged particles may have image-charges across the interface, resulting in additional interactions.
- The particles' degrees of freedom may be reduced, as in e.g. colloids trapped at a liquid-gas interface.
- Symmetries around the macroion may be broken leading for example, to distortion of the EDL.

- The solvent is confined to a half-space.

While in bulk, charge stabilized colloidal suspensions have been the subject of a vast number of theoretical and experimental investigations [2, 8-11], a lot more still needs to be done on understanding the structural properties of interfacial colloidal suspensions which have received only a handful of consideration in the literature [12-17], in most of which the specific roles of the interfaces are lacking. Interfacial suspensions are well suited as model systems to study, in general, the basic effects of dielectric discontinuity on the structural properties of a suspension of charged objects, be it an ion near a protein or a single DNA molecule (carrying a large net charge) near a membrane [18-22]. With respect to membrane/electrolyte systems, only a few studies exist that have yet addressed the question of image-charge effects [23, 24]. Furthermore, the importance of studies on interfacial suspensions is underscored by the ongoing debate in the literature [25-29] about the unexpected findings of attractive interaction between colloids near and between planar glass walls [30-32] and curious structures at the air-water interface [33-36]. A clear understanding of the specific role played in these findings by the effect of interface walls, e.g., image-charges is a necessary prerequisite for coming to any consistent interpretation of the experimental observations.

1.5. Relevance to experimental studies

The studies reported in this thesis are theoretical, and theoretical models are often caricatures of the real systems probed in experiments and applications. This is mainly due to simplifying approximations and averaging to make the system tractable to mathematical analysis. A typical example is the protein, where the complex three-dimensional structure of the polymer may be averaged into simple geometries like spheres and rods.

Nevertheless, good theories, in spite of approximations are able to interpret experimental data qualitatively and/or quantitatively, and have the advantage of making predictions where existing experimental apparatus and materials have limitations. That has been the guiding principle in our studies — to interpret experimental results and make predictions to guide further experimental studies.

To mention some examples: In chapter 2, we have obtained simple analytic approximate expressions for effective interaction potentials of a system of one macroion and a charged planar wall. One of these expressions is shown to agree remarkably well with experimental measurements using the TIRM (Total internal reflection microscopy) technique. We then went further to provide in a systematic way, regions in

the relevant parameter space where each approximate analytic potential can be used in estimating the exact wall–colloid interaction potential.

The work presented in chapter 3, can be used to interpret an experimental observation by Kesavamoorthy *et al* [16], where stable macroions in suspension suddenly pop up and get trapped at the air-water interface.

Crystallization of macroions at the air-water interface with a supporting substrate, studied in chapter 4, was originally motivated by an experiment on two-dimensional protein crystallization in an interface between the protein solution and an oxygen atmosphere, with mercury as the supporting substrate [37]. Our results, however, showed that a certain class of dielectric material other than that to which mercury belongs should make a better supporting substrate in macroions crystallization.

1.6. Outline and overview

In this section we outline the various studies presented in the remaining chapters. We give an overview of the objectives, methods used and results obtained in each chapter. A few general remarks are necessary: Each chapter proceeds with an introduction which sets the problem of the topic and a short review on it. An appendix to clarify points made in a chapter appears at the end of that chapter. The meaning of a symbol should be taken from its definition — closely related symbols may represent completely unrelated quantities, as can be seen directly from the list of some symbols provided in P. xi. Also provided is a list of abbreviations (P. ix).

The main studies are presented in chapters 2 to 5, while in chapter 6, we give a brief summary of the results and an outlook on the subjects for further studies.

Chapter 2 deals with the electric double-layer force between a charged colloidal sphere and a charged or uncharged dielectric planar wall. To introduce the problem and to uncover the basic physics involved, the effective wall–colloid potentials that one obtains in linearized PB theory is first reviewed. The important key concepts in this context are: charge renormalization, confinement effects, charged interfaces, and image-charge effects due to the dielectric discontinuity at the wall. Starting from the potentials derived in linear theory, approximate wall–colloid potentials are derived that are valid also in the parameter regime where the non-linearity of the Poisson–Boltzmann equation becomes important. The range of validity of these potentials is systematically investigated by comparing them with potentials based on the exact numerical solution to the PB equation. The important parameters of the calculation are the salt content of the electrolyte solution, the colloidal sphere radius, and the surface

charge densities on both the wall and the colloid. The chapter closes with a short report of an optical experiment that has been performed to measure the approximate wall–colloid potentials investigated here.

Chapter 3 is an extension of the work in chapter 2. Here the interfacial wall is specified as an uncharged air-water interface which can be penetrated by the colloidal particle. Still within the framework of linear and non-linear PB theory, we study the effective interaction of a single charged colloidal sphere in an aqueous electrolytic solution with the air-water interface. The effects of varying the salt concentration and the colloidal surface charge density on the effective interaction are investigated, with a view to understanding some physical phenomena, which include electrostatic adsorption and trapping at the air-water interface. Results show an electrostatic double-layer barrier against the colloid approaching the interface. This barrier can be lowered considerably by increasing the salt concentration of the suspension. At high enough added salt, the charged colloid should be able to suddenly pop up at the air-water surface, an effect which has actually been observed in recent experiments. The relevance of the results to other experimental observations is also discussed, and we emphasize the close analogy between the problem considered here and the classical problem of the interaction of two colloids in a bulk suspension.

In chapter 4, we study two-dimensional systems of macroions trapped at the interface between air and an aqueous electrolyte solution, in the presence of a dielectric substrate approaching the air-water interface from the water side. Working within the linear DH theory, we investigate how the microion-averaged interaction potential between the macroions is affected by the presence of the dielectric substrate. Using these potentials in a one-component MC simulation, we further study the structural changes and phase behaviour of the 2D colloidal system in response to the position of the substrate relative to the air-water interface. The scope of investigation covers two classes of colloidal particles, namely highly charged particles of tens of nanometers radius (e.g. latex particle), and particles of a few nanometers radius carrying relatively small numbers of total charge (e.g. proteins). Probing the bond-orientational order parameter Φ_6 as a function of the 2D particle surface fraction $\phi_{\rm surf}$ and the air-water/substrate-water separation distance L, our simulations show that structural formations at the air-water interface are strongly influenced by the presence and the dielectric nature of the supporting substrate. Specifically, our $[L : \phi_{\rm surf}]$ phase diagrams reveal that the transition from the fluid to the crystal phase is shifted to higher surface fractions, if the approaching substrate is metallic, and to lower surface fractions, if it has a very low dielectric constant. These phase diagrams may be useful for choosing materials and substrate interfaces for growing, e.g. the elusive crystals of protein particles in 2D.

Chapter 5: As opposed to the previous chapter where studies are based on the DH theory and one-component MC simulation, we here employ non-linear PB theory and primitive MC simulation in cell model approximations, for suspensions where the macroions are just below the surface. In primitive model simulation, all types of ions in the suspension are explicitly accounted for. We investigate some properties of the interfacial colloidal suspensions, which include the total electrostatic force acting on a macroionic sphere due mainly to image-charge forces and confinement. We also show how these effects can modify the effective charge of the interfacial macroion. For a broad range of possible system parameters used in the calculations, it was possible to scale down the parameters in both the MC simulation and the PB theory in the salt-free approximation. The MC simulation result also reveals effects due to correlation and finite-size of the microions integrated out in most PB theories. We discuss how both confinement and image-charges affect the structural properties of interfacial colloidal suspensions.

Note on bibliography

Finally, we mention some few books and papers, which may or may not have been cited directly in the text, but have played a vital role in the writing of this thesis. They include: the highly recommendable book of Verwey and Overbeek [2] dealing with the theories of EDL; Books by Schmitz [8],Russel [38], the review articles of Nägele [10], Löwen and Hansen [39] for a good introduction to the field colloids and EDL theories; the books of Israelachvili [3] and Overbeek [1] on surface forces; Evans and Wennerström [9], an interdisciplinary book; a collection of articles on experiments edited by Arora and Tata [11]. Most of our needs on computer simulation techniques were met by the books of Allen and Tildesley [6] and Frenkel and Smit [7]. The old but classical paper by Stillinger [40] on DH theory of interfacial macroions, and the experiment of Pieranski [12] on two-dimensional colloidal crystals at the air-water interface formed the backbone and motivation for most of this work, which in turn has resulted directly or indirectly in the following list of papers:

1. H.H. von Grünberg and E.C. Mbamala, *Colloidal suspensions at dielectric interfaces*, J. Phys.: Condens. Matter **12** (2000) 10349-10370.

2. H.H. von Grünberg and E.C. Mbamala, *Charged colloids near interfaces*, J. Phys.: Condens. Matter **13** (2001) 4801-4834.

3. E.C. Mbamala and H.H. von Grünberg, *Effective interaction of a charged colloidal particle with an air-water interface*, J. Phys.: Condens. Matter **14** (2002) 4881-

4900.

4. E.C. Mbamala and H.H. von Grünberg, *Charged colloids and proteins at air-water interface: the effect of dielectric substrates on interaction and phase behaviour*, Accepted for publication: Phys. Rev. E **67**, (2003).

5. E.C. Mbamala and G. Pastore, *Optimal Monte-Carlo sampling for simulation of classical fluids*, Physica **A 313** (2002) 312-320.

6. E.C. Mbamala and H.H. von Grünberg, *Effective charges of macroions: Confinement and image-charge effects*, In preparation (2002).

2

Effective interaction: A charged colloid with an interfacial wall

2.1. Introduction

This chapter is concerned with the apparently simple question of how a charged colloidal spherical particle (hereafter colloid or macroion) inside an electrolyte solution interacts with a planar wall which has a dielectric constant that is different from that of the solution and which may or may not bear any surface charges. That the answer is, in fact, not straightforward, becomes obvious from the list of observations made already in sec. 1.4, chapter 1, where the structure of the double layer of a spherical particle undergoes a sharp alteration very close to a wall. For a charged wall, there is an additional complexity arising from the double layer formed by the fixed charges on the wall and the mobile electrolyte ions. The complex density distributions of the microions around and between the colloid and wall for every possible wall–colloid distance, further complicate the calculation of the grand potential, the relevant thermodynamic function of the system. This quantity, when seen as a function of the wall–colloid distance, can only be regarded as the *effective* wall–colloid interaction potential where the term 'effective' is a reminder to the fact that an initial multi-component system has been reduced to a smaller system consisting of just the colloidal sphere and the wall. Obtaining such effective wall–colloid potentials is the main subject of this chapter.

To show that this subject, besides being fundamentally interesting, is also of practical interest, a few recent experiments are here recalled, where charged latex colloids or biocolloids near an interface play a major role. There is a series of optical exper-

iments where the effective pair potentials between colloids near a glass surface have been measured, with the surprising finding that at long range, colloids may attract each other, even though they bear like charges [30-32, 41-43]. As earlier mentioned, this unexpected attraction has caused a long theoretical debate on whether or not this can be explained within the Poisson-Boltzmann (PB) theory [25-29, 44-47], and has also been interpreted in terms of hydrodynamic interactions [48]. Another set of studies related to this topic are concerned with the adsorption of charged poly-electrolytes, specifically DNA molecules, on fluid or glass-supported cationic lipid bilayers [18-22, 49, 50], where image-charge effects might be of considerable importance [51]. Finally there is the TIRM, an optical method based on the evanescent wave near an interface, designed to measure the interaction between a single colloidal particle and a wall [52-57]. There will be a short report on a TIRM experiment in the last section of this chapter. Another interesting example can be found in Ref. [58] where the effective interaction between a biological cell and a smooth surface has been studied using the TIRM method. Other works related to the present subject include studies of the interaction and structural properties of interfacial colloidal suspensions [13, 59, 60], wall-induced layering in colloidal hard-sphere glasses [61], and super-cooled colloidal suspensions [62]. There are studies on image-charge effects on colloidal crystal ordering [14, 15, 17], the huge field of lipid–protein interaction—see for instance [24]—and works on colloidal aggregation [33], two-dimensional crystallization and melting [12, 16] affected in someways by interfacial walls.

The procedure here is to solve the PB equation numerically to determine the mean-field electrostatic potential and, from it, the effective interaction potential between the colloid and the wall. We compare the numerically determined potentials with approximate analytical potentials obtained through linearized and corrections to linearized PB equations, and check systematically in what parameter regimes these potentials can be used. Carnie and co-workers (see e.g. Refs [63-68]) have made similar studies on the interactions between two similar or dissimilar spheres in the bulk electrolyte solution, including recently [67] a sphere and a plate. In most of these studies, they have compared results obtained by numerical solution of the PB equation with those from approximate models, e.g. the linear superposition approximation, the Derjaguin method, etc. Warszynski and Adamczyk [69], also treating two dissimilar spheres and sphere/wall interaction, have gone a step further in their numerical scheme, to include the electric field distributions within the particles and wall which are usually neglected in most studies including the present one. Bhattacharjee and Elimelech [70] used a method that they referred to as surface element integration to determine the van-der-Waals and electrostatic double-layer interaction between a sphere and an infinite plate, starting from the well-known energy of interaction between two infinite paral-

lel plates. Their method, which basically integrates the flat-plate interaction energy per unit area over a planar projected area on the particle surface, seems to agree well with a numerical solution of the problem and improves on the conventional Derjaguin method.

In the three studies [67, 69, 70], the PB equation has been solved in the sphere/wall geometry and compared to approximate models that are often themselves based on numerical solutions. The philosophy here is somewhat different: we obtain less sophisticated analytical potentials, similar to those to be found already in classical books on colloid, e.g. by Verwey and Overbeek [2], which have however the advantage of being more handy for experimentalists as they are of purely analytical form. This, in conjunction with the fact that we have systematically explored the range of validity of these potentials, should make this study useful primarily to those who need a quick estimate of the wall–colloid interaction energy but not the best accuracy possible. Another feature of the study here is that we emphasize the role played by image-charges. Contrary to other studies, we have taken account of their contribution to the effective wall–colloid interaction potential, which results in a non-zero interaction even when the wall is uncharged.

The next section (sec. 2.2) is devoted to the formulation of the PB boundary value problem (BVP) and clarifying the concept of 'effective interactions'. This is followed by sec. 2.3 where a detailed discussion of studies on the effective wall–colloid interaction based on the linearized PB theory is made. Potentials obtained by non-linear corrections to the *linear*-effective potentials are presented in sec. 2.4, and their range of validity discussed in sec. 2.5. The chapter closes with a brief discussion on the TIRM experiment (sec. 2.6).

2.2. Formulation of the problem

We consider a charged spherical colloid in the vicinity of a planar interface between an electrolyte solution and a dielectric substrate. At this interface, there can be additional static surface charges. The electrolyte is assumed to be unbounded; that is, there is a reservoir of electrolyte ions coupled to the system, so the number of ions in the system can vary. The thermodynamic variables that are fixed are thus: the temperature T, the chemical potential of the salt ions μ_s, and the volume of the system V. The ensemble that we work in is then the grand-canonical ensemble with the grand potential Ω being the relevant thermodynamic potential. The principal question that guides this study is: how does the grand potential of the whole system depend on the distance h of the centre of the colloidal particle from the interface wall? This function can be

regarded as the effective wall–colloid interaction potential [71, 72]. The strategy here for calculating the effective potential is, (i) to solve the mean-field PB equation for a fixed wall–colloid distance h to determine the electrostatic mean-field potential ϕ, and (ii) use this potential to evaluate the grand potential. Repeating this procedure for varying h, we then obtain the effective interaction potential as a function of h.

The colloidal sphere of radius a bears Z negative surface charges, while the confining wall has a surface charge density of $-e\sigma_w$. These charges, which are *fixed*, in contrast to the *mobile* salt or counterions ions (of screening constant κ), enter the problem through the boundary conditions. Let us call the boundary given by the $z = 0$ interfacial wall ∂G_w, the surface of the colloid particle ∂G_c, the region of the electrolyte solution between the two surfaces G, and the negative $z < 0$ half-space $G_<$; see Fig. 2.1. At

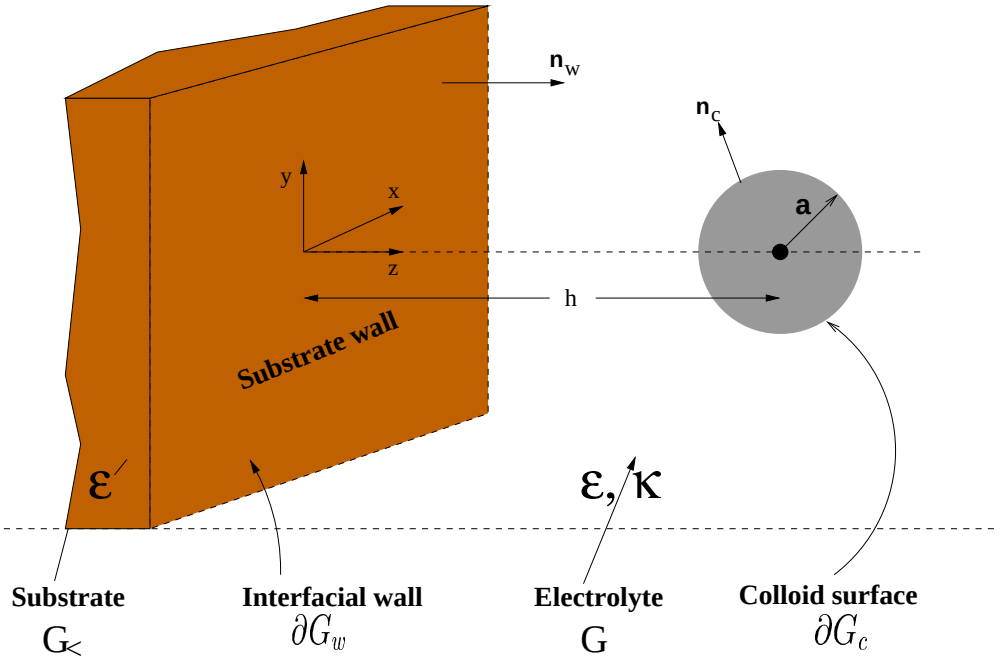

Figure 2.1: The model system: a colloid of charge $-Ze$ and radius a inside an electrolyte solution of dielectric constant ϵ, a distance h away from a substrate of dielectric constant ϵ'.

∂G_c we then require the normal component of the electric field to be identical to the colloidal surface charge density $\sigma_c = Z/4\pi a^2$ (the constant-charge boundary condition), while at ∂G_w we must demand that the normal component of the electric displacement field jumps by the amount $4\pi\epsilon\lambda_B\sigma_w$. With the boundary condition at ∂G_c, we have assumed (for simplicity) that the dielectric constant of the colloid is vanishingly small. In addition, we assume that the potential vanishes at infinity.

The PB equation, eq. (1.7) along with these boundary conditions, then leads to the

following BVP for the potential, $\phi(\mathbf{r})$:

$$\begin{aligned} \nabla^2\phi &= \kappa^2 \sinh\phi & \mathbf{r} &\in G \\ \nabla^2\phi &= 0 & \mathbf{r} &\in G_< \\ \epsilon \mathbf{n}_w \nabla\phi\big|_{z=0+} - \epsilon' \mathbf{n}_w \nabla\phi\big|_{z=0-} &= 4\pi\epsilon\lambda_B\sigma_w & \mathbf{r} &\in \partial G_w \\ \mathbf{n}_c \nabla\phi &= 4\pi\lambda_B\sigma_c & \mathbf{r} &\in \partial G_c \\ \phi &= 0 & \mathbf{r} &\to \infty \end{aligned} \tag{2.1}$$

where ϵ' is the dielectric constant of the substrate. $\mathbf{n}_w$ and $\mathbf{n}_c$ are unit outward vectors, normal to the surfaces of the wall and the colloidal sphere, respectively, and pointing towards G. Since there is still rotational symmetry about the z-axis (see Fig. 2.1), eq. (2.1) can essentially be represented in two spatial variables, i.e. $r \to (s, z)$ where $s = \sqrt{x^2 + y^2}$.

Furthermore, in the numerical scheme to solve the BVP, eq. (2.1), the complex boundaries of the real system are mapped into simple rectangular boundaries. This is achieved by converting the (s, z)-coordinates to the bispherical coordinate (BSC) system (η, θ, φ) [73], as has been done by others before [65, 74, 75]. Here and in the next chapter, the general procedure in the numerical scheme involves expressing the Laplacian appearing in the PB-BVP in the appropriate coordinates. The mildly nonlinear elliptic BVP, in which the nonlinearity arises solely through the potential function is reduced to a sequence of linear elliptic problems by the Newton-Raphson iteration method [76, 77]. Each iteration requires the solution of a linear elliptic problem, achieved using the HERMCOL [77], a publicly available code. This method uses a fourth-order discretization based on collocation with bi-cubic Hermite basis functions. The resultant linear equations are then solved with a band solver. And the resulting potential in every iteration is used in the numerical integration for the grand potential, also expressed in the appropriate coordinates. This continues until the iteration converges to the desired accuracy.

2.2.1. The boundary value problem in bispherical coordinates

Scaling all lengths by κ^{-1} and introducing

$$\begin{aligned} \varsigma_w &= \lambda_B\sigma_w/\kappa \\ \varsigma_c &= \lambda_B\sigma_c/\kappa \end{aligned} \tag{2.2}$$

the BVP of eq. (2.1) for the special case $\epsilon'/\epsilon = 0$ can be written in the following form:

$$\begin{aligned} \nabla^2\phi &= \sinh\phi & \mathbf{r} &\in G \\ \mathbf{n}_w\,\nabla\phi &= 4\pi\varsigma_w & \mathbf{r} &\in \partial G_w \\ \mathbf{n}_c\,\nabla\phi &= 4\pi\varsigma_c & \mathbf{r} &\in \partial G_c \\ \phi &= 0 & \mathbf{r} &\to \infty. \end{aligned} \tag{2.3}$$

In the absence of any charged body (e.g. the colloid) in the electrolyte solution, the problem reduces to only the double layer of the wall. The solution of the resulting BVP is the Gouy–Chapman potential ϕ^{GC} given in eqs (2.47) and (2.48). We define the potential $\tilde{\phi}$ as the difference of the true potential ϕ and ϕ^{GC} which leads to a new BVP in ϕ^{GC} and $\tilde{\phi}$ as follows:

$$\begin{aligned} \nabla^2\tilde{\phi} &= \sinh(\tilde{\phi}+\phi^{GC}) - \sinh\phi^{GC} & \mathbf{r} &\in G \\ \mathbf{n}_w\,\nabla\tilde{\phi} &= 0 & \mathbf{r} &\in \partial G_w \\ \mathbf{n}_c\,\nabla\tilde{\phi} &= 4\pi\varsigma_c - \mathbf{n}_c\,\nabla\phi^{GC} & \mathbf{r} &\in \partial G_c \\ \tilde{\phi}(\infty) &= 0 & \mathbf{r} &\to \infty. \end{aligned} \tag{2.4}$$

We thus calculate not the double layer in front of the wall, but its perturbation due to the charged colloid.

The BSC are related to the cylindrical coordinates (s, z), where $s(x, y)$ is the radial part; $x = (b\sin\theta\cos\varphi)/(\cosh\eta - \cos\theta)$ and $y = (b\sin\theta\sin\varphi)/(\cosh\eta - \cos\theta)$. Hence,

$$\begin{aligned} s &= \frac{b\sin\theta}{\cosh\eta - \cos\theta} \\ z &= \frac{b\sinh\eta}{\cosh\eta - \cos\theta}. \end{aligned} \tag{2.5}$$

Using eq. (2.5), the region external to the colloidal sphere becomes the rectangular domain (Fig. 2.2 with $\eta_i \to \eta_0$ in (c)): $\eta_0 \le \eta \le \eta_c$ and $0 \le \theta \le \pi$, where $\eta_0 = 0$ and η_c are coordinate surfaces of constant η corresponding to the interfacial wall and the colloid respectively.

The constant η spheres are of radius R_η and their centres are at a distance C_η:

$$\begin{aligned} R_\eta &= \frac{\kappa b}{\sinh\eta} \\ C_\eta &= \frac{\kappa b\cosh\eta}{\sinh\eta} = \kappa b\coth\eta. \end{aligned} \tag{2.6}$$

The constants b and η_c, are defined by requiring that $R_{\eta_c} = \kappa a$ and $C_{\eta_c} = \kappa h$.

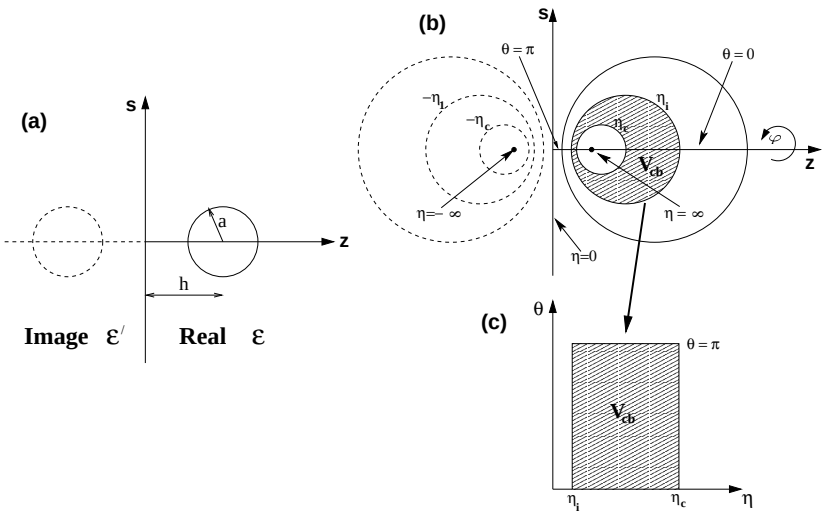

Figure 2.2: The bispherical coordinate system: The system consisting of the colloidal sphere and its image across the interface (z=0), in the (s, z)-coordinates in shown in (a). In (b), the region external to the sphere whose surface corresponds to a constant η-coordinate surface, η_c, can be mapped onto a rectangular volume, V_{cb} as shown in (c).

We can now write the BVP in eq. (2.4) in terms of the (η, θ)-coordinates, expressing the Laplacian also in bsc [73] and using the boundary conditions for $\tilde{\phi}$ on the four sides of the rectangle (see Fig. 2.2(c)) as follows:

$$\begin{aligned} \partial_\eta \tilde{\phi}\big|_{\eta=\eta_c} &= 2\kappa b \sinh(\Phi_w/2)\frac{1-\cosh\eta_c\cos\theta}{(\cosh\eta_c-\cos\theta)^2} - \frac{4\pi\kappa b\varsigma_c}{(\cosh\eta_c-\cos\theta)} \\ \partial_\eta \tilde{\phi}\big|_{\eta=0} &= \partial_\theta \tilde{\phi}\big|_{\theta=\pi} = \partial_\theta \tilde{\phi}\big|_{\theta=0} = 0 \qquad (2.7) \\ \tilde{\phi}(\eta=0,\theta=0) &= 0. \end{aligned}$$

For the new BVP we can now employ the Newton–Raphson iteration scheme, which takes the form

$$\nabla^2\tilde{\phi}_{n+1} - \cosh(\tilde{\phi}_n+\phi^{GC})\tilde{\phi}_{n+1} = \sinh(\tilde{\phi}_n+\phi^{GC}) - \sinh\phi^{GC} - \cosh(\tilde{\phi}_n+\phi^{GC})\tilde{\phi}_n \quad (2.8)$$

where a new estimate $\tilde{\phi}_{n+1}$ of the solution of the non-linear PB equation is obtained from a previous estimate, $\tilde{\phi}_n$.

And once we know ϕ, we can proceed to calculate the grand potential of the system:

2.2.2. The grand potential

For our system, assumed to be coupled to a reservoir of electrolyte ions, the number of the microions is not fixed, and the appropriate thermodynamic function is the grand

potential, Ω.

In the grand-canonical description, the bulk concentration c_s of electrolyte ions (monovalent salt) is a fixed input parameter of the calculation, and is directly related to the chemical potential of the salt, $\beta\mu_s = \log c_s\Lambda_T^3$, with Λ_T^3 being the usual thermal wavelength. The local density of positive/negative microions can be obtained from $p_\pm = c_s e^{\mp\phi}$, so the net charge density at a given point $\mathbf{r}$ in the solution is $\rho(\mathbf{r}) = \rho_+ - \rho_- = -2c_s \sinh\phi(\mathbf{r})$, and the total ion number density is $\rho_+ + \rho_- = 2c_s\cosh\phi(\mathbf{r})$, see eq. (1.6).

Von-Grünberg [78] in the manner of Netz *et al* [79-82], has employed a field theoretic formulation of the grand canonical ensemble partition function, to obtain Ω for our kind of system. Following Ref. [78], the grand potential for our system in units of the thermal energy, $\beta\Omega$ can be written as:

$$\begin{aligned}\beta\Omega &= \frac{1}{8\pi\lambda_B}\int_G \mathrm{d}\mathbf{r}\ (\nabla\phi)^2 + \frac{\epsilon'/\epsilon}{8\pi\lambda_B}\int_{G_<}\mathrm{d}\mathbf{r}\ (\nabla\phi)^2 \\ &\quad + \sum_{i=\pm}\int_G \mathrm{d}\mathbf{r}\ \rho_i(\log\rho_i\Lambda_T^3 - 1) \\ &\quad - \beta\mu_s\int_G \mathrm{d}\mathbf{r}\ (\rho_+ + \rho_-) + \int_G \mathrm{d}\mathbf{r}\ 2c_s.\end{aligned} \tag{2.9}$$

The first and second terms give the energy stored in the electric field in G and $G_<$ respectively. The third gives the entropy of mixing of the microions, and the last terms account for the fact that the number of ions in the system varies. The energy of the Z elementary charges on the colloid surface in their own Coulomb potential ($Z^2\lambda_B/2a$ which diverges if a vanishes), is contained in eq. (2.9). On substitution of $\rho_\pm$(r) and $\beta\mu_s$, eq. (2.9) becomes

$$\begin{aligned}\beta\Omega &= \frac{1}{8\pi\lambda_B}\left[\int_G \mathrm{d}\mathbf{r}\ (\nabla\phi)^2 + \frac{\epsilon'}{\epsilon}\int_{G_<}\mathrm{d}\mathbf{r}\ (\nabla\phi)^2\right. \\ &\quad \left. +2\kappa^2\int_G \mathrm{d}\mathbf{r}\ \big(\phi\sinh\phi - \cosh\phi + 1\big)\right].\end{aligned} \tag{2.10}$$

Using Green's first identity, we can decompose the terms $\int \mathrm{d}\mathbf{r}\ (\nabla\phi)^2$, to have

$$\begin{aligned}\beta\Omega = \frac{1}{8\pi\lambda_B}\Bigg[&-\int_{\partial G_w}\mathrm{dS}\ \left[\mathbf{n}_\mathrm{w}\,\nabla\phi_\mathrm{h}\big|_{\mathrm{z}=0+} - \frac{\epsilon'}{\epsilon}\mathbf{n}_\mathrm{w}\,\nabla\phi_\mathrm{h}\big|_{\mathrm{z}=0-}\right]\phi_\mathrm{h} \\ &- \int_{\partial G_c}\mathrm{dS}\ \mathbf{n}_\mathrm{c}\,\nabla\phi_\mathrm{h}\,\phi_\mathrm{h} + \kappa^2\int_\mathrm{G}\mathrm{d}\mathbf{r}\ (\phi_\mathrm{h}\sinh\phi_\mathrm{h} - 2\cosh\phi_\mathrm{h} + 2)\Bigg].\end{aligned} \tag{2.11}$$

This can be further simplified by inserting the boundary conditions of the BVP in eq. (2.1), which leads to

$$\beta\Omega_h = -\frac{\sigma_w}{2}\int_{\partial G_w}\mathrm{dS}\ \phi_\mathrm{h} - \frac{\sigma_\mathrm{c}}{2}\int_{\partial\mathrm{G_c}}\mathrm{dS}\ \phi_\mathrm{h} + \mathrm{c_s}\int_\mathrm{G}\mathrm{d}\mathbf{r}\ (\phi_\mathrm{h}\sinh\phi_\mathrm{h} - 2\cosh\phi_\mathrm{h} + 2). \tag{2.11a}$$

The position of the boundary ∂G_c in eq. (2.1) depends on the wall–colloid distance h, thus for one specific value of the external parameter h, we have one BVP to solve. In eq. (2.11), we have thus written ϕ_h to stress that ϕ still depends parametrically on h, and so does the grand potential. It was however, found more convenient (only in this non-linear numerical scheme) to calculate the force on the particle and integrate it with respect to h to obtain the grand potential. The force calculation (in bispherical coordinate system) is given in the appendix (sec. 2.8.1).

We define the effective wall–colloid interaction potential $\beta V(h)$ as the total change of the grand potential when the colloidal sphere is brought from the bulk, $h = \infty$ to a finite distance h close to the wall:

$$\beta V(h) = \beta(\Omega_h - \Omega_\infty). \tag{2.12}$$

With the numerical solution of eq. (2.1) used eq. (2.12), we thus arrive at the effective interaction potential in full non-linear PB theory.

2.3. The interaction potential in linear theory

Due to the non-linearity of the PB equation, the BVP of eq. (2.1) can in general only be solved numerically. Analytical work is feasible merely in the special case where ϕ is everywhere smaller than one, in which case linearization of the BVP of eq. (2.1) becomes possible. But even then, as we will see soon, further approximation is needed to arrive at analytical expressions for the effective potential. Nevertheless, we begin by studying the linear case, mainly for the reason that the basic features of our problem can best be understood at this level of approximation. In sec. 2.4, we return to the non-linear theory formulated in eqs (2.1) and (2.11).

Linearizing the PB equation in eq. (2.1) leads to the following BVP:

$$\begin{aligned}
\nabla^2\phi &= \kappa^2\phi && \mathbf{r} \in G \\
\nabla^2\phi &= 0 && \mathbf{r} \in G_< \\
\epsilon \mathbf{n}_w \nabla\phi\big|_{z=0+} - \epsilon' \mathbf{n}_w \nabla\phi\big|_{z=0-} &= 4\pi\epsilon\lambda_B\sigma_w && \mathbf{r} \in \partial G_w \\
\mathbf{n}_c \nabla\phi &= 4\pi\lambda_B\sigma_c && \mathbf{r} \in \partial G_c \\
\phi &= 0 && \mathbf{r} \to \infty.
\end{aligned} \tag{2.13}$$

The grand potential, too, becomes much simpler after the linearization, because the volume integrals in eq. (2.11a) vanish due to the fact that $\phi_h \sinh\phi_h - 2(\cosh\phi_h - 1) \approx 0$ if $\phi < 1$. This leaves us with

$$\beta\Omega_h = -\frac{\sigma_w}{2}\int_{\partial G_w} \mathrm{dS}\ \phi_\mathrm{h} - \frac{\sigma_\mathrm{c}}{2}\int_{\partial \mathrm{G_c}} \mathrm{dS}\ \phi_\mathrm{h}. \tag{2.14}$$

We see that, in linear theory, the grand potential reduces to just the electrostatic energy of the system—that is, the electrostatic energy which the colloidal (σ_c) and interfacial charges (σ_w) have in the mean-field potential ϕ. Carnie *et al* solved this BVP and calculated the effective colloid potential from it [66], which they later on compared with the numerical solution of the full PB equation [67]. Related studies on the double-layer interaction of two spheres in linearized theory can be found in [63, 68, 83].

2.3.1. The uncharged interface: interaction in the point-ion approximation

The case of an uncharged interface ($\sigma_w = 0$) already reveals most of the physical content subsumed in the effective wall–colloid pair potentials. That there is a non-vanishing effective interaction potential even in this case might at first seem surprising, but it becomes obvious if one realizes that the ionic double layer surrounding the colloid is heavily distorted from its usual bulk shape by the presence of the wall that is impenetrable to the ions. In addition to this confinement effect, we have to expect image-charge effects arising from the dielectric discontinuity across the interface. We now aim to discuss both effects by considering the case of a colloid near an uncharged wall.

Since the BVP of eq. (2.13) still poses severe problems due to the complicated geometry of the region G, i.e., the shape of the boundaries ∂G_c and ∂G_w, we simplify the problem a little further, and replace the colloidal sphere of finite size by a fixed *point-charge ion*—an approximation that is applicable when the particles are separated by distances much larger than their radii. We will refer to the case of a colloid of finite size in linear theory in sec. 2.3.2. For such a point-charge, the linearized PB-BVP of eq. (2.13) takes the form

$$\begin{aligned}
\nabla^2\phi &= \kappa^2\phi + 4\pi\lambda_B Z\left[\delta(h-z)\vec{e}_z\right. & \\
&\quad \left.+\delta(x)\vec{e}_x + \delta(y)\vec{e}_y\right] & \mathbf{r}\in G \\
\nabla^2\phi &= 0 & \mathbf{r}\in G_< \\
\epsilon\mathbf{n}_w\,\nabla\phi\big|_{z=0+} - \epsilon'\mathbf{n}_w\,\nabla\phi\big|_{z=0-} &= 0 & \mathbf{r}\in\partial G_w \\
\phi &= 0 & \mathbf{r}\to\infty,
\end{aligned} \tag{2.15}$$

where we used the fact that $\sigma_c = Z/4\pi a^2$. This BVP has long been solved by Stillinger [40], and independently by Schmutzer [84]. The Stillinger solution for the potential around a reference point-ion of charge $-Ze$ at the distance h (see Fig. 2.1) reads

$$\phi_h^{St}(s,z) = -Z\kappa\lambda_B\int_0^\infty \mathrm{d}\ell\; J_0(\kappa s\ell)\frac{\ell}{\tilde{\ell}}\left(\mathrm{e}^{-\kappa|z-h|\tilde{\ell}} + \tilde{\chi}(\ell)\mathrm{e}^{-\kappa(z+h)\tilde{\ell}}\right) \tag{2.16}$$

where $s = s(x, y)$, $\tilde{\ell} = (1 + \ell^2)^{1/2}$ and ℓ is just a convenient dimensionless variable having no physical meaning. J_0 is the zero order Bessel function and the quantities $\tilde{\chi}(\ell)$ and χ are given by

$$\tilde{\chi}(\ell) = \frac{\epsilon\tilde{\ell} - \epsilon'\ell}{\epsilon\tilde{\ell} + \epsilon'\ell} = \frac{\alpha(\tilde{\ell} + \ell) - \ell}{\alpha(\tilde{\ell} - \ell) + \ell} \tag{2.17}$$

and

$$\chi = \frac{\epsilon - \epsilon'}{\epsilon + \epsilon'} = 2\alpha - 1 \tag{2.18}$$

where $\alpha = \epsilon/(\epsilon + \epsilon')$ gives a relation between the dielectric constants of the electrolyte solution and the substrate. The nature of the Stillinger potential can best be understood in the infinite-dilution limit $\kappa \to 0$, when eq. (2.16) becomes [40]

$$\phi_h^0(s, z) = -Z\lambda_B \left[\frac{1}{|\mathbf{r} - h\vec{e}_z|} + \frac{\chi}{|\mathbf{r} + h\vec{e}_z|} \right]. \tag{2.19}$$

In this limit, there is no screening by salt ions any more, and we are left with the purely electrostatic problem of a single point charge near a dielectric substrate, which is the classical test case for the image-charge method [85]. And, indeed, the second term of eq. (2.19) can readily be identified as the potential due to the image-charge at $z = -h$, while the first term is just the simple Coulomb potential of our original charge at $z = h$. This image-charge has a magnitude of χZe. The Stillinger potential in eq. (2.16) for finite κ has very much the same structure, with the first term, the direct term, coming from the (now screened) point-ion and the second term, the indirect term, arising from the screened image-charge. Consistently with this association, the first term becomes in the bulk limit (infinite wall–colloid distances) just the Yukawa potential of the standard DH theory, while the second term vanishes.

In order to arrive at an effective potential, we next need to determine the grand potential as a function of h. Equation (2.14) in our case (uncharged wall, point-ion) becomes

$$\beta\Omega_h = -\frac{Z}{2} \lim_{s\to 0, z\to h} \phi_h^{St}(s, z) - \beta W^{SE}. \tag{2.20}$$

Here we need to subtract the divergent Coulomb self-energy βW^{SE} of the point-charge for the grand potential to be finite. It is better to write

$$\beta\Omega_h = -\frac{Z}{2} \lim_{s\to 0, z\to h} \left[\phi_h^{St}(s, z) - \phi_h^{C}(s, z)\right] \tag{2.21}$$

where

$$\phi_h^C(s, z) = -Z\lambda_B \frac{1}{|\mathbf{r} - h\vec{e}_z|} = -Z\kappa\lambda_B \int_0^\infty J_0(\kappa s\ell) \mathrm{e}^{-\kappa|z-h|\ell}\, \mathrm{d}\ell \tag{2.22}$$

is just the direct Coulomb potential of the point-charge, which we have rewritten using the identity [40]

$$\frac{1}{r} = \kappa \int_0^\infty J_0(\kappa s \ell) \mathrm{e}^{-\kappa x \ell} \, \mathrm{d}\ell. \tag{2.23}$$

Placing eq. (2.22) and (2.16) into eq. (2.21) and taking the limits, we obtain

$$\beta\Omega_h = \frac{Z^2 \kappa \lambda_B}{2} \int_0^\infty \mathrm{d}\ell \left(\frac{\ell}{\tilde{\ell}} + \frac{\ell}{\tilde{\ell}} \tilde{\chi}(\ell) \mathrm{e}^{-2\kappa h \tilde{\ell}} - 1 \right) \tag{2.24}$$

which for $h \to \infty$ becomes

$$\beta\Omega_\infty = \frac{Z^2 \kappa \lambda_B}{2} \int_0^\infty \mathrm{d}\ell \left(\frac{\ell}{\tilde{\ell}} - 1 \right) = -\frac{Z^2 \kappa \lambda_B}{2}. \tag{2.25}$$

This latter energy looks familiar from the DH theory, where it is known as the DH self-energy, i.e., the interaction energy of a point test ion located in the bulk of a symmetric electrolyte and interacting with its ion atmosphere. With eqs (2.24) and (2.25) we have finally arrived at the effective wall–colloid interaction potential:

$$\beta V_{St}(h) = \beta(\Omega_h - \Omega_\infty) = \frac{Z^2 \kappa \lambda_B}{2} \int_0^\infty \mathrm{d}\ell \, \frac{\ell}{\tilde{\ell}} \frac{\alpha(\tilde{\ell} + \ell) - \ell}{\alpha(\tilde{\ell} - \ell) + \ell} \mathrm{e}^{-2\kappa h \tilde{\ell}}. \tag{2.26}$$

The integral depends essentially on α $(= \epsilon/(\epsilon + \epsilon'))$ and κh and can be evaluated only numerically. But in the two most interesting limits, $\alpha = 1$ and $\alpha = 0$, eq. (2.26) reduces to simple Yukawa-like potentials:

$$\beta V_{St}(h) = \frac{Z^2 \kappa \lambda_B}{2} \left(\frac{\mathrm{e}^{-2\kappa h}}{2\kappa h} \right) \quad \text{if } \alpha = 1 \tag{2.27}$$

and

$$\beta V_{St}(h) = -\frac{Z^2 \kappa \lambda_B}{2} \left(\frac{\mathrm{e}^{-2\kappa h}}{2\kappa h} \right) \quad \text{if } \alpha = 0. \tag{2.28}$$

The $\alpha = 1$ case is the limit where the dielectric constant of the substrate ϵ', is much smaller than that of the solution (realized, for example, in the case of a glass-water or air-water interface) that ϵ' can be neglected against ϵ; $\epsilon'/\epsilon \sim 0$. The opposite limit, $\epsilon/\epsilon' \sim 0$ $(\alpha = 0)$, describes the case where a substrate of extremely large dielectric constant is in contact with a solution of much smaller dielectric constant, e.g., a metal-water interface. In the limit of zero salt concentration $(\kappa \to 0)$, we know from our discussion of eqs (2.18) and (2.19) that in the two limits, $\alpha = 1$ and $\alpha = 0$, the point-charge has image-charges of the same magnitude. They differ, however, in their charge polarity, having the same polarity when $\alpha = 1$ and just the opposite if $\alpha = 0$. Thus, the point-charge at position h sees a potential $\pm Z\lambda_B/2h$ and the wall–colloid interaction

potential is $\mp Z^2\lambda_B/4h$, which is negative if $\alpha = 0$ and positive if $\alpha = 1$. A single point-charge in water is therefore attracted to a metal surface, but repelled from an uncharged glass surface. Now, if there are salt ions present ($\kappa > 0$), this changes only inasmuch as the image charge is screened by the salt ions, which produces just the screening factor $e^{-2\kappa h}$ in the potential, $\pm Z\lambda_B e^{-2\kappa h}/2h$, and the interaction potentials then become the screened Yukawa-like potentials of eqs (2.27) and (2.28). These effective potentials can therefore be understood as the interaction of the point-charge with its own *screened* image-charge, which is attractive if $\epsilon' \gg \epsilon$ and repulsive if $\epsilon' \ll \epsilon$. All other cases, $0 < \alpha < 1$, are covered by the effective potential of eq. (2.26), which when plotted against the distance from the planar interface always lies between those of eqs (2.27) and (2.28), as is evident from Fig. 2.3.

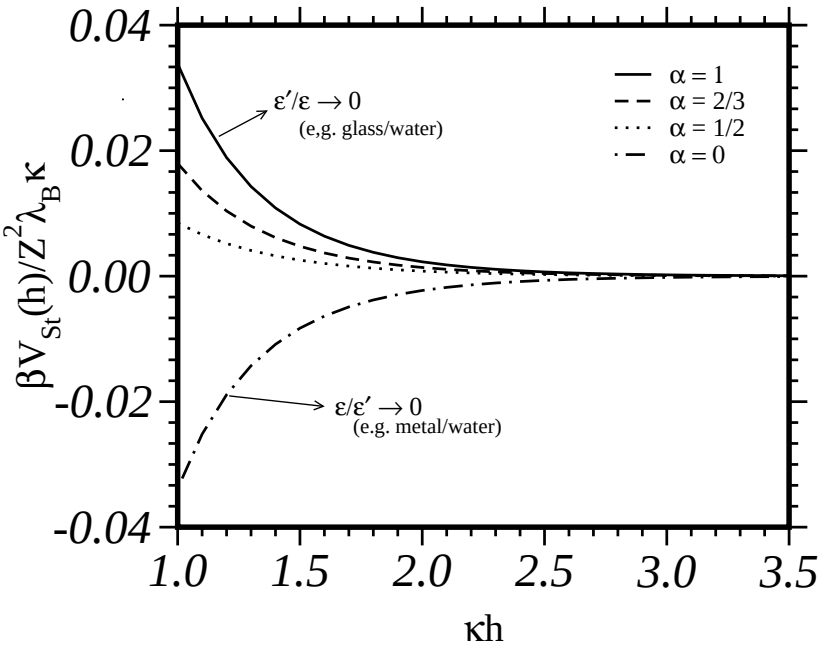

Figure 2.3: The effective wall–colloid interaction potential $\beta V_{St}(h)/Z^2\lambda_B\kappa$ of eq. (2.26) for various values of $\alpha = \epsilon'/(\epsilon+\epsilon')$, calculated in linear theory. The macroion is considered as point-like ($\kappa a = 0$).

In Fig. 2.4 we show the effective potential of eq. (2.26) when the point-charge nearly touches the wall ($\kappa h = 0.8, 1.0, 1.2$), as a function of α. This quantity may be interpreted as the energy gained or lost in bringing the point-ion from infinity to the surface of the wall, and can be used to make predictions about the adsorption behaviour of colloids on dielectric walls. We see that adsorption is favoured if $\alpha = 0$, while desorption is favoured for $\alpha = 1$, as one would intuitively predict from our simple electrostatic considerations in the $\kappa \to 0$ limit.

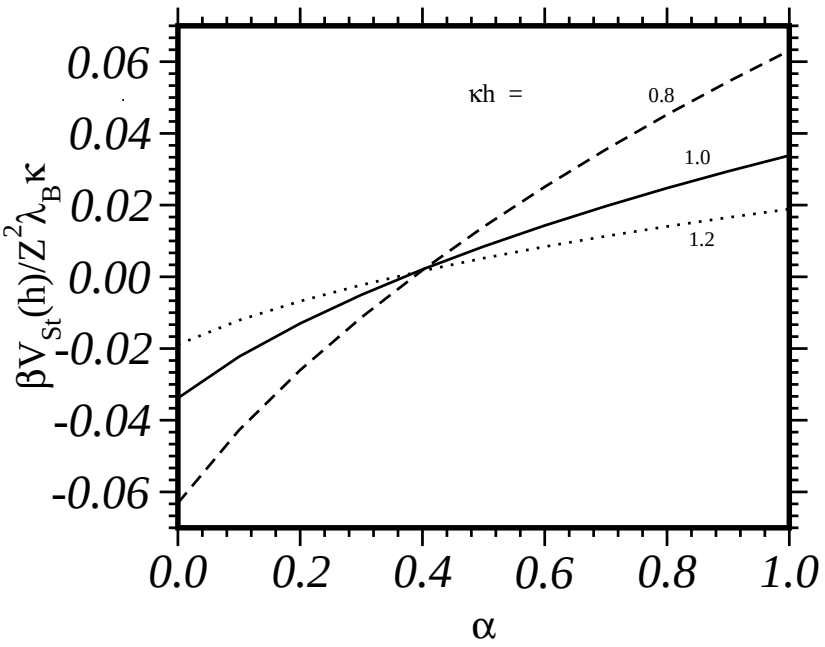

Figure 2.4: The effective potentials as in Fig. 2.3 (eq. (2.26)) at fixed values of κh, but here as functions of α.

In his paper, Stillinger presented a similar curve (Fig. 2 of Ref. [40]) where the interaction energy W of the point-charge at $h = 0$ with its ion atmosphere is plotted as a function of α. The far more important interaction between the point-charge and its image has however been rightly subtracted due to divergence. This curve shows a monotonic *decreasing* behaviour, with W changing its sign from $+$ to $-$ at $\alpha = 0.645$. From this figure, Stillinger predicts adsorption if $\alpha = 1$ and desorption if $\alpha = 0$. This conclusion is not correct since the mechanism for such adsoption is not favourable. It is just the other way round, as we have seen, and the error is clearly due to the neglect of the direct interaction of the point-charge with its image. The same error has been made by Earnshaw [59] who predicts an electrostatic trapping of colloids at an air-water interface due to decreasing interface–colloid interaction potential towards the interface. The correct role of electrostatic forces in the trapping of colloids at the air-water interface is clarified in the next chapter. However, it suffices from the above discussion to say that a colloid in an aqueous suspension will be repelled from, and not attracted to an air-water and similar interfaces.

If the substrate has the same dielectric constant as the solution, $\epsilon = \epsilon'$ (i.e. $\alpha = 1/2$), there are no image-charges, as we can see from eqs (2.18) and (2.19). And still, the colloid is repelled from the wall; see Figs 2.3 and 2.4. This is accounted for by the fact that the shape of the colloidal double layer deviates from its perfect spherical bulk

shape when the colloid approaches the wall. This is so because of the presence of a wall which, though having the same dielectric constant as the solution, is impenetrable to electrolyte ions. This distortion will restrict the motion of the microions, leading to an increase in the free energy. Therefore, repulsion is to be expected, when the particle is sufficiently close to the wall. We thus learn from Fig. 2.3 that the effective wall–colloid interaction is dominated by two effects: the confinement effect, on the one hand, and the image-charge effect, on the other, which both have a repulsive effect if $\alpha \geq 1/2$, and which compete with each other if $\alpha < 1/2$ (this means that a case is conceivable where the effective wall–colloid interaction is repulsive in spite of an attractive interaction between the charge and its image).

Both effects are usually present, though their relative importance for the effective potential is strongly dependent on α. To discriminate between one effect and the other, one has to choose a substrate having the same dielectric constant as the solution, thus eliminating all image-charges and leaving just the confinement effect.

We remark that the potential, eq. (2.16) is well known in the theory of the electric double layer. Most of the discussion on image-charge and confinement effects is usually also in this context and can be found in good review articles on double-layer theory, for example in Ref. [86]. Also potentials similar to eqs (2.27) and (2.28), have appeared in the literature as early as 1924 in studies by Wagner [87] and Onsager and Samaras [88] on surface tension of electrolytes.

2.3.2. Renormalizing the colloidal charge

We intend here to amend the potential around the test point-ion to take account of the finite size of a colloid. This follows from renormalizing the colloidal charge from $Z \to Z^* = Z/g$, a standard method known from the theory of effective colloid–colloid interaction in bulk [71]. The primary error that is involved in representing the colloid by a point-ion is that it allows microions to be in the region $r < a$ (r is the distance from the centre of the colloid, a its radius), where in reality they are excluded. If one determines the total charge (colloidal charge minus the total charge of salt ions) inside a virtual sphere of radius a, one obtains a charge $\mathcal{Z}$ which is only a fraction g of the colloidal point-charge Z, $\mathcal{Z} = gZ$. The renormalization trick now consists of the idea of taking a larger value Z/g for the colloidal point-charge, so that the total charge of all ions inside the sphere of radius, a becomes $\mathcal{Z} = gZ/g = Z$, i.e. the actual charge of the colloid. Then we can take this virtual sphere of effective charge Z as representing our colloidal sphere of radius a. This should work well as long as the ion distribution around the point-charge is essentially spherical, because the electric field outside a

charged sphere contains no information about the field-producing distribution of ions inside the sphere; any spherically symmetric distribution of the same total number of ions inside a has the same field at $r > a$.

Let us start by considering the bulk situation ($h \to \infty$), where the electrostatic potential around our colloidal point-charge in eq. (2.26) reduces to the usual DH potential:

$$\phi(r) = -\frac{Z\lambda_B \mathrm{e}^{-\kappa r}}{r} = \phi_\infty^{St} \tag{2.29}$$

and the ion charge density becomes

$$\rho(r) = -2c_s\phi = \frac{Z\kappa^2 \mathrm{e}^{-\kappa r}}{4\pi r}. \tag{2.30}$$

The net charge inside the virtual sphere is hence

$$\mathcal{Z} = g_\infty Z = Z - 4\pi \int_0^a \rho(r) r^2 \, \mathrm{d}r \tag{2.31}$$

which leads us to the familiar result

$$g_\infty = \frac{1+\kappa a}{\mathrm{e}^{\kappa a}}. \tag{2.32}$$

Translating these ideas now to the situation where h is finite, we have to carry out a two-dimensional integration to determine the net charge inside the virtual sphere, since the Stillinger potential depends on two variables, s and z (see eq. (2.16)):

$$Z(1-g_h) = 2\pi \int_{h-a}^{h+a} \mathrm{d}z \int_0^{p(z)} s \, \mathrm{d}s \; \rho_h(s,z) \tag{2.33}$$

with $\rho_h(s,z) = -2c_s\phi_h^{St}(s,z)$ which is derived from the Stillinger potential and $p(z) = \sqrt{a^2-(z-h)^2}$. Using the integral identity

$$\int_0^{\mathcal{B}} J_0[\mathcal{A}x] x \, \mathrm{d}x = \frac{\mathcal{B}}{\mathcal{A}} J_1[\mathcal{A}\mathcal{B}] \tag{2.34}$$

eq. (2.33) can be reduced to

$$g_h = 1 - \int_0^\infty I(\ell) \frac{1}{\tilde{\ell}} \left(1 + \tilde{\chi}(\ell) \mathrm{e}^{-2\kappa h \tilde{\ell}}\right) \mathrm{d}\ell \tag{2.35}$$

with

$$I(\ell) = 2 \int_0^\zeta \mathrm{d}\xi (\zeta^2 - \xi^2)^{1/2} J_1\left[\ell(\zeta^2-\xi^2)^{1/2}\right] \mathrm{e}^{-\tilde{\ell}\xi} \tag{2.36}$$

where $\xi = \kappa(z-h)$ and $\zeta = \kappa a$. For ease of evaluation, we take the limiting case $\tilde{\chi}(l) = 1$ ($\alpha = 1$) in eq. (2.35) and solve the resulting equation for g_h by numerical

integration. In Fig. 2.5, g_h is shown for various values of κa. It rises from the wall (interface) and approaches, as it should, the bulk limit g_∞ as κh becomes large. The first value of each curve corresponds to a situation where $h = a$, i.e. where the particle touches the wall. Interestingly, this first value becomes first smaller with increasing κa, up to $\kappa a = 1$, and goes up again for $\kappa a > 1$. This behaviour allows us to draw the conclusion that g_h will never deviate by more than a few percent from g_∞, and it is thus not only convenient, but also a good approximation to replace g_h by the much simpler expression for g_∞. This approximation will henceforth be adopted. We can best

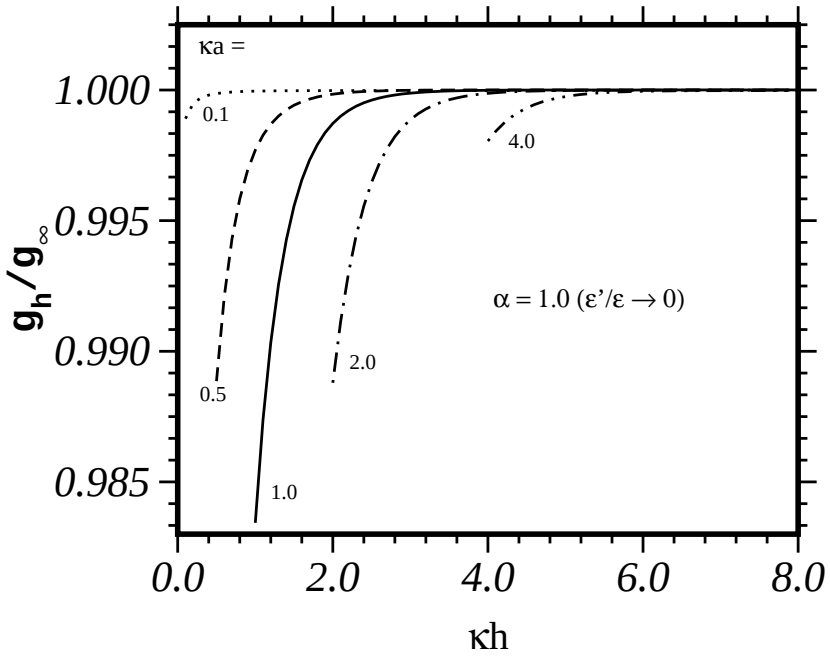

Figure 2.5: The ratio of the macroion charge renormalizing factor near the interface (g_h) to that of the bulk (g_∞), versus the macroion–wall distance κh, for $\alpha = 1$.

summarize the results obtained so far by repeating the effective wall–colloid interaction potential for the case $\alpha = 1$. This is a case that is naturally of prominent interest in our context, since colloids in most experiments are suspended in aqueous solutions, and water has a very large dielectric constant in comparison to practically most dielectric wall materials, so making the assumption that $\epsilon'/\epsilon \to 0$ is reasonably justifiable for colloidal systems. In the following we shall therefore focus on this important limiting case. Inserting Z/g_∞ with g_∞ from eq. (2.32) into eq. (2.27), we obtain the potential

$$\beta V_{St}(h) = \frac{Z^2 \mathrm{e}^{2\kappa a} \kappa \lambda_B}{2(1+\kappa a)^2} \left(\frac{\mathrm{e}^{-2\kappa h}}{2\kappa h} \right) \tag{2.37}$$

which demonstrates that increasing particle size results in increased repulsion from the

wall. The potential in eq. (2.37) is just half of the usual repulsive double-layer potential of DLVO theory between two like-charged spheres that are separated by a distance $2h$ from each other. This is clear: the BVP given in eq. (2.13) reveals that the normal component of the electric field at the interface is zero in our case where $\epsilon'/\epsilon = 0$. This is exactly the same situation as on the mid-plane between two identical spheres. In other words, the electric field lines on the positive side of the symmetry plane are identical in the two cases (wall–colloid and colloid–colloid). The only difference is that in the latter case the total volume filled by the electrolyte solution is just twice the volume in the former. Since the grand potential is obtained from the integration over this volume, it produces just a factor $1/2$, which then remains the only difference between eq. (2.37) and the effective colloid–colloid interaction in the bulk.

2.3.3. The charged interface: the superposition principle

After having considered the case where the surface charge density at the wall is zero ($\sigma_w = 0$), we now return to the starting point of this section, the BVP in linear theory, formulated in eq. (2.13). The great advantage of linearization of the PB equation is that one can make use of the superposition principle; that is, if one knows the electrostatic potential ϕ for a single point-charge, one can calculate the potential for an arbitrary charge distribution just by superposing the point-charge potentials. Therefore, we can reuse the Stillinger potential (which is just the potential for a single point-charge) as a Green's function for the more complex distribution of fixed charges appearing in the BVP of eq. (2.13).

To be specific, let us assume that the single point-charge, which in the Stillinger BVP of eq. (2.15) has been located at $z = h$, is now at the position $(h_x,\, h_y,\, h_z)$. This point-charge we now assume to have a charge $+e$. The Stillinger potential, given in eq. (2.16), has to be modified then in the following obvious way:

$$\phi_{\mathbf{h}}^{Gr}(x,y,z) = \kappa\lambda_B \int_0^\infty \mathrm{d}\ell\; J_0\left(\kappa\ell[(x-h_x)^2+(y-h_y)^2]^{1/2}\right) \times \frac{\ell}{\tilde{\ell}}\left(\mathrm{e}^{-\kappa|z-h_z|\tilde{\ell}} + \tilde{\chi}(\ell)\mathrm{e}^{-\kappa(z+h_z)\tilde{\ell}}\right). \tag{2.38}$$

This function is in fact the Green's function of the problem, eq. (2.13); see Refs [75, 89]. Given an arbitrary distribution of fixed charges $\sigma(\mathbf{h})$, we can now generate the corresponding potential by convoluting $\sigma(\mathbf{h})$ with this Green's function:

$$\phi(x,y,z) = \int \phi_{\mathbf{h}}^{Gr}(x,y,z)\sigma(\mathbf{h})\;\mathrm{d}\mathbf{h}. \tag{2.39}$$

For example, setting $\sigma(\mathbf{h}) = -Z\delta(h_x)\delta(h_y)\delta(h_z - h)$ and performing the integration in eq. (2.39) leads back to the original Stillinger potential, given in eq. (2.16). For the homogeneously charged interface at $z = 0$, we demand $\sigma(\mathbf{h}) = -\sigma_w\delta(h_z)$, which when inserted in eq. (2.39) gives a potential

$$\phi^{\sigma_w}(x, y, z) = -4\pi\frac{\sigma_w\lambda_B}{\kappa}\mathrm{e}^{-\kappa z} \tag{2.40}$$

that can easily be verified to be a solution to the BVP of eq. (2.13) when there is no colloid. We note, in passing, that eq. (2.40) is independent of ϵ', which is reasonable since the electric field at $z < 0$ is zero and the dielectric property of the wall material thus irrelevant. The general solution to the BVP in eq. (2.13) may be obtained from convoluting

$$\sigma(\mathbf{h}) = -\sigma_w\delta(h_z) - \sigma_c\delta(\sqrt{h_x^2 + h_y^2 + (h_z - h)^2} - a) \tag{2.41}$$

with the Green's function, eq. (2.38) This, however, amounts to an inconsistency, since we assumed a vanishing dielectric constant inside the colloidal sphere in our BVP of eq. (2.13), while a superposition of potentials of point-charges fixed at the surface of the colloids implies that the dielectric constant inside the sphere is the same as that outside. But since this is a rather involved undertaking [63, 66] leading again to non-analytical expressions, we must once more be content with the point-charge assumption for the colloid:

$$\sigma(\mathbf{h}) = -\sigma_w\delta(h_z) - Z\delta(h_x)\delta(h_y)\delta(h_z - h) \tag{2.42}$$

resulting in a potential which is nothing but the sum of the potentials of eqs (2.16) and (2.40), ϕ_h^{St} and ϕ^{σ_w}.

To obtain the effective potential, we need to look back at eqs (2.12) and (2.14) which lead us to

$$\beta V(h) = \beta V_{St}(h) - \frac{\sigma_w}{2}\int_{\partial G_w}\mathrm{d}S\phi_h^{St} - \frac{Z}{2}\phi^{\sigma_w}(h) \tag{2.43}$$

where the first term is the effective potential in the case of an uncharged wall, given in eq. (2.26), while the second and third terms give the interaction of the interfacial charges with the field produced by the colloidal point-charge and vice versa. These two latter terms are equal, so

$$\beta V(h) = \beta V_{St}(h) - Z\phi^{\sigma_w}(h) \tag{2.44}$$

which for $\alpha = 1$ $(\epsilon'/\epsilon \to 0)$ takes the form

$$\beta V(h) = \frac{Z^2\kappa\lambda_B}{2}\left(\frac{\mathrm{e}^{-2\kappa h}}{2\kappa h}\right) + Z\,4\pi\frac{\sigma_w\lambda_B}{\kappa}\mathrm{e}^{-\kappa h}. \tag{2.45}$$

From this expression it is evident that the colloidal point-charge interacts with two well separated charge distributions at the same time: with the interfacial charges, on the one hand, and the image charge, on the other. Both are screened, but one of them is a distance h away, and the other $2h$. The second term ($\sim \mathrm{e}^{-\kappa h}$), describing the direct interaction of the point charge interacting with the unperturbed double layer of the charged wall, will therefore be the dominant one for larger distances. The image-charge term, though having a pre-factor that goes as Z^2, becomes important only for small distances and small values of the ratio σ_w/Z. We expand on this further, below. Again, renormalization of the colloidal charge is useful, thus:

$$\beta V_{LIN}(h) = \frac{Z^2\kappa\lambda_B}{2(1+\kappa a)^2}\left(\frac{\mathrm{e}^{-2\kappa(h-a)}}{2\kappa h}\right) + Z\,4\pi\frac{\sigma_w\lambda_B}{\kappa(1+\kappa a)}\mathrm{e}^{-\kappa(h-a)}. \qquad (2.46)$$

We remark that Netz [79] in a recent work derived the Green's function of eq. (2.38) within a field-theoretic formalism. He considered the more general case, where there are mobile ions *within* the interface itself (salty interface) and two solutions with different salt concentrations and dielectric constants on either side of the interface. Such a two-dimensional salt solution is realized, for instance, by membranes consisting of cationic and anionic lipids [18-22, 49, 50]. Netz [79] shows that, though the interface on average is still charge neutral, this planar accumulation of ions may lead to additional electrostatic attraction between the wall and the colloid. Thus, the repulsive effect of image-charges tends to be less pronounced if there are mobile screening ions in the interface, but the distance dependences ($\sim \mathrm{e}^{-2\kappa h}/2\kappa h$) of the two effects are the same.

2.4. Approximate potentials with non-linear corrections

The BVP of the non-linear PB equation given in eq. (2.1) can only be solved numerically, and consequently, an analytical expression for the effective wall–colloid potential that is valid in a parameter regime where the non-linearity becomes important is not possible. And unfortunately, the condition $\phi < 1$ for linearization is rather restrictive, and most experiments are carried out in a parameter regime where this condition is not fulfilled. One way out of this problem is to make use of the charge renormalization concept, part of which has already been applied in the last section to take account of the finite size of the colloid. Further renormalization of charge is possible for the purpose of including, on a rather phenomenological level, non-linear effects [71]. Another way to go beyond linear theory is to use the few known solutions to non-linear problems in other geometries (for example, planar wall) in order to improve on the potentials

calculated in linear theory. That is what we want to do here, starting from eq. (2.45), which is valid for the case $\alpha = 1$ (the only case considered in this section). Since we can obtain the exact numerical solution of eq. (2.1) and with it the effective potential in non-linear theory, eq. (2.11), we can test in what parameter regime and to what extent these augmented potentials work. Testing of the validity of classical theories of effective colloidal pair potentials against accurate numerical results has been done in a similar way for two spheres in bulk [65, 89].

The BVP of eq. (2.1) can be solved analytically if there is no colloid in the electrolyte solution, but just a charged planar wall. The solution, due to Gouy–Chapman theory [9] can be written as

$$\phi^{GC}(z) = 4\,\mathrm{arctanh}[\mathrm{e}^{-\kappa z}\tanh(\Phi_w/4)] \tag{2.47}$$

with Φ_w being the potential at the wall. The derivative of this potential with respect to z at $z = 0$ is $-2\kappa\sinh\Phi_w/2$,which according to eq. (2.1) must be equal to $4\pi\lambda_B\sigma_w$. This gives the Graham equation [3, 9] relating the surface charge densities to the surface potentials:

$$4\pi\lambda_B\sigma_{w/c} = -2\kappa\sinh\Phi_{w/c}/2, \tag{2.48}$$

where we have additionally introduced the subscript, c referring to the colloidal charge densities and surface potentials. Using eq. (2.48), we introduce another abbreviation:

$$\gamma_{w/c} = |\tanh\Phi_{w/c}/4| = \tanh\left[\frac{1}{2}\,\mathrm{arcsinh}\left(\frac{2\pi\lambda_B\sigma_{w/c}}{\kappa}\right)\right]. \tag{2.49}$$

If $\kappa z > 1$, eq. (2.47) becomes

$$\phi^{GC}(z) = -4\gamma_w\mathrm{e}^{-\kappa z} \tag{2.50}$$

because γ_w cannot be larger than one. If $\Phi_w < 1$, eq. (2.50) reduces to the linear potential, eq. (2.40).

The second term in the interaction potential obtained in linear theory, eq. (2.45), is just the electrostatic energy of a point-charge Z in the unperturbed double layer of the charged wall. We can go beyond linear theory and improve this interaction potential just by taking $\phi^{GC}(z)$ of eq. (2.50) instead of $\phi^{\sigma_w}(z)$, eq. (2.40), in expression (2.44). This, along with the usual renormalization of charge Z/g_∞ (g_∞ from eq. (2.32)), leads to the potential

$$\beta V_{GCH}(h) = \frac{Z^2\lambda_B}{2(1+\kappa a)^2}\left(\frac{\mathrm{e}^{-2\kappa(h-a)}}{2h}\right) + \frac{Z4\gamma_w}{1+\kappa a}\mathrm{e}^{-\kappa(h-a)} \tag{2.51}$$

which henceforth we call the Gouy–Chapman-based (GCH-based) potential. If the surface potential of the wall becomes small, $\beta V_{GCH}(h)$ reduces to $\beta V_{LIN}(h)$ of linear theory, eq. (2.46), because $\phi^{GC}(z)$ reduces to $\phi^{\sigma_w}(z)$.

If $\kappa a \gg 1$, the colloidal sphere might be treated as a planar charged wall. We can then use eq. (2.47) to represent also the double layer due to the colloidal particle. Formally, this can be done by renormalizing the charge once more. Starting with eq. (2.29) with Z replaced by Z^*/g_∞ and requiring $\phi(a)$ to be just $\phi^{GC}(0)$ of eq. (2.50), one finds $Z^* = 4\gamma_c(1+\kappa a)a/\lambda_B$; see Ref. [71]. Using this Z^* instead of Z in eq. (2.51), we obtain

$$\beta V_{DJG}(h) = \frac{4\gamma_c^2 a^2}{h\lambda_B}\mathrm{e}^{-2\kappa(h-a)} + \frac{16a\gamma_c\gamma_w}{\lambda_B}\mathrm{e}^{-\kappa(h-a)}. \tag{2.52}$$

Conventionally, eq. (2.52) is derived by calculating the free energy of an electrolyte solution in between two parallel plates having surface charge densities σ_w and σ_c and then integrating over these energies to account for the curvature of the colloidal sphere (the Derjaguin approximation [2, 3]). However, we emphasize that this derivation gives only the second term in eq. (2.52), while the calculation here includes also the image-charge interaction terms. In the following, we will refer to the potential of eq. (2.52) as the Derjaguin-based (DJG-based) potential.

The derivation of the potentials in eqs (2.51) and (2.52) might appear rather *ad hoc*, and it is therefore an advantage that we can calculate correct mean-field interaction potentials to test the validity of $V_{GCH}(h)$ and $V_{DJG}(h)$. The most prominent deficiency of these two potentials is an obvious inconsistency: in just adding the image-charge to the direct interaction one has still relied on the superposition principle that is strictly valid only in linear theory, while introducing at the same time the double-layer potential of the non-linear Gouy–Chapman theory. One should therefore expect a good agreement with the potentials derived from PB theory only if the non-linearity is weak. In the highly non-linear regime, this inconsistency is almost bound to produce a substantial error, and, as we will see, the case can occur where it is even better to ignore the image-charge contribution than to include it in this inconsistent way.

We have now introduced four interaction potentials based on approximations that are valid in different parameter regimes. These are $V_{DJG}(h)$ of eq. (2.52), $V_{GCH}(h)$ of eq. (2.51), $V_{LIN}(h)$ of eq. (2.46), and, the limiting Stillinger potential $V_{St}(h)$ for the uncharged wall, eq. (2.37). By comparing each of them with the exact PB solution obtained from eq. (2.12), we aim to find out for what range of parameters these potentials are reasonably good approximations to the exact PB mean-field potential. There are again four parameters on which the four potentials depend, two specifying the surface charge densities of the wall and the colloid, and two for the size of the colloid and its distance to the wall, both in units of $1/\kappa$. While the latter two parameters are therefore just κa and κh, the first two are best expressed in terms of surface potentials, Φ_c and Φ_w, which can be obtained from eq. (2.48) for any given pair of surface densities. The parameters Φ_c and Φ_w are only used here for convenience and are not intended

to imply anything about the boundary conditions; we reiterate that we used constant-charge boundary conditions in all of the calculations. For eq. (2.51), we need a value for $Z\lambda_B\kappa$, which is also specified by Φ_c using $\sigma_c = Z/4\pi a^2$, then $Z\lambda_B\kappa = 2(\kappa a)^2|\sinh \Phi_c/2|$. To quantify the accuracy of the potentials under investigation, we define the relative percentage error

$$\% \text{ Error} = \left(\frac{\text{analytical} - \text{numerical}}{\text{numerical}}\right) \times 100. \tag{2.53}$$

This equation will reveal where the approximate theories overestimate (positive values) the interaction and where they are underestimated (negative values). Results are presented for various Φ_w:Φ_c ratios up to 4:4, for particle radius κa from 1 to 10 and minimum wall–particle distance $\kappa(h-a)$ up to 5. Table 2.1 relates some values of κa and $\Phi_{w/c}$ through the Graham relation, eq. (2.48) to $\sigma_{w/c}$, a and Z for an arbitrary screening length $\kappa^{-1} = 50$nm and Bjerrum length $\lambda_B = 0.715$. This gives us a feel of the bare parameters.

Table 2.1: Some values of the surface potentials $\Phi_{w/c}$ and κa with the corresponding surface densities $\sigma_{w/c}$, colloid radius, a and number of charge, Z, for an arbitrary screening length, κ^{-1} and Bjerrum length, λ_B.

$\kappa^{-1} = 50.0$nm and $\lambda_B = 0.715$nm				
$\Phi_{w/c}$	κa	$\sigma_{w/c}$ (nm^{-2})	a (nm)	Z
1.0	1.0	0.00232	50.0	73
2.0	2.0	0.00523	100.0	657
3.0	5.0	0.00948	250.0	7445
4.0	10.0	0.01615	500.0	50725

2.5. Further results and discussions

The Stillinger potential, $V_{St}(h)$: We begin the presentation of our results again with the case of an uncharged wall and concentrate on $V_{St}(h)$ of eq. (2.37) (which is identical to $V_{GCH}(h)$ and $V_{LIN}(h)$ when $\Phi_w = 0$). In Fig. 2.6(a), we compare this potential with the PB-based potential for $\Phi_c = 1.0, 1.5, 2.0$ taking a fixed value for κa of 5.0. Evidently, the Stillinger potential tends to systematically overestimate the correct potential. To quantify this error, we use the curves of Fig. 2.6(a) and calculate from eq. (2.53) the percentage error for all three values of Φ_c; the results are shown in Fig. 2.6(b). For $\Phi_c = 1.0$ the agreement between the PB-based potential and $V_{St}(h)$ is better than 10%

for nearly all wall–colloid distances ($\kappa(h-a) > 0.6$). Recalling that $\Phi = 1$ marks the value where the non-linearity becomes important, this is what one would have expected for the Stillinger potential, since it is derived in the linear approximation. For larger values of Φ_c, going up in the weakly non-linear regime only, we see that the Stillinger potential soon becomes rather poor, with a percentage error as high as 30% at all wall–colloid distances for a value of only $\Phi_c = 2.0$. So far we have just considered the case

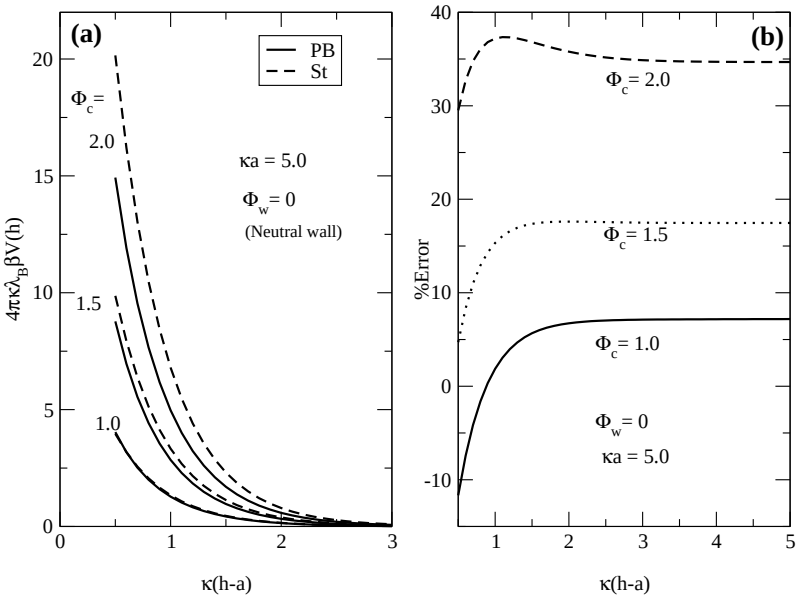

Figure 2.6: Uncharged wall, κa fixed: (a) The interaction potential versus the wall–colloid minimum separation, $\kappa(h-a)$; comparing the interaction potentials based on the approximate potential, eq. (2.37) (labeled St), to the that based on the numerical solution ("Exact") of the PB-BVP, eq. (2.1) (labeled PB). Different values of the reduced surface potential Φ_c of the colloid are considered. (b) The accuracy of the approximate potentials in (a), percentage error versus $\kappa(h-a)$.

$\kappa a = 5$. To get a more systematic overview of the accuracy of $V_{St}(h)$, in particular for different combinations of κa and κh, we now introduce a different form of presentation of our data, used first by Glendinning and Russel [83] and later extensively by Carnie *et al* [63, 65]. It is that of indicating in the parameter plane [κa:κh] the regions where the percentage error is less than 10%. In Fig. 2.7, we have plotted these lines of 10% error for the Stillinger case, for the three values of Φ_c already used in the previous figure ($\Phi_c = 1.0, 1.5, 2.0$). Each line in this plot separates a region in the [κa:κh] space where the magnitude of the error in $V_{St}(h)$ is under 10% from a region where it is greater than 10%. In this plot and all those of this type that follow, the arrows always point into the region where the error is under 10% and thus where the potential investigated is a reasonably good approximation to the exact PB-based potential. Since the Stillinger

potential $V_{St}(h)$ depends merely on three parameters, κa, κh, and Φ_c ($\Phi_w = 0$), Fig. 2.7 contains information on the error of $V_{St}(h)$ for *all possible* combinations of parameters. We produce such contour diagrams from error curves like those of Fig. 2.6(b). For

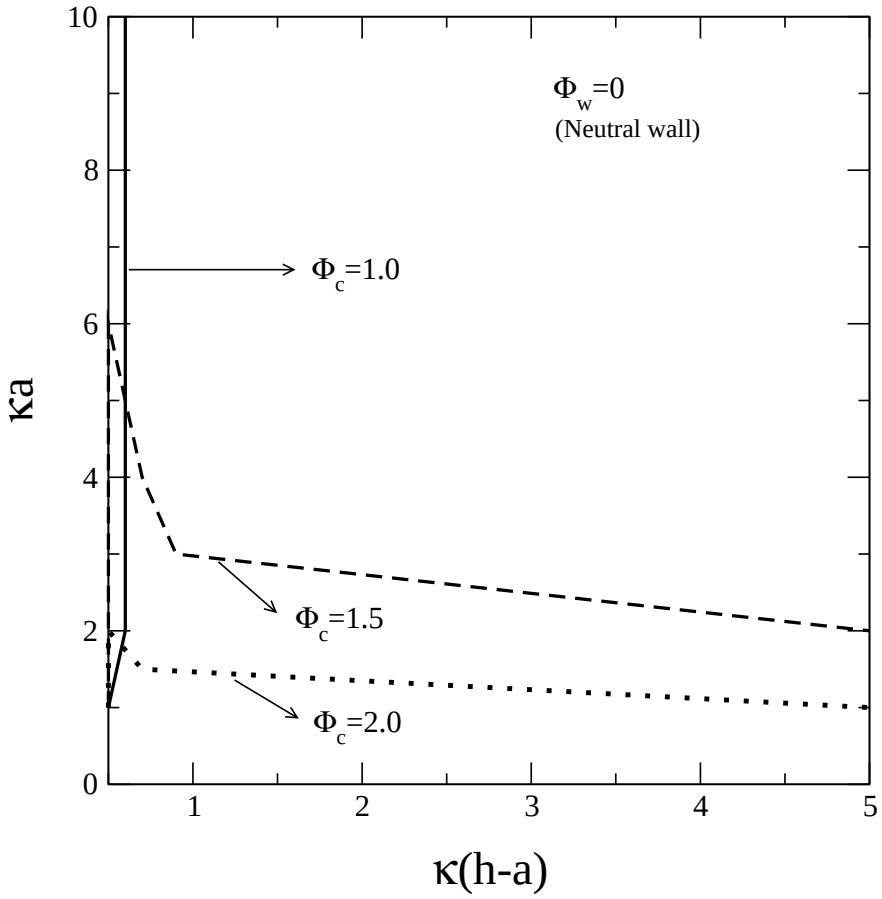

Figure 2.7: Uncharged wall ($\Phi_w = 0$): Regions in the $[\kappa a : \kappa h]$ parameter plane where the error of the approximate potential, eq. (2.37), is below 10%. Arrows point to the regions with under 10% error. The values of Φ_c are the same as in Fig. 2.6.

example, the error curve for $\Phi_c = 1.0$ in Fig. 2.6(b) is between -10% and $+10\%$ for $\kappa(h-a) > 0.6$, which is consistent with the solid line of Fig. 2.7 going through the point $(\kappa a, \kappa(h-a)) = (5.0, 0.6)$ and with the arrow on the solid line pointing into the region where $\kappa(h-a) > 0.6$. Fig. 2.7 shows clearly that the Stillinger potential, eq. (2.37), produces an error smaller than 10% for almost all values of κa as long as $\Phi_c \leq 1$ and $\kappa(h-a) > 0.6$. Thus we can make the general statement that the Stillinger potential is within 10% error over the whole linear regime ($\Phi_c \leq 1$) just as long as $\kappa(h-a) > 0.6$. For larger values of Φ_c, this potential soon fails, as we have already noticed in Fig. 2.6. For a moderately high value of the surface potential of only $\Phi_c = 2.0$, $V_{st}(h)$ has an

error below 10% only if κa is rather small ($\kappa a < 1$)—see the dotted line in Fig. 2.7—and this is true for all wall–colloid distances. For even higher values of Φ_c, the region of validity of the Stillinger potential in the $[\kappa a{:}\kappa h]$ plane will become even smaller, and at $\Phi_c = 3.0$ there is no point left in this plane where $V_{st}(h)$ has an error below 10%.

The linear potential $V_{LIN}(h)$ and the GCH potential $V_{GCH}(h)$: Let us now turn to the case where the wall bears surface charges ($|\sigma_w| > 0$). Fig. 2.8(a) compares the linear (eq. (2.46)) and the GCH (eq. (2.51)) interaction potentials, with the exact PB-based potential, again for $\kappa a = 5.0$ and $\Phi_c = 1.0$ and $\Phi_c = 2.0$ as in Fig. 2.6(a), but now with a surface wall potential of $\Phi_w = 1.0$. Again, the analytic potentials overestimate the correct potential for larger values of Φ_c, which is shown more clearly in Fig. 2.8(b), where the curves of Fig. 2.8(a) have been used to calculate the percentage error according to eq. (2.53). Again, for $\Phi_c = 1$, both potentials $V_{LIN}(h)$ and $V_{GCH}(h)$ show error less than 10% for almost all values of $\kappa(h-a)$, while the error for $\Phi_c = 2.0$ can reach values between 30% and 40%. Because the Stillinger potential is part of $V_{LIN}(h)$ and $V_{GCH}(h)$, this is what one would have anticipated from the failure of the Stillinger potential in this weakly non-linear regime found in Fig. 2.6(b). Figure 2.8(b) also demonstrates that $V_{GCH}(h)$ always has a smaller error than $V_{LIN}(h)$, a statement whose validity we have tested for a large number of input parameters. As $V_{LIN}(h)$ is merely a limiting case of $V_{GCH}(h)$ in the limit of small surface wall potentials, this is not surprising; it is still reassuring to know that the replacement of eq. (2.40) by $\phi^{GC}(z)$ of eq. (2.50) in the derivation of $V_{GCH}(h)$ does indeed mean an improvement of the potential. As $V_{LIN}(h)$ is thus contained in $V_{GCH}(h)$, we do not need to consider it any further and can instead concentrate on $V_{GCH}(h)$. An overview can again be obtained from a contour plot in the $[\kappa a{:}\kappa h]$ parameter plane, Fig. 2.9, showing regions where the error is under 10%. We have generated this contour plot by analyzing error curves like those given in Fig. 2.8(b). We tested eight different combinations of Φ_w and Φ_c, fixing the colloid surface potential at $\Phi_c = 1.0$ and varying Φ_w between one and four in Fig. 2.9(a), while fixing the wall potential and varying the colloid surface potential in Fig. 2.9(b). The two figures together now help us to identify the region of the four-dimensional parameter space where the GCH potential is a reliable and useful effective potential:

(i) As long as $\Phi_c \leq 1$ and $\kappa(h-a)$ is well above one, $V_{GCH}(h)$ is almost always a suitable potential, working well even for very large surface–wall potentials and showing only a very weak dependence on the colloidal size. That is what one can learn from Fig. 2.9(a).

(ii) If the colloid surface potential Φ_c is increased (Fig. 2.9(b)), the performance of $V_{GCH}(h)$ becomes poorer, and the region in the $[\kappa a{:}\kappa h]$ plane where $V_{GCH}(h)$ has

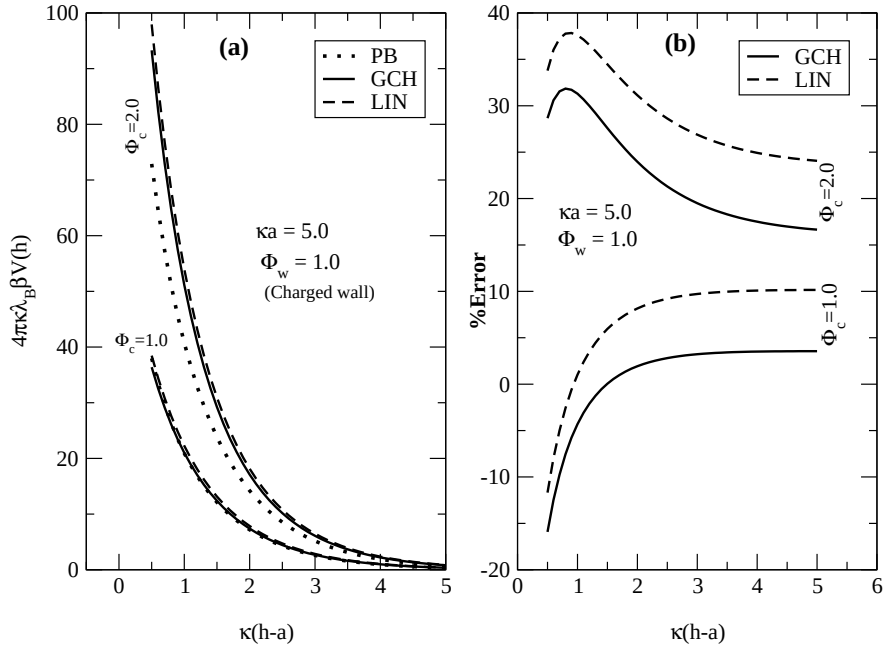

Figure 2.8: Charged wall, κa fixed: Comparison of the effective wall–colloid interaction potentials based on (i) the linear potential (LIN), eq. (2.46), (ii) the approximate potential (GCH), eq. (2.51), and (iii) the exact numerical solution of the PB-BVP. For a fixed wall–surface potential $\Phi_w = 1.0$, the colloid surface potential is varied from $\Phi_c = 1.0$ to $\Phi_c = 2.0$. (a) The interaction potential, $4\pi\lambda_B\kappa\beta V(h)$, versus the wall–colloid minimum separation, $\kappa(h-a)$. (b) The accuracy of the effective potentials in (a), percentage error versus $\kappa(h-a)$.

a small error shrinks. For example, if Φ_w:$\Phi_c \equiv 2$:2, $V_{GCH}(h)$ is useful only if κa is small ($\kappa a < 2$) (dashed–dotted line Fig. 2.9(b)).

It has earlier been pointed out that both approximate potentials, eq. (2.51) and eq. (2.52), suffer from the same basic problem. In linear theory, the total electrostatic potential around interacting charged objects in an electrolyte solution can be obtained just by adding the separate potentials for each object in isolation, and as a result of this superposition principle the effective interaction between the objects is a simple sum of terms associable with the different charge distributions. This is not valid in non-linear theory, and still both potentials, eq. (2.51) and eq. (2.52), are obviously based on this principle as they are sums of direct and image-charge interactions. One might wonder whether this inconsistency is responsible for the bad performance of $V_{GCH}(h)$ at high Φ_c, and whether or not the inclusion of the image-charge effect in eq. (2.51) improves the effective potential at all. Figure 2.10 clarifies this point. We plotted the percentage error of $V_{GCH}(h)$ for Φ_w:$\Phi_c \equiv 1$:1 and Φ_w:$\Phi_c \equiv 2$:2, with (solid line) and without (dashed line)

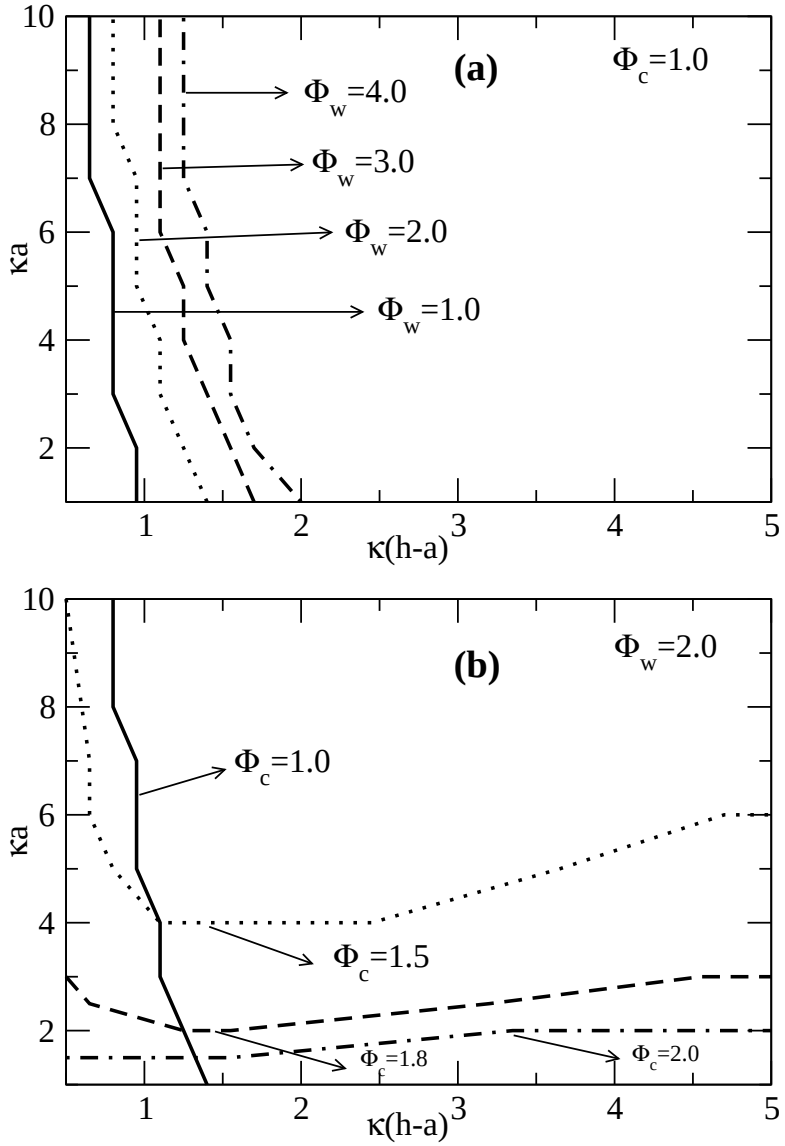

Figure 2.9: Charged wall, κa varies: an error contour diagram as in Fig. 2.7, but now for the GCH potential, eq. (2.51). The arrows point to the regions with under 10% error.

the first term in eq. (2.51). We first observe that both lines in both cases converge for larger values of κh; because the distance is too large for the image charge to have any effect at all (the image-charge interaction goes as $e^{-2\kappa(h-a)}$ and the direct interaction as $e^{-\kappa(h-a)}$). We furthermore observe that for Φ_w:$\Phi_c \equiv$ 1:1 inclusion of the image-charge contribution considerably improves the accuracy of the potential, in particular in the range $1 < \kappa(h-a) < 3$. The case Φ_w:$\Phi_c \equiv$ 2:2, on the other hand, shows that adding the image-charge term can also increase the error, thus demonstrating that the direct

and the image-charge interactions are not additive in the non-linear regime. But we also note that the error is still quite large even if the image-charge effect is ignored.

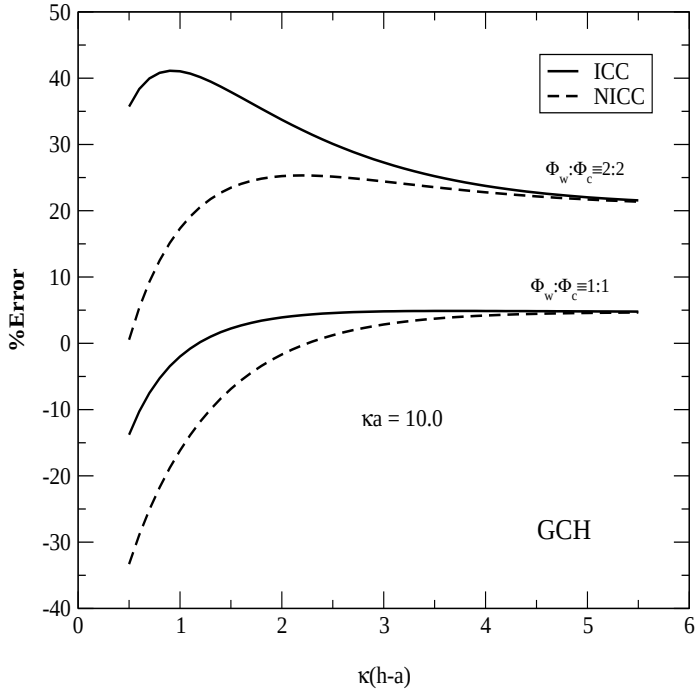

Figure 2.10: The contribution of image-charge term to the GCH potential, eq. (2.51), for two combinations of Φ_w:Φ_c, $\kappa a = 10.0$: the full lines show the error of the GCH potential calculated with image-charge contributions (ICC), while the dashed lines show the error calculated with no image-charge contributions (NICC).

Since it is the aim of this study not only to test approximate theories, but also to recommend for any given set of parameters $(\kappa a, \kappa h, \Phi_w, \Phi_c)$ a handy analytical expression that is as close as possible to the mean-field result, we have to check whether one may substantially enlarge the total region with an error below 10% in Fig. 2.9 by totally ignoring the image-charge effect. The answer is negative. For the specific combinations of parameters which we found $V_{GCH}(h)$ to be a suitable potential, we have explicitly tested that inclusion of the image-charge effect does indeed improve the agreement with the *exact* PB-based potential. This is not so for $V_{DJG}(h)$, which we discuss next.

The DJG potential $V_{DJG}(h)$: Like in Fig. 2.10, we check in Fig. 2.11 the importance of the image-charge interaction term, but now in the DJG potential $V_{DJG}(h)$. The same parameters as in Fig. 2.10 are used. Again, including the image-charge effect improves the result for Φ_w:$\Phi_c \equiv$ 1:1, but causes a larger error for Φ_w:$\Phi_c \equiv$ 2:2. In contrast to $V_{GCH}(h)$ in Fig. 2.10, $V_{DJG}(h)$ becomes better at larger distances when going from Φ_w:$\Phi_c \equiv$ 1:1 to Φ_w:$\Phi_c \equiv$ 2:2. One recognizes that for Φ_w:$\Phi_c \equiv$ 2:2 the error without

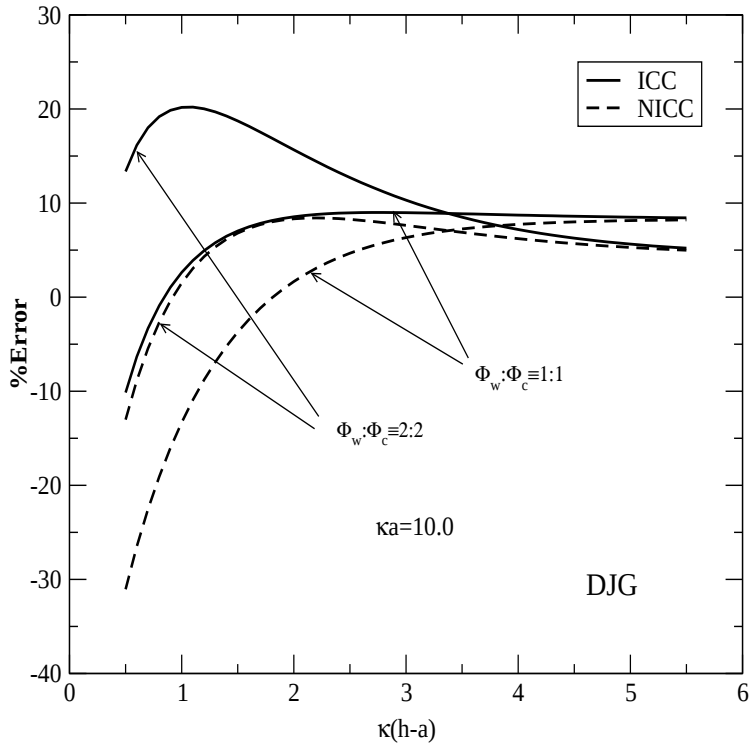

Figure 2.11: The contribution of the image-charge term to the DJG potential, eq. (2.52). The parameters are the same as in Fig. 2.10. The full lines show the error of the DJG potential calculated with image-charge contributions (ICC), while the dashed lines show that with no image-charge contributions (NICC).

the image-charge contribution remains well under 10%, while it goes up to 20% if the image-charge term is taken into account. This shows that naively adding the image-charge contribution can render a potential useless that would otherwise reproduce the mean-field result well (error $< 10\%$). We have checked this more systematically by producing 10% error contour maps as in Fig. 2.9 for the DJG potential with and without the image-charge contribution. We have found that for low values of Φ_c and/or low values of κa, the first term in eq. (2.52) is important. However, comparing the errors of $V_{DJG}(h)$ and $V_{GCH}(h)$ in this regime we have found that $V_{GCH}(h)$ generally produces a smaller error and is thus preferable to $V_{DJG}(h)$. On the other hand, in the parameter region where $V_{DJG}(h)$ performs better than $V_{GCH}(h)$, inclusion of the image-charge effect may considerably increase the error of $V_{DJG}(h)$, as seen for example in Fig. 2.11 for $\Phi_w{:}\Phi_c \equiv 2{:}2$. The conclusion to be drawn from this is that adding direct and image-charge interactions as is done in eq. (2.52) introduces an error that can sometimes be larger than the error that one produces by completely ignoring image charges. Of course, this conclusion is not meant to deny the existence of image-charges, nor is it

to say that they are unimportant; it just refers to the quality and usefulness of certain approximations. Moreover, it is true only in some region of parameter space relevant for the DJG potential. We therefore discard the image-charge term in eq. (2.52) in the following, and consider henceforth

$$\beta V_{DJG2}(h) = \frac{16a\gamma_c\gamma_w}{\lambda_B}\mathrm{e}^{-\kappa(h-a)}. \tag{2.54}$$

For this potential we present in Fig. 2.12 the 10% error contour plot in the $[\kappa a{:}\kappa h]$

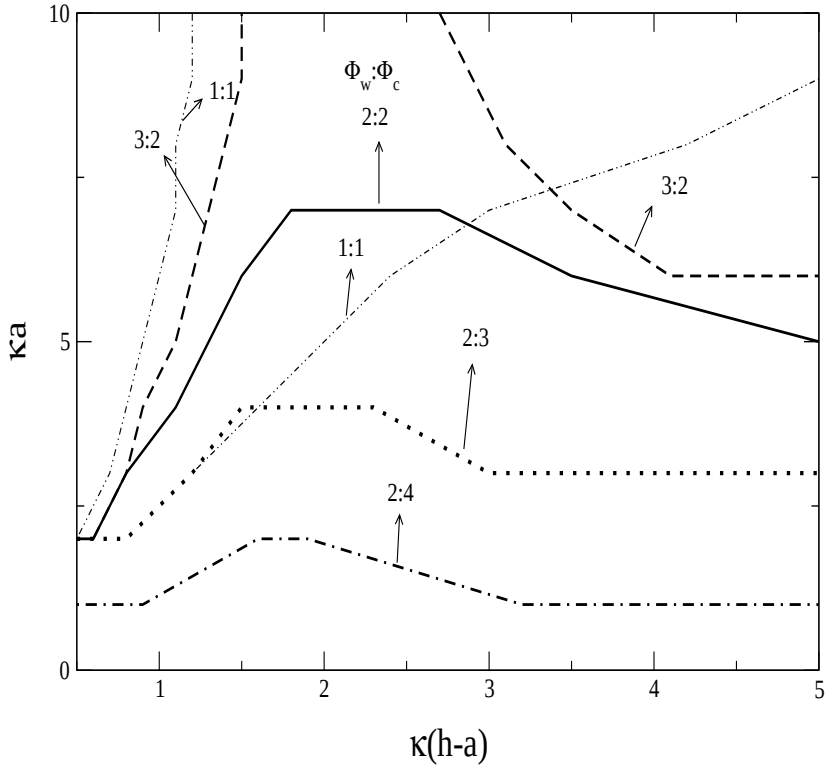

Figure 2.12: An error contour diagram as in Figs 2.7 and 2.9, but now for the DJG potential, eq. (2.54), for various combinations of $\Phi_w{:}\Phi_c$.

plane for various combinations of $\Phi_w{:}\Phi_c$. As is evident from this figure, the DJG potential becomes almost always tolerably good just provided that κa is sufficiently large. With increasing Φ_c the region with an error below 10% becomes larger, while it becomes smaller with increasing Φ_w. $\Phi_w{:}\Phi_c \equiv 4{:}2$ produces the same error boundary as $\Phi_w{:}\Phi_c \equiv 3{:}2$.

We have seen that $V_{GCH}(h)$ cannot be used if the colloidal surface potential is high and κa is at the same time large. But this is exactly the parameter regime where $\beta V_{DJG2}(h)$ performs exceedingly well. If one compares, for example, the $\Phi_w{:}\Phi_c \equiv$

2:2 error lines in Fig. 2.9 and 2.12, one can see that $V_{GCH}(h)$ and $\beta V_{DJG2}(h)$ are complementary in that $V_{GCH}(h)$ works for $\kappa a < 2$ while $\beta V_{DJG2}(h)$ is useful if κa is roughly greater than 5.

In summary, we have outlined the regions of validity of the three potentials $V_{St}(h)$, $V_{GCH}(h)$, and $\beta V_{DJG2}(h)$ using 10% error contour plots in Figs. 2.7, 2.9, and 2.12; this should be of use if one wishes to estimate the quality of one of the three potentials starting from a given set of input parameters $(\kappa a, \kappa h, \Phi_w, \Phi_c)$.

2.6. A TIRM experiment: a colloid near a wall

To demonstrate that the effective wall–colloid interaction potentials discussed here can actually be observed in an experiment, we want to close this chapter by briefly reporting the results of a recent TIRM (Total internal reflection microscopy) [52-57] experiment. The experimental detail is reported in [90]. Here we restrict ourselves to a rough sketch of the main idea of this experiment. A colloidal sphere (polystyrene; $a = 10$ μm) of unknown negative surface charge density σ_c is brought into a highly deionized (salt concentration in the μM regime) electrolyte solution. Due to gravitation, the particle sinks to the bottom of the glass container, and is thus located in the vicinity of a glass surface. This surface bears again an unknown amount of negative surface charges (σ_w), so there will be double layers both in front of the glass surface and surrounding the colloid. The colloid, being repelled by the repulsive double-layer forces and attracted by gravitation, will thus find a stable position at a finite distance from the glass interface, with small fluctuations in position due to Brownian forces.

When light is totally reflected at an interface, an evanescent field is created whose intensity I decays exponentially with distance z perpendicular to the interface, $I(z) = I_0 \mathrm{e}^{-\omega z}$, with ω being the inverse penetration depth of the evanescent wave. What is important here is that ω is a quantity known *a priori*. The central idea of the TIRM method now is to measure the scattered intensity of the interfacial colloidal particle, which is located in this evanescent wave, and to deduce the wall–colloid distance from the measured intensity through the known relation $I(z) = I_0 \mathrm{e}^{-\beta z}$. In order to obtain the spatial dependence of the potential energy of the particle, one has to measure the separation distances sampled by the colloidal sphere for a statistically long period of time. From this, the probability of finding the particle at any separation distance can be calculated; it is related to the potential energy via the Boltzmann distribution. This potential energy is the sum of the gravitational and double-layer potentials. Fig. 2.13(a) shows the measured potentials for ten different salt concentrations (10 nm $< \kappa^{-1} <$ 100 nm) when the gravitational contribution is subtracted.

Thus, Fig. 2.13(a) represents a direct experimental observation of what we have discussed in this chapter: the effective wall–colloid potentials due to double-layer forces.

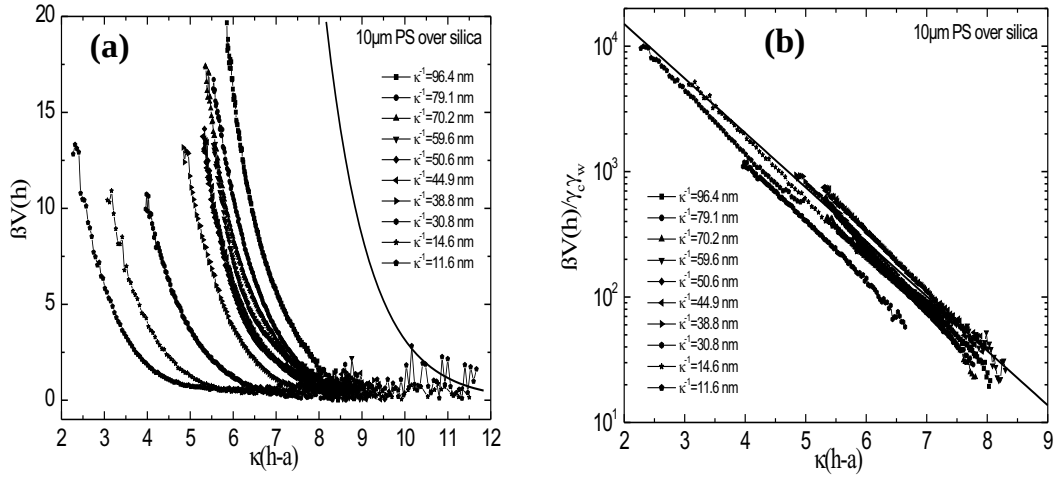

Figure 2.13: (a)Effective double-layer potentials between a glass surface and a colloidal sphere, experimentally determined for various salt concentrations using the TIRM method [90]. The function $16ae^{-\kappa(h-a)}/\lambda_B$ is plotted as solid line. (b) The potentials of (a) divided by $\gamma_w\gamma_c$ all collapse onto the simple function $16ae^{-\kappa(h-a)}/\lambda_B$, appearing as the solid line in the logarithmic plot. Thus, the interaction potential in eq. (2.54) is experimentally confined.

To find out which of the approximate potentials, eq. (2.51) or eq. (2.54), is appropriate for this experiment, we need to specify the surface potentials using eq. (2.48), which however is possible only if we know the surface densities σ_c, σ_w. In Ref. [90], explanation on how to use such salt-dependent measurements of double-layer forces to determine surface densities is given. We find that Φ_w and Φ_c are both of the order of one. While these values lie within the range studied theoretically here, the values of κa are not. The double layers in the experiment were extremely thin, with values of κa ranging between 50 and 500, which is far beyond the range studied in Figs. 2.9 and 2.12. Such high values of κa cannot be calculated with our numerical scheme for solving the PB equation, and one thus depends on extrapolating a sequence of error curves for increasing κa. The general trend of Fig. 2.12 suggests that since the DJG potential in eq. (2.54) seems to work for every combination of Φ_w:Φ_c just as long as the κa-value is large enough, the agreement with the PB theory should become better as the κa-value becomes larger. This is indeed the case, as shown in Ref. [90] for a set of parameters adapted to the experimental conditions. The calculation shows

that the potential, eq. (2.54), should be almost identical to the full mean-field result in the parameter regime under consideration. As for the image-charge contribution, we found that it becomes less important as κa becomes higher, and Fig. 2.11 shows that at $\kappa a = 10.0$ the image-charge contribution for Φ_w:Φ_c = 1:1 already has a rather small effect in the distance regime explored experimentally ($\kappa(h-a) > 2$). Thus in the experiment with $\kappa a > 50$, the colloid is too large and too far away from the surface to be sensitive to image-charge repulsion, and eq. (2.54) should be appropriate.

Recalling that the $\gamma_{w/c}$-factors in the potential, eq. (2.54) still depend on the salt concentration—see eq. (2.49)—we now understand that the salt dependence of the interaction potentials observed in Fig. 2.13(a) comes in through the product $\gamma_w\gamma_c$ in the interaction potential. Given the values of σ_w and σ_c, we can determine $\gamma_w\gamma_c$ for all measured salt concentrations. Dividing each experimentally determined potential in Fig. 2.13(a) by the product $\gamma_w\gamma_c$, we see in Fig. 2.13(b) all ten potential curves collapsing onto one master curve (solid line), which is just the function $\beta V(h)/\gamma_c\gamma_w = 16a\mathrm{e}^{-\kappa(h-a)}/\lambda_B$. The agreement is remarkably good and demonstrates quite interestingly, that the wall–colloid interaction potential of eq. (2.54) can be measured experimentally.

2.7. Summary and conclusions

We have been concerned with the question of how a charged sphere inside an electrolyte solution of dielectric constant ϵ interacts with a charged wall of dielectric constant ϵ'. We first considered the colloidal sphere as a point-charge, and discussed its interaction with both an uncharged and a charged wall. Renormalizing the charge by a factor g_h, one can afterwards correct these interaction potentials to account for the finite size of the colloidal sphere. Starting from these linear potentials, and making use of the known solution of the one-dimensional non-linear PB problem, we arrived at two potentials: eq. (2.51) (GCH potential) and eq. (2.52) (DJG potential) approximately valid also in the non-linear regime. The range of validities of these analytic approximate potentials were then checked by comparing them with the exact interaction potentials obtained from the full numerical solution of PB-BVP, eq. (2.1). We may summarize the main points as follows:

For an uncharged wall of dielectric constant ϵ', the effective wall–colloid potential is repulsive if $\epsilon'/\epsilon \to 0$ and attractive if $\epsilon/\epsilon' \to 0$. A charged colloid in an aqueous suspension will therefore be repelled from e.g. an air-water interface, and attracted to e.g. a metal-water interface. In contrast to conclusions in Refs [59] and [40], there is no electrostatic attraction of colloids to an $\epsilon'/\epsilon < 1$ interface. Even if there are no

image-charges present ($\epsilon' = \epsilon$), a colloid is still repelled from an uncharged interface due to a confinement effect. The h-dependent renormalization factor g_h is found to be negligibly different from g_∞. In linear theory and if $\epsilon'/\epsilon \to 0$, the interaction of a colloid of finite size with an uncharged wall is just half of the usual repulsive Yukawa double-layer potential of DLVO theory between two like-charged spheres (see eq. (2.37)), where one sphere is the screened colloid at $z = h$ and the other, being located at $z = -h$, represents nothing but the screened image of the colloid. Then only the factor 1/2 in the potential remains as a reminder of the fact that we are concerned not with a colloid–colloid interaction, but with a wall–colloid interaction. One can reuse Stillinger's potential for a point-charge near an uncharged wall as the Green's function for the linearized PB equation for the case of an arbitrary distribution of fixed charges. Using the point-charge approximation, the effective potential is then a sum of the potential for an uncharged wall and the interaction of the colloid with the unperturbed double layer of the wall. We checked the validity of $\beta V_{st}(h)$ for the uncharged wall and found that it produces an error under 10% for all values of κa as long as $\kappa(h-a) > 0.61$ and $\Phi_c \leq 1$. Adding to $\beta V_{st}(h)$ the interaction energy of a renormalized point-charge Z/g_∞ in the unperturbed Gouy–Chapman layer, we arrive at the GCH potential, eq. (2.51), which we have found to be appropriate for all κa provided that $\kappa(h-a) > 2$ and $\Phi_c \leq 1$, in accord with the range of validity found for $\beta V_{st}(h)$ alone. We have explicitly checked that inclusion of the image-charge contribution improves the accuracy. If $\Phi_c > 1$, the DJG potential, eq. (2.52), without image-charge contributions is almost always tolerably good for all $\kappa(h-a)$ provided only that κa is sufficiently large (error under 10% if $\kappa a > 6$ for $\Phi_w{:}\Phi_c \equiv 2{:}2$). With increasing Φ_c this region with error below 10% becomes larger, while it becomes smaller with increasing Φ_w. A TIRM experiment to measure the effective wall–colloid potential was found to be in good agreement with the DJG potential.

We note that when a suspension of colloids is considered, the wall–colloid interaction potential considered here will compete with the colloid–colloid interaction potential, with neighbouring colloids in the bulk. If the latter is more repulsive as in the case of an uncharged wall with $\epsilon'/\epsilon > 0$, the interfacial colloid may experience an attractive force towards the wall. This situation is the subject of chapter 5, where the problem is addressed via the cell model approximation.

2.8. Appendix

2.8.1. Force via the stress tensor

The force $\vec{F}$ acting on a particle enclosed by a surface S can be calculated by integrating the stress tensor $\vec{\vec{T}}$:

$$\vec{F} = \int_S \mathrm{d}S\vec{\vec{T}} \cdot \mathbf{n} \tag{2.55}$$

where $\mathbf{n}$ is a unit normal pointing into the surface. Here the total stress tensor is the sum of an osmotic pressure term and a Maxwell stress

$$\vec{\vec{T}} = \left(\Pi + \frac{\epsilon}{8\pi}\mathcal{E}^2\right)\vec{\vec{I}} - \frac{\epsilon}{4\pi}\vec{\mathcal{E}}\vec{\mathcal{E}}. \tag{2.56}$$

$\vec{\mathcal{E}}$ is the electric field, $\vec{\vec{I}}$ is a unit tensor, and Π is the difference in local osmotic pressure from that in the bulk electrolyte:

$$\beta\Pi = (\rho_+ + \rho_-) = 2c_s(\cosh\phi - 1), \tag{2.57}$$

c_s being the familiar bulk salt concentration. Rewriting the stress tensor in thermal energy units (with also $\vec{E} = e\beta\vec{\mathcal{E}}$) we have

$$\beta\vec{\vec{T}} = 2c_s(\cosh\phi - 1) + \frac{1}{8\pi\lambda_B}\left[E^2\vec{\vec{I}} - 2\vec{E}\vec{E}\right]. \tag{2.58}$$

Since the system is symmetrical about the axis, z, passing through the centres of the colloid and normal to the wall, see Fig. 2.2(a)), the direction of the force on the particle is normal to the wall, i.e.

$$\beta F_z = \int_{S_\eta} \mathrm{d}S_\eta \ \vec{e}_z.\beta\vec{\vec{T}}.\mathbf{n} \ . \tag{2.59}$$

In the BSC system, the enclosing surface S_η is an η-coordinate surface ($\eta_0 \leq \eta \leq \eta_c$), where $\eta = \eta_0 = 0$ and $\eta = \eta_c$ coincide with the wall and the colloid surfaces respective (see Fig. 2.1). $\mathbf{n}$ is a unit vector normal to the η-coordinate surface, $\mathbf{n} = \vec{e}_\eta$, where $\vec{e}_\eta$ and also $\vec{e}_\theta$ are the corresponding unit vectors in the BSC system: $\vec{e}_\eta = \partial_\eta\mathbf{r}/\left|\partial_\eta\mathbf{r}\right|$ and $\vec{e}_\theta = \partial_\theta\mathbf{r}/\left|\partial_\theta\mathbf{r}\right|$

with $\mathbf{r} = s(\eta,\theta)\vec{e}_s + z(\eta,\theta)\vec{e}_z$. Therefore,

$$\vec{e}_z \cdot \vec{\vec{T}} \cdot \mathbf{n} = \vec{e}_z \cdot \vec{\vec{T}} \cdot \vec{e}_\eta = T_{\eta\eta}\ \vec{e}_z \cdot \vec{e}_\eta + T_{\theta\eta}\ \vec{e}_z \cdot \vec{e}_\theta. \tag{2.60}$$

Using eq. (2.5),

$$\vec{e}_\eta \cdot \vec{e}_z = \frac{1-\cosh\eta\cos\theta}{\cosh\eta-\cos\theta}$$
$$\vec{e}_\theta \cdot \vec{e}_z = -\left(\frac{\sinh\eta\sin\theta}{\cosh\eta-\cos\theta}\right). \tag{2.61}$$

and with

$$\int \mathrm{d}S_\eta = \int 2\pi \frac{(\kappa b)^2\sin\theta}{(\cosh\eta-\cos\theta)^2}\,\mathrm{d}\theta \tag{2.62}$$

eq. (2.59) then becomes

$$\beta F_z = 2\pi\int_0^\pi \left\{\left[2c_s(\cosh\phi-1)+\frac{1}{8\pi\lambda_B}(E_\theta^2-E_\eta^2)\right]\frac{1-\cosh\eta\cos\theta}{\cosh\eta-\cos\theta} + \left[\frac{1}{4\pi\lambda_B}E_\eta E_\theta\right]\frac{\sinh\eta\sin\theta}{\cosh\eta-\cosh\theta}\right\}\frac{(\kappa b)^2\sin\theta}{(\cosh\eta-\cos\theta)^2}\;\mathrm{d}\theta. \tag{2.63}$$

Recalling that $c_s = \kappa^2/8\pi\lambda_B$ and choosing the enclosing surface S_η to be the interfacial wall corresponding to $\eta = 0$, the dimensionless force on the colloid $f = 4\pi\lambda_B\beta F_z$ takes the form

$$f = \pi\int_0^\pi \mathrm{d}\theta\;\left[2\kappa^2(\cosh\phi-1)+E_\theta^2-E_\eta^2\right]\frac{(\kappa b)^2\sin\theta}{(1-\cos\theta)^2}. \tag{2.64}$$

The electric field $E_{\eta/\theta}$ can be written in terms of ϕ:

$$bE_\eta = (1-\cos\theta)\,\partial_\eta\phi$$

$$bE_\theta = (1-\cos\theta)\,\partial_\theta\phi$$

and substituting this in eq. (2.64) we finally write the reduced force as

$$f = \pi\int_0^\pi \mathrm{d}\theta\left(\frac{2(\kappa b)^2\sin\theta}{(1-\cos\theta)^2}(\cosh\phi-1)+\left[\partial_\theta\phi^2-\partial_\eta\phi^2\right]\sin\theta\right)_{\eta=0}. \tag{2.65}$$

Noting that $\partial_\eta\phi$ at $\eta = 0$ is known from our boundary condition, we have that

$$\begin{aligned}\partial_\eta\phi^2\big|_{\eta=0} = (\partial_\eta\phi^{GC})^2\big|_{\eta=0} &= \left(\frac{2\kappa b}{1-\cos\theta}\right)^2\sinh^2\Phi_w/2\\ &= \frac{1}{2}\left(\frac{2\kappa b}{1-\cos\theta}\right)^2(\cosh\Phi_w-1)\end{aligned} \tag{2.66}$$

and we can simplify eq. (2.65) to

$$f = \pi\int_0^\pi \mathrm{d}\theta\left(\frac{2(\kappa a\sinh\eta_c)^2\sin\theta}{(1-\cos\theta)^2}[\cosh\phi-\cosh\Phi_w]+\left(\frac{\partial\phi}{\partial\theta}\right)^2\sin\theta\right)_{\eta=0}. \tag{2.67}$$

This force can be calculated once ϕ is known. All of the error estimates of the analytical potentials obtained in this chapter were made on the basis of the force, f. Where potentials are plotted, we have obtained them from numerically integrating the forces.

3

Effective interaction: A charged colloid with an air-water interface

3.1. Introduction

In the preceeding chapter, we addressed via PB theory the problem of the effective interaction of a charged colloidal sphere in an electrolyte solution, with an interface formed between the solution and an interfacial wall, where such a wall is assumed to be hard, i.e. the colloid is not allowed to penetrate the wall. Here in this chapter, the same formalism is being employed to extend the investigation to the case of a penetrable interface, specifically, the air-water interface. The main idea is to clarify the role of electrostatic double layer forces in the observed trapping of certain charged particles at the air-water interface.

Colloidal particles can be trapped at the interface between two fluids. A direct microscopic observation of stable 2D colloidal crystals of polystyrene spheres at the air-water interface was first reported by Pieranski [12]. Since then, the study of 2D colloidal particle at the air-water interface has afforded the possibility of investigating in two dimensions such interesting problems as crystallization, melting, aggregation, phase separation e.t.c. [16, 33, 34, 91-96].

We have mentioned earlier that colloidal systems can serve as good models for some biologically oriented questions e.g., crystallization of proteins and other macromolecules often referred to as biocolloids. Adsorption of proteins generally at fluid-fluid interfaces and their behaviour in the adsorbed state play an important role in the formulation

and stabilization of different foam-based and emulsion based products in the food and drug industries [97-99].

Most of the above cited studies deal mainly with the various interparticle interactions between colloids already stable at the interface. These interactions lead to the various structural and phase behaviour, as we shall also investigate in the next chapter. There are however, very few reliable studies on the interaction of colloids in solution with the air-solution interface. The present chapter focuses just on this interface–colloid interactions, and here, in particular, the effective interaction of electric double layer origin, between a charged colloidal particles with an air-water interface.

Hurd [13] investigating the effective pair interaction potential of trapped charged colloids, has defined interfacial colloids as consisting of particles dispersed on an interface between two fluid media and held there by surface tension. This definition follows perhaps from the work of Ref. [12] where it is concluded that a polystyrene latex sphere is trapped at the air-water interface in a huge surface tension energy well which dominates by many orders of magnitude, any thermal or gravitational fluctuations present. The influence of electrostatic forces for the charged latex particle, however, was totally ignored in this analysis as regards the trapping. We will show in the present chapter that the electrostatic contribution to keeping a colloid at the interface is also very small compared to the surface energy trap. But it (electrostatics) however, provides an important barrier to spontaneous precipitation of the colloids in the vicinity of the interface.

We have shown from the results of chapter 2 that a particle approaching a neutral interface between two media of different dielectric constants (such as air-water) experiences repulsive image-charge force, if it does so from the medium with the higher dielectric constant (see e.g., sec. 2.3.1, Fig. 2.6). This electrostatic energy barrier is in the focus of this chapter. We calculate its height and salt-dependence within the framework of PB theory in the same manner as in chapter 2.

3.2. Formalism

3.2.1. Effective interaction: non-linear theory

Our model system illustrated in Fig. 3.1 is similar to Fig. 2.1, but with the ϵ'-ϵ boundary definitely an air-water interface penetrable to the colloids. For air, $\epsilon' = 1$ is very small compared to water, $\epsilon \approx 80$ that we again approximate the ratio ϵ'/ϵ to zero. The colloidal particle of radius a is assumed to bear a fixed surface charge density, $-e\sigma$,

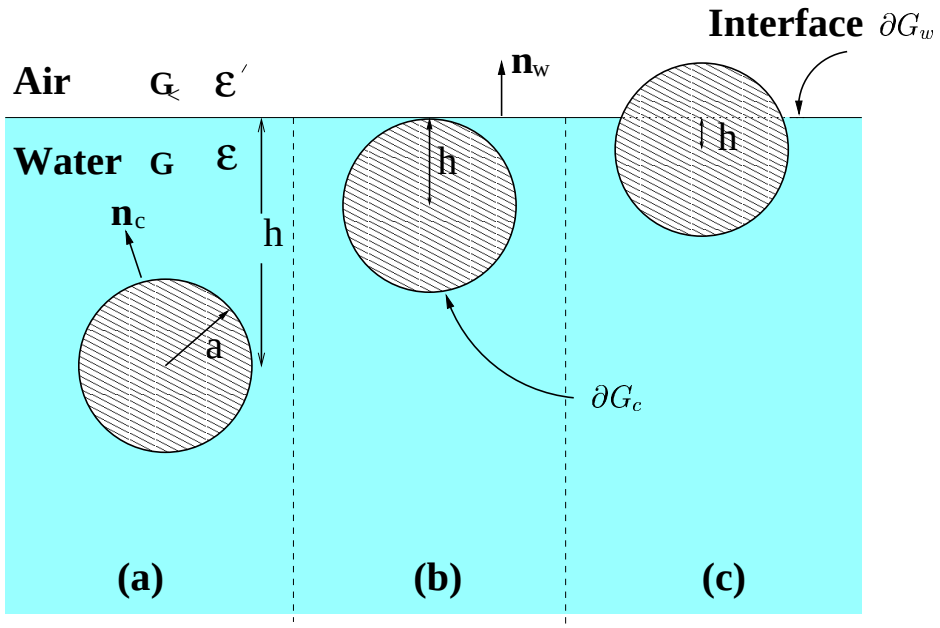

Figure 3.1: The model system: A colloidal sphere of uniform surface charge density $-e\sigma$ and radius a inside an electrolyte (water) of dielectric constant ϵ, and a distance h from an interface formed by air of dielectric constant ϵ'. (a) The colloid is completely immersed in the electrolyte ($h > a$), (b) the colloid just touches the interface ($h = a$), and (c) the colloid emerges at the interface ($h < a$).

which when totally immersed in water ($h \geq a$) bears Z ($= 4\pi a^2\sigma$) fixed negative homogeneously distributed charges, while the confining air-water interface bears no surface charges.

We point out the controversy in the literature that the air-water interface can be associated with some surface charges. This is supposedly due to the preferred orientation of interfacial water molecules. It has been reported that as a result of this orientation, a thin electric double layer at the interface is established with the outermost portion (facing the gas phase) of the double layer being negative and the innermost part (facing the liquid phase) being positive [100-102]. Sengupta and Damodaran [97] have given the value of the inner potential as about 184.7mV. On the other hand, works involving air bubbles in water report that the bubble-water surface potential (facing the liquid phase) is negative and of value -25 ± 10mV [103]. Ducker [104] lamenting the uncertainty in the exact magnitude of the potential (air-water interface) assumed values from zero to -25 mV. Even if we assume an air-water interface of oppositely charged layers, the electric flux through any surface enclosing such layers is zero and hence it is more accurate to assume that the interface is electrically neutral and bears no net surface charges, as we have done here. It is also noteworthy that Wagner [87],and

Onsager and Samaras [88] also treated the air-water interface as being charge neutral in related studies.

With the above characterizations, the PB-BVP of eq. (2.1) now becomes,

$$\begin{array}{ll} \nabla^2\phi = \kappa^2 \sinh\phi & \mathbf{r} \in G \\ \mathbf{n}_c \nabla\phi = 4\pi\lambda_B\sigma & \mathbf{r} \in \partial G_c \\ \mathbf{n}_w \nabla\phi = 0 & \mathbf{r} \in \partial G_w \\ \phi = 0 & \mathbf{r} \to \infty \end{array} \tag{3.1}$$

where the symbols and notations retain their definitions in eq. (2.1) except the colloids surface charge density which here is just σ.

Equation (3.1) is solved for three cases corresponding to colloid position in the water relative to the air-water interface in different coordinate systems suitable for the interface–colloid configuration as follows:

(a) Colloid wholly in solution ($h > a$; Fig. 3.1(a)): the bispherical coordinate (BSC) system (η, θ, φ).

(b) Colloid in solution but just touching the interface ($h = a$; Fig. 3.1(b)): the tangent-sphere coordinate (TSC) system (μ, ν, φ).

(c) Colloid partly in solution and partly in air ($0 < h < a$; Fig. 3.1(c)): the toroidal coordinate (TOC) system $(\alpha, \omega\varphi)$.

The BSC coordinate system as mentioned earlier, has been frequently used for calculating the effective interaction between two charged spheres in bulk solution and also in the preceeding chapter for the interaction between a colloidal sphere and a charged or uncharged hard planar interface. A description has been given sec. 2.2.1. The use here of the TOC and TSC systems are quite new and some details are given in Appendix A (sec. 3.5.1). The reason and advantage of choosing the various coordinate systems have been emphasized. In trying to transform the complex boundaries of the system as they appear in the ordinary Cartesian coordinates to simple geometries, a coordinate system that works well in the BVP numerical scheme for a particular set of interface–colloid separation distance breaks down for another set. Figure 3.2 shows the correspondence between the BSC and TOC schemes, where we have plotted the potential profiles along the radial axis (interface), s $(= \sqrt{x^2 + y^2})$ and along the axis of symmetry, z. In Fig. 3.2(a), along the interface, the potential $\phi(s)$ increases in magnitude for decreasing interface–colloid separation given as κh, as expected. As the particle barely penetrates the interface, $\kappa h = 4.8 < \kappa a$, $|\phi(s)|$ deeps more, and then begins to depreciate as κh decreases further. Figure 3.2(b)) shows the potential

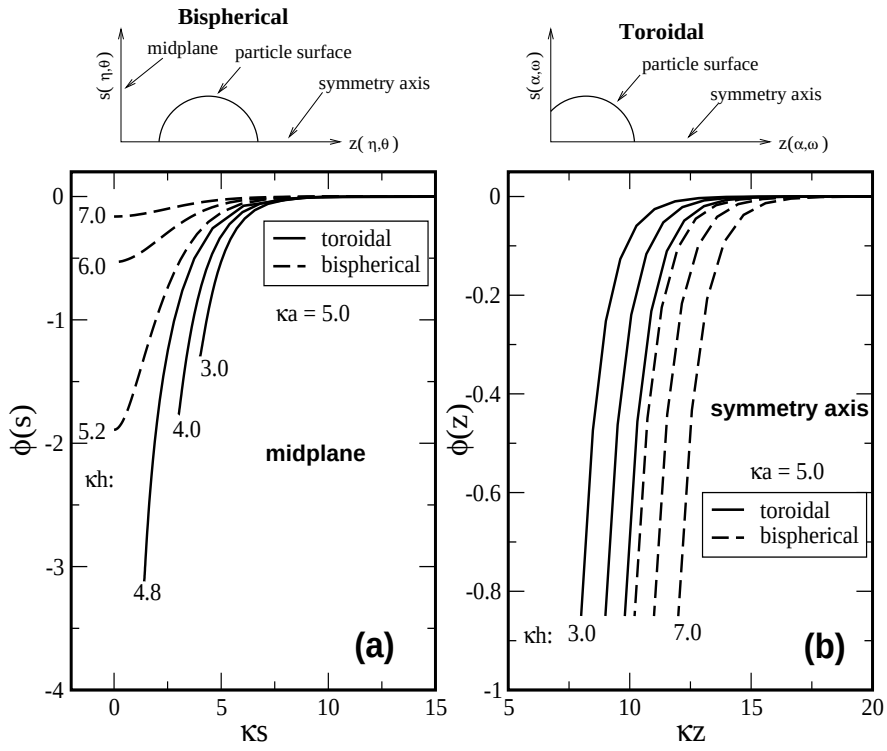

Figure 3.2: The potential, ϕ along different axis with the bispherical and toroidal coordinate schemes, for particle radius, $\kappa a = 5.0$, and various interface–colloid separation distance, $\kappa h = 3.0,\ 4.0,\ 4.8$ (toroidal) and $\kappa h = 5.2,\ 6.0,\ 7.0$ (bispherical): (a) along the midplane (interface), $\kappa s(\alpha, \omega)$ — toroidal and $\kappa s(\eta, \theta)$ — bispherical. (b) along the side of the symmetry axis, $\kappa z(\alpha, \omega)$, $\kappa z(\eta, \theta)$ as indicated in the upper illustration.

profiles along the symmetry axis (z) on the right side of the particle as indicated in the upper illustrative diagram. The profiles as expected show no sensitivity to the interface–colloid separation, the shift between any two curves being just the difference in the separation distances (κz). The increase and decrease in $\phi(s)$ at the interface will be discussed in sec. 3.3. The curves of Fig. 3.2 are only intended to show that there is no error in switching coordinate systems.

Once ϕ is known we proceed to calculate the grand potential, Ω_h of the system as given as eq.(2.11), chapter 2. The effective interface–colloid interaction $\beta V(h)$ is the total change in the grand potential when the particle is brought to a finite distance h near the interface from infinity.

$$\beta V(h) = \beta\Omega_h - \beta\Omega_{\pm\infty}\ , \tag{3.2}$$

where $\Omega_{+\infty}$ can be determined by solving the PB problem for an isolated particle in the bulk electrolyte solution, in spherical coordinate system. It can also be obtained from

solution in BSC by taking a sufficiently large interface–colloid separation ($h \to \infty$). When the colloids is completely removed from the solution to the air, where we assume it bears no surface charges, therefore $\Omega_{-\infty} = 0$

3.2.2. The no-screening limit

Our numerical schemes for solving the BVP, eq. (3.1) and hence the grand potential works well for various microion concentrations characterized by κ, except for the case $\kappa = 0$ (no screening) when convergence problems occurs. Though not realistic, the case $\kappa = 0$ is still interesting, not only as a limiting case, but also as an introduction to the following section.

The effective potential in the salt-free limit, $V^0(h)$, consists only of the self energy of the particle's fixed charges in their own Coulomb potential,

$$\beta V^0(h) = \beta\Omega_h^{self} - \beta\Omega_\infty^{self} \tag{3.3}$$

with the self-energy

$$\beta\Omega_h^{self} = -\frac{1}{2}\int_{\partial G_c} dS\, \sigma(\mathbf{r})\phi_h^0(\mathbf{r}) \tag{3.4}$$

where ϕ_h^0 is the potential due to the colloidal surface charges. When $h \to \infty$, the potential has perfect spherical symmetry and, for a colloid with a constant surface charge density $-\sigma e = -Ze/4\pi a^2$, one obtains $\phi^0(a) = -Z\lambda_B/a$ and thus

$$\beta\Omega_\infty^{self} = \frac{Z^2\lambda_B}{2a}, \qquad h \to \infty\,. \tag{3.5}$$

If the colloid is very close to the interface ($h \geq a$), the potential is no longer spherically symmetric since there is a jump in the dielectric constants at $z = 0$, requiring that $\nabla\phi = 0$ at $z = 0$ when $\epsilon'/\epsilon \simeq 0$. This boundary condition can conveniently be satisfied using the method of image-charges. If $\epsilon'/\epsilon \simeq 0$ and if we approximate the colloid by a point-charge, the colloidal image-charge is of the same sign and magnitude as the colloidal charge. The separation distance between the real and image-charges is $2h$, and the resulting potential, $\beta\Omega_h^{image} = Z^2\lambda_B/4h$, (see sec. 5.3.1 for details). One then obtains,

$$\begin{aligned} \beta\Omega_h^{self} &= \beta\Omega_h^{image} + \beta\Omega_\infty^{self} \\ &= \frac{Z^2\lambda_B}{2}\left(\frac{1}{2h} + \frac{1}{a}\right), \qquad h \geq a. \end{aligned} \tag{3.6}$$

The next stage is reached when the colloidal particle breaks through the air-water

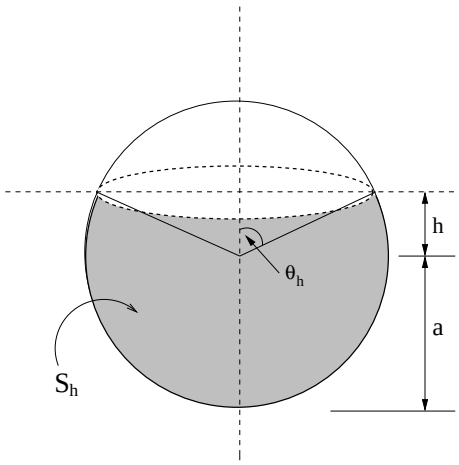

Figure 3.3: S_h is the surface area of the part of the colloid in water (the shaded surface), $S_h = 2\pi a(a+h) = 2\pi a^2(1+\cos\theta_h)$. If $S_\infty = 4\pi a^2$ is the surface area of the whole colloid, the charge on the wetted part, Z_h is defined such that $Z_h/Z = S_h/S_\infty$, where Z is the bulk charge.

interface ($h < a$). We assume that the total charge on the particle falls as the de-wetted surface. We note that this assumption is not explicit in the BVP numerical schemes where the colloid surface charge, σ remains constant as long as part of it is in contact with the solution. Assuming uniform wetting or de-wetting without meniscus, the now h-dependent total charge Z can be expressed as (see Fig. 3.3),

$$Z_h = \frac{Z}{2}(1 + h/a), \qquad |h| \leq a\,. \tag{3.7}$$

The electrostatic potential of this partially charged sphere in spherical coordinates reads

$$\phi_h^0(r,\theta,\varphi) = -\frac{Z\lambda_B}{4\pi}\int_{\theta_h}^{\pi} d\theta' \sin\theta' \int_0^{2\pi} \frac{d\varphi'}{\sqrt{\mathcal{R}}} \tag{3.8}$$
$$\mathcal{R} = r^2 + a^2 - 2ar\cos\theta\cos\theta' - 2ra\sin\theta\sin\theta'\cos\varphi',$$

where θ_h is the contact angle of the colloid with the air-water interface (see Fig. 3.3). Interestingly, numerical integration of eq. (3.4) with eq. (3.8) substituted, shows that the self energy (for $h < a$) can reasonably be approximated as,

$$\beta\Omega_h^{self} = \frac{Z_h^2\lambda_B}{2}\left(\frac{1}{2h'} + \frac{1}{a}\right), \qquad h < a \tag{3.9}$$

where we have just replaced Z in eq. (3.6) by Z_h, assumed now to be located at the center of the wetted part, h' from the interface. Here, h' is taken to be the radius of a sphere equivalent to the volume of the wetted part, V_h, and $V_h = \frac{\pi}{3}(h+a)^2[3a-(h+a)]$.

Applying eqs (3.6) and (3.9) in eq. (3.3), we thus arrive at the following approximate effective potential,

$$\beta V^0(h) = \begin{cases} \dfrac{Z^2\lambda_B}{4h} & h \geq a \\ \dfrac{Z_h^2\lambda_B}{2a}\left(1 + \dfrac{a}{2h'} - \dfrac{Z^2}{Z_h^2}\right) & |h| < a. \end{cases} \tag{3.10}$$

The interaction potential, eq. 3.10 sets the limit which that obtained from the numerical solution of the PB-BVP, eq. (3.1) should approach as $\kappa \to 0$.

In sec. 2.3, chapter 2, we have described how to obtain the effective interface–colloid interaction from Stillinger's [40] potential derived for a point-charge in an electrolytic solution (ϵ) near a neutral dielectric substrate (ϵ') using the linearized PB equation ($\nabla^2\phi = \kappa^2\phi$). If $\epsilon'/\epsilon \to 0$, the following Yukawa-like interaction potential is found

$$\beta V_{st}(h) = \frac{(Z/g_\infty)^2\lambda_B}{4h}\mathrm{e}^{-2\kappa \mathrm{h}} \qquad h \geq a \tag{3.11}$$

where g_{infty} (see eq. (2.32)) is just the DH charge renormalization factor to take care of the finite size of the colloidal particle. It is immediately seen that eq.(3.11) is consistent with eq. (3.10), as the $\kappa = 0$ limit of eq. (3.11) gives just the bare image-charge interaction $Z^2\lambda_B/4h$. The parameter regime of validity of eq. 3.11 have been tested extensively against the exact PB result in the previous chapter.

3.2.3. Other forces

It is important to emphasize that eq. (3.2) accounts only for the energy stored in the double-layer. As long as $h \geq a$, this is indeed equal to the total interaction energy between the colloid and the interface. However, when the colloidal particle breaks through the air-water interface, i.e. if $h < a$, additional contributions to the interaction energy should be considered. The most important of these additional energy terms, we denote by E_s – is due to capillary forces and is estimated further below. Other terms arise due to the fact that a part of the colloidal surface is exposed to air when $h < a$. Estimating these terms requires knowledge of some subtle details about the de-wetted colloid surface. We can only speculate about the precise state of charge of the de-wetted surface. Two cases mark the extreme: the de-wetted part remains fully charged, or, it completely discharges by binding some ions either from the air or from water. Let us first consider the former case. The charges on the de-wetted parts of the colloidal particles are then transferred from a region of high dielectric constant to

one of low dielectric constant. There is an energy penalty known as Born repulsion for transferring charges from a high to a low dielectric region [105]. The repulsion would in fact be high enough to make it virtually impossible for any colloid to break through the interface. This, however, would contradict all the experimental observations reporting stable 2D colloidal particles trapped at the air-water interface [12, 16, 106].

The alternative, namely a discharging of the de-wetted surface will cost free energy as well. A colloidal particle put in the bulk of an aqueous solution, would become spontaneously charged: its solvation energy U_{sol} is negative. If $p_{dewet}(h)$ is the fraction of the colloidal surface that is de-wetted, then $-U_{sol} \times p_{dewet}(h)$ could, in principle, be used to estimate the energy cost of discharging the particle. Being however a quantity that depends heavily on the microscopic details of the solvation process, U_{sol} would vary from colloid to colloid. Since we here wish to keep our considerations as general as possible, we have assumed the case of full discharging of the de-wetted surface (sec. 3.2.2), but completely ignored the energy contribution due to this discharging and concentrate instead on the only safe piece of information, that is, the energy change that goes along with the changes of the double-layer near the wetted surface as the particle goes through the interface. This assumption of de-wetting is also made in Ref. [12] in calculating E_s, as we discuss in the next section. We finally note that full discharging of the de-wetted part of the colloid implies that ∂G_c for $h < a$ in eq. (3.1) refers to only that part of the colloidal surface exposed to water.

3.3. Results and discussions

3.3.1. The electrostatic and surface energy barriers and traps

We have solved the PB-BVP of eq. (3.1) numerically for a charged colloidal particle near and at an air–aqueous electrolyte interface, at finite salt-ion concentrations characterized by the Debye screening constant κ. The solution enabled us to determine the grand potential and the effective interaction, eq. (3.2) between the charged particle and the air-water interface. Other relevant parameters that have gone into the problem are: the equilibrium temperature of the system characterized by the Bjerrum length λ_B, the colloid or particle radius a, the particle surface ion density σ and the interface–colloid separation distance h. We have then five input parameters; κ, λ_B, a, σ and h that govern the interaction potential. By scaling all lengths by a and the interaction potential as $\tilde{\lambda}_B\beta\Omega$ (see eq. (3.26)) we can reduce these parameters to only three independent input parameters: $\tilde{\kappa}$, $\tilde{h}$ and $\tilde{\sigma}$, where $\tilde{\lambda}_B = \lambda_B/a$, $\tilde{\kappa} = \kappa a$, $\tilde{h} = h/a$, and $\tilde{\sigma} = a\sigma\lambda_B$. The scaled form of the surface density is suggested by the first boundary condition in

eq. (3.1).

The reduced inverse screening length, $\tilde{\kappa}$ is varied from 0 to 3. The colloid position is varied from the bulk solution where $\tilde{h} \gg 1$ to the surface where $\tilde{h} < 1$. The magnitude of the reduced surface charge density $|\tilde{\sigma}|$ is changed from about 0.02 to 0.15 when we begin to encounter convergence problems in the numerical schemes for the BVP. A sphere of radius 1μm carrying $Z = 1000$ elementary charges corresponds to $\tilde{\sigma} \approx 0.057$ at room temperature. Because the fixed charges are assumed to be homogeneously distributed on the colloid, σ is constant and independent of h, but Z can vary with h when the particle pops out of water, see eq. (3.7). In the following presentation, it does not matter if σ or Z is given as positive or negative, they always appear as products in the energies. The choice and range of these parameters will enable us to explore the linear and to some extent nonlinear regimes of the potential ϕ_h.

Figure 3.4 shows the plot of the scaled grand potential $\tilde{\lambda}_B\beta\Omega(\tilde{h})$ as a function of the reduced interface–colloid separation distance, $\tilde{h}$ for various values of the reduced screening constant $\tilde{\kappa} = 0$, 0.5, 1.0 and 2.0 at fixed $\tilde{\sigma} = 0.08$. The $\tilde{\kappa} = 0$ curve is obtained from limiting potentials, eqs (3.6) and (3.9). All curves show a repulsive interface–colloid interaction at $\tilde{h} > 1$ and a well-resolved peak at $\tilde{h} = 1$. For $\tilde{h} < 1$, the particle begins to de-wet. The fraction of the colloid surface exposed to water decreases and accordingly the double-layer energy goes down, resulting in an obvious minimum, $\beta\Omega(h \leq -a) = 0$ when the particle is completely discharged. This minimum is not shown in the plots. We re-iterate that Fig. 3.4 shows just the double-layer interaction energy and that for $\tilde{h} < 1$ the energy contributions due to the discharging and the capillary forces have not yet been added. The figure reveals an electrostatic barrier to adsorption of the charged colloid to the interface from the bulk electrolyte. This barrier is lowered on increasing the salt content of the solution. Let us define the adsorption barrier height as

$$\tilde{\lambda}_B\beta V_{ad} = \tilde{\lambda}_B\beta[\Omega(\tilde{h} = 1) - \Omega(\infty)]\,. \tag{3.12}$$

There is also a double-layer barrier to pushing the particle from the interface back to the solution,

$$\tilde{\lambda}_B\beta V_{de} = \tilde{\lambda}_B\beta[\Omega(\tilde{h} = 1) - \Omega(-\infty)], \tag{3.13}$$

which we call double-layer desorption barrier ($\Omega(-\infty) = 0$). Figure 3.5 shows the variation of these quantities with $\tilde{\kappa}$, for $\tilde{\sigma} = 0.05$, 0.08 and 0.10. Both barrier heights decrease with increasing $\tilde{\kappa}$, i.e. increasing salt concentration. Note that both graphs of Fig. 3.5(a) and (b), are plotted to the same scale showing that for a given $\tilde{\sigma}$, the desorption barrier is far higher than the adsorption barrier.

We now turn to the other forces that the colloid experiences at the interface. Most important are the forces resulting from the surface tension which lead to a trap for the

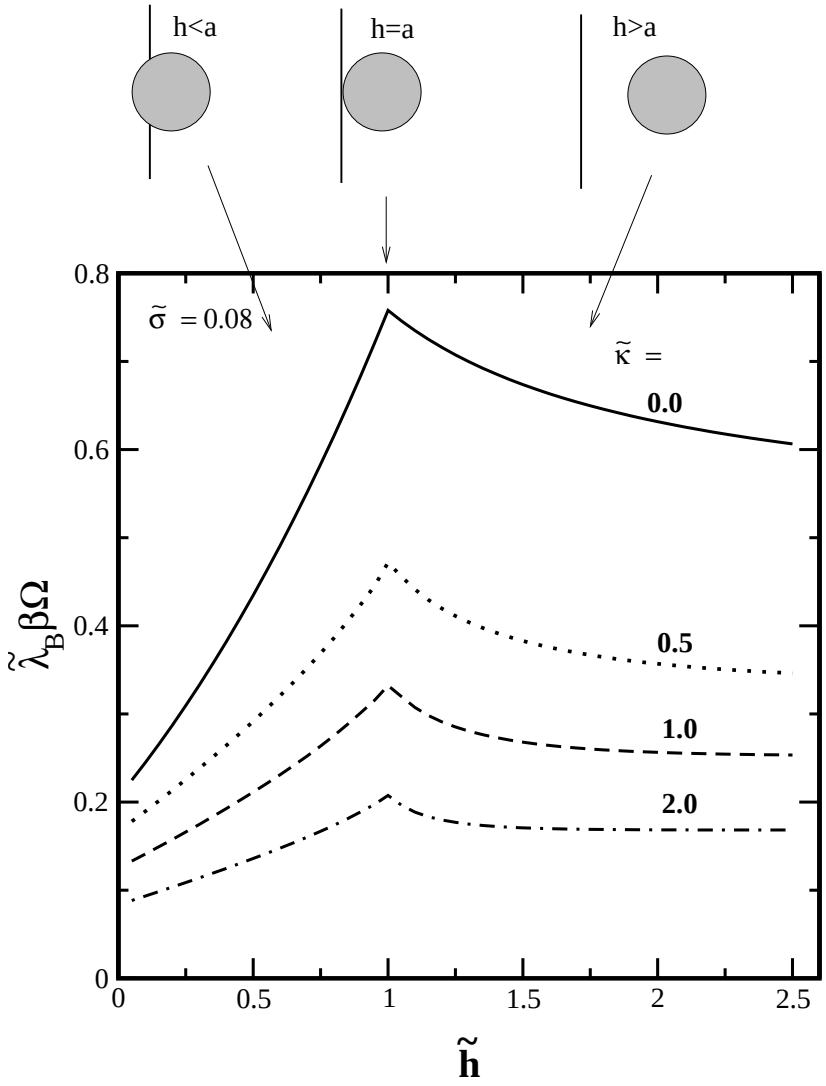

Figure 3.4: The grand potential given in the reduced form $\tilde{\lambda}_B\beta\Omega(\tilde{h})$ as a function of the interface–colloid separation distance, $\tilde{h}$ for various values of the screening constant. The reduced colloid surface charge density, $\tilde{\sigma}$ is fixed at 0.08. The $\tilde{\kappa} = 0$ curve is obtained from the limiting case, eqs (3.6) and (3.9), while the rest are through numerical solution of the non-linear PB equation. All lengths are given in the unit of the colloid radius, a, denoted by the tilde symbol. The sketch at the top of the plot show the relative position of the particle with respect to the interface in different regions of the graph.

colloidal particles at the air-water interface. It is instructive to compare the depth of this trap with that resulting from the double-layer forces just considered. Pieranski [12] has reported that polystyrene particles are trapped in a surface energy well with a minimum when a particle is immersed about two third of its diameter in suspension

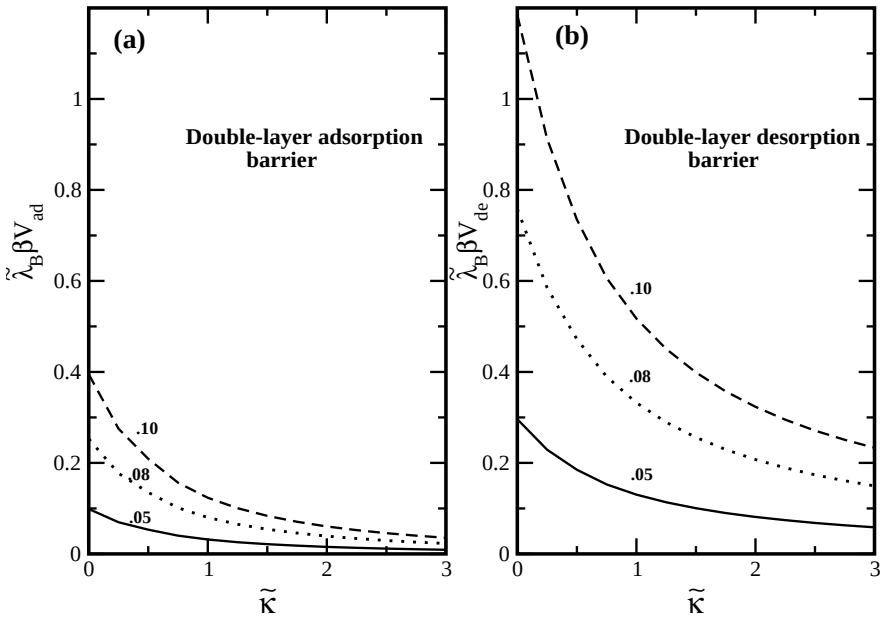

Figure 3.5: (a) The double-layer energy barrier height to the colloid adsorption to the air-water interface from the electrolyte, $\tilde{\lambda}_B\beta V_{ad}$ defined in eq. (3.12), as a function of the inverse screening length, $\tilde{\kappa}$, for various scaled surface charge densities, $\tilde{\sigma}$ (numbers labeling the curves). (b) The analogous barrier height to desorption back to the electrolyte from air, $\tilde{\lambda}_B\beta V_{de}$ defined in eq. (3.13), also as a function of $\tilde{\kappa}$.

($\tilde{h} \approx 1/6$). This surface energy is made up of three contributions [12]; the surface energy of the particle-air interface ($2\pi\gamma_{pa}a^2[1-\tilde{h}]$), the surface energy of the particle-water interface ($2\pi\gamma_{pw}a^2[1+\tilde{h}]$), and the negative surface energy of the missing air-water interface ($-\pi\gamma_{aw}a^2[1-\tilde{h}^2]$). The total energy can be expressed as,

$$\beta E_s(\tilde{h}) = \beta\pi a^2\gamma_{aw}\left(\tilde{h}^2 + 2(\bar{\gamma}_{pw}-\bar{\gamma}_{pa})\tilde{h} + 2(\bar{\gamma}_{pa}+\bar{\gamma}_{pw}) - 1\right), \qquad \tilde{h} \le 1 \quad (3.14)$$

where $\bar{\gamma}_{pa} = \gamma_{pa}/\gamma_{aw}$, $\bar{\gamma}_{pw} = \gamma_{pw}/\gamma_{aw}$; γ_{pw}, γ_{pa} and γ_{aw} are respectively the surface tensions of the particle-water, particle-air and air-water interfaces. Figure 3.6 shows the total surface energy, βE_s as a function of $\tilde{h}$. The energy well (the trap) is several orders of the thermal energy, β^{-1}. For the minimum energy, one obtains

$$\beta E_s(\tilde{h}_{min}) = \beta\pi a^2\gamma_{aw}\left(2(\bar{\gamma}_{pw}+\bar{\gamma}_{pa}) - (\bar{\gamma}_{pw}-\bar{\gamma}_{pa})^2 - 1\right) \quad (3.15)$$

with $\tilde{h}_{min} = (\bar{\gamma}_{pa}-\bar{\gamma}_{pw})$ found from minimizing eq. (3.14). The corresponding desorption barrier, βE_{de} for the surface energy is then given by,

$$\beta E_{de} = \beta E_s(\tilde{h}=1) - \beta E_s(\tilde{h}_{min})\,. \quad (3.16)$$

Dividing the surface energy desorption barrier by a^2 we obtain a quantity $\beta E_{de}/a^2$ that is constant for all particle sizes. On the other hand, the double-layer desorption barrier

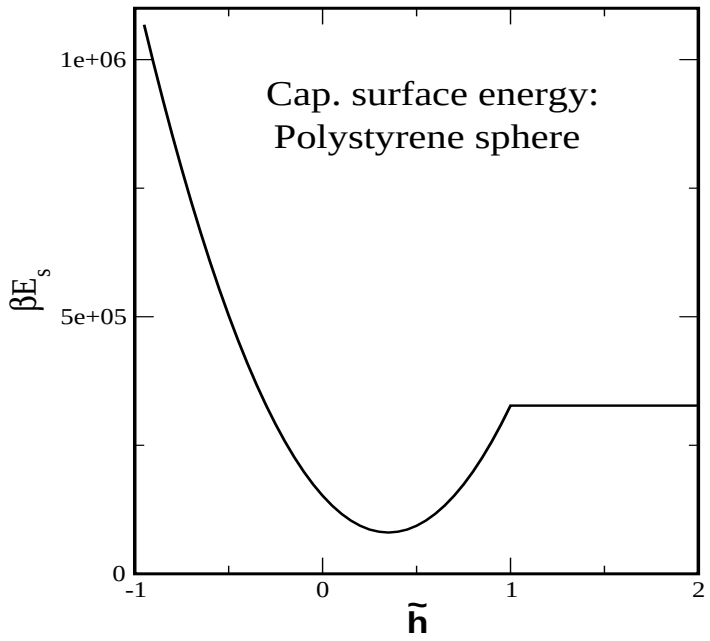

Figure 3.6: The capillary surface energy of a polystyrene colloidal sphere: $a = 100\text{nm}$, $\gamma_{pa} = 35\,\text{erg/cm}^2$, $\gamma_{pw} = 10\,\text{erg/cm}^2$ and $\gamma_{aw} = 72\,\text{erg/cm}^2$ [12].

reduced in the same manner, $\beta V_{de}/a^2$, still depends on the sphere radius as well as the surface charge density and the screening constant. To compare the two types of barrier for a polystyrene sphere, we have to resort back to the un-reduced parameters namely a, λ_B, κ and σ. Figure 3.7(a-c) show the variation of the double-layer desorption barrier per a^2 with the surface charge density $|e\sigma|$ for three particle radii $a = 50\text{nm}$, 100nm, and 200nm and for (a) $\kappa = 0.01\text{nm}^{-1}$ and (b) $\kappa = 0.005\text{nm}^{-1}$. λ_B is fixed at its room temperature value for water (0.715nm). The straight line in Fig. 3.7 is $\beta E_{de}/a^2$ ($\times 10^{-2}$). The values for γ_{pa}, γ_{pw} and γ_{aw} are taken from Ref. [12]. The figure shows that $\beta V_{de}/a^2$ increases with increasing a, increasing $|e\sigma|$ and decreasing κ. However, for the highest surface charge density and largest particle investigated here, the surface energy trap still leads the electrostatic trap by more than an order of magnitude. This implies that the stability of a colloidal particle at the air-water is dominated by the surface tension forces.

Figure 3.8 is meant as a summary of the preceeding considerations. Presented is a schematic drawing of the total interaction energy of a charged colloid near and at an air-water interface, i.e., the sum of the electrostatic contributions,$\beta\Omega_h$ and the energy due to the surface tension forces, βE_s. The force on a colloid, approaching the interface from bulk where $\tilde{h} \gg 1$, is repulsive, but for a particle of finite size the repulsive energy barrier has a finite height. This barrier height at $\tilde{h} = 1$ is the larger

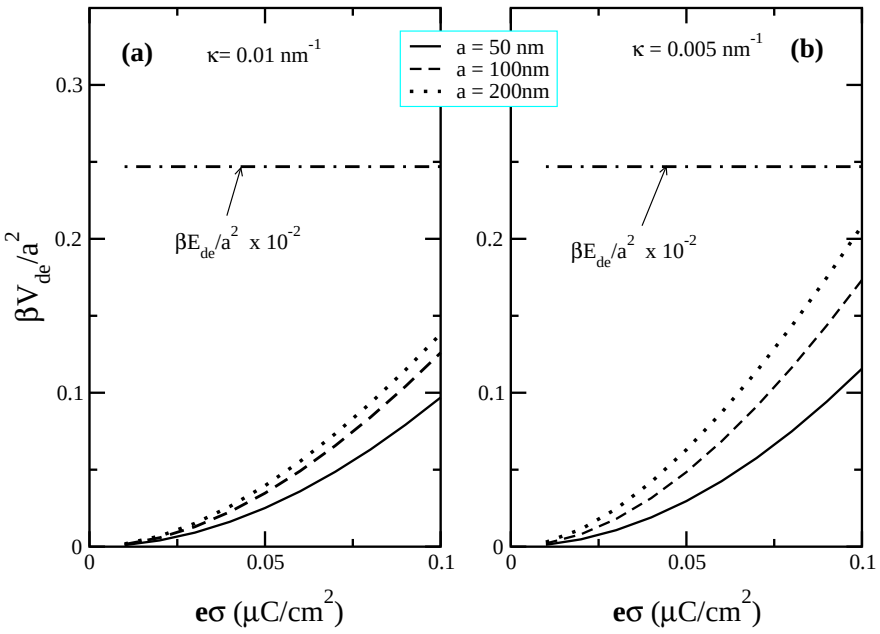

Figure 3.7: Comparing the double-layer barrier height to desorption with that of the surface energy, specifically for polystyrene spheres, and with unscaled parameters [a, λ_B, κ, $e\sigma$]. By dividing both double-layer barrier height, βV_{de} and the surface energy barrier height, βE_s by a^2, $\beta E_s/a^2$ remains constant while $\beta V_{de}/a^2$ varies with a,κ and σ. The axes labels are the same for the two plots.

the higher the colloidal surface charge or the lower the salt content of the electrolyte. When the colloidal particle breaks through the air-water interface, i.e., when $\tilde{h} < 1$, surface tension forces become important and hold the colloid in a trap that is orders of magnitude deeper than the height of the double-layer barrier.

It is an interesting observation that this picture of the interaction between a charged colloid and an air-water interface resembles our classical understanding of the effective colloid–colloid interaction in bulk (the DLVO theory [2]): in both cases, there is a repulsive and salt-dependent energy barrier at large distances that prevents particles collapsing into an attractive well at shorter distances that is orders of magnitudes larger (van-der-Waals attraction in DLVO theory, attractive surface tension force in our case). This, for instance, means that just in the same way as one can induce an initially stable colloidal suspension to aggregate by adding salt ('salting-out' effect), one should be able to cause colloids to pop up to the air-water interface by reducing the energy barrier through added salt.

It is necessary to point out again that the terms, *adsorption* and *desorption* used repeatedly in this study are only convenient terminologies to describe the behaviour of the particle in the vicinity of the interface. Ion adsorption or desorption is a complex

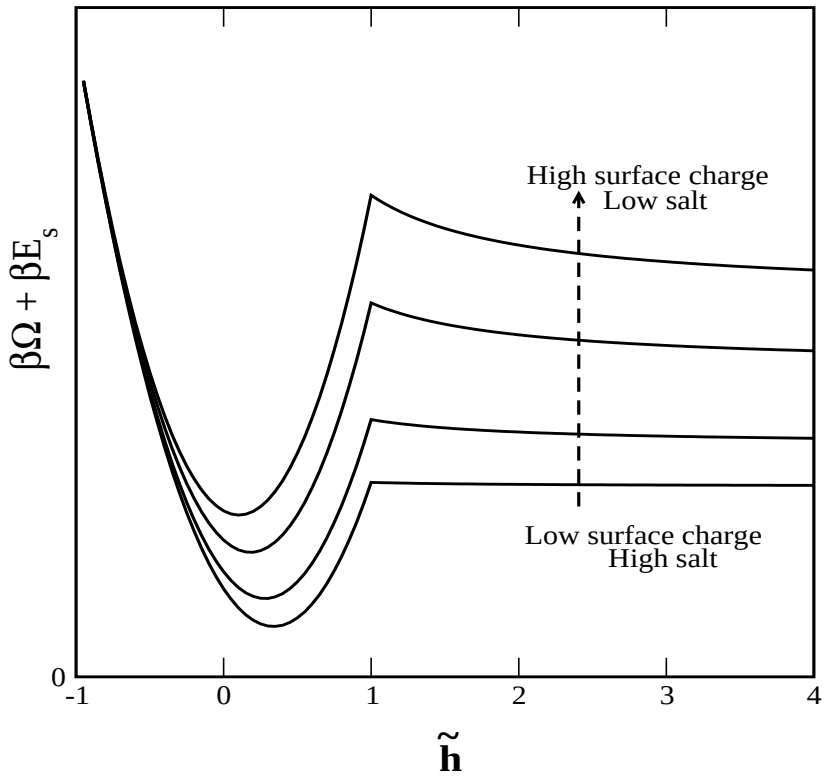

Figure 3.8: Schematic plot of the total interaction energy of a charged colloidal particle at the air-water interface with a repulsive double-layer energy barrier at large distances and an attractive well resulting from surface tension forces at shorter distances.

process which should include the explicit structure of the solvent (water) molecules. For similar reasons also, the potentials used in the analysis are regarded as *effective*, in that, contributions from solvent interactions (colloid-solvent, air-solvent) and contributions from lateral interactions (colloid–colloid) are not included.

3.3.2. Relevance to experiments

The forgoing results can be applied to explain qualitatively some experimental observations. (i) As mentioned earlier, Kesavamoorthy *et al.* [16] have described the observation of a layer of 2D triangular polystyrene crystals in a thin suspension film confined between glass and air. Below the air-water interface, the crystalline particles are separated by about two times the particle diameter. But on exposing the film to an intense laser light, some water is drained from the suspension and some particles suddenly pop out at the air-water interface, and subsequently collapse into a compact 2D structure. The sudden emergence of the particles at the interface can be explained

in the light of our results: By draining water from the film, the salt concentration is increased, increasing the screening constant κ, thereby reducing the electrostatic adsorption barrier height, $\tilde{\lambda}_B \beta V_{ad}$. The particles can then overcome the barrier and are subsequently trapped in both electrostatic and surface capillary energies, but most dominantly in the latter, as we have shown in Fig. 3.7.

(ii) The adsorption rates of some charged proteins at interfaces have been observed to increase with increasing ionic strength of the solvent. MacRitchie and Alexander [107] quite long ago have studied experimentally the rate of adsorption of the charged globular proteins, bovine serum albumin and lysozyme at the air-water interface. Varying the electrostatic potential by addition of NaCl, the rate of adsorption was found to increase as the potential was decreased. This is in agreement with our result in which the interface–colloid interaction potential is decreased with increased screening, resulting in lowering of the adsorption barrier. Furthermore, the much talked about non-reversibility of proteins on adsorption at air-water interface which has been attributed largely to denaturing once at the interface [98], may well also be due to the trapping of the protein at the interface.

(iii) A recent Atomic force microscope (AFM) experiment [108] involving a direct measurement of the force of interaction between an air bubble attached to the base of the AFM piezo stage and a single polystyrene sphere attached to the AFM cantilever all in an aqueous electrolyte, shows some barrier (suspected to be of electrostatic origin) to the particle approach to the air-water (bubble-water) interface. However, direct comparison of data from AFM experiments with theoretical results such as ours is not quite straight forward for the following reason: The conversion of the direct measurable AFM stage position and the cantilever deflection, to the more relevant interface–colloid separation is problematic due to the deformability of the bubble interface. That is, the position of the interface shifts as the particle approaches the interface. A good deal about the AFM experiments for particle – air-water interface interaction can be found in Refs. [109, 104] and in Appendix B (sec. 3.5.2 of the present chapter) where we have also given a simple procedure for coming to the interface–colloid distance from the AFM observables. The idea is to provide a guide to the AFM experimentalist to use his system properties to come to the theoretically accessible interface–colloid separation distances from the piezo positions.

3.4. Summary and conclusions

This chapter presents essentially a numerical study of the interaction of a single charged colloidal particle of radius a with an air-water interface, where special emphasis has

been put on the electrostatic aspect of this problem. Based on the PB equation, the effective electrostatic double-layer interaction was calculated for all possible interface–colloid separation distances h, including the cases, when the particle touches and breaks through the air-water interface – situations not considered in the preceeding chapter. The PB boundary value problems could be solved numerically using geometry-adapted coordinate systems for the three situations $h > a$, $h = a$ and $h < a$. For $h > a$ the colloid experiences a repulsive double-layer force which becomes attractive for $h < a$. The resulting double-layer energy barrier has its maximum value at $h = a$. We studied its dependence on the colloidal surface charge density and the salt concentration of the electrolyte, and compared it with the depth of the surface tension trap, located directly at the air-water interface. For the system experimentally studied in Ref. [12], the energy contributions due to surface tension forces are some orders of magnitude larger than those resulting from electrostatic forces. The electrostatic aspects of the problem are therefore mainly important in the distance regime where the colloid has not yet broken through the interface, i.e., at $h \geq a$. In the distance regime $h < a$, a thorough calculation of the interaction potential is still awaited; it must take into account a) the detailed discharging process of the de-wetted part of the colloidal surface, and b) the capillary forces with a realistic description of the meniscus.

An interesting analogy that we have mentioned in this work, is that between the DLVO problem of two colloids in bulk and our problem of a colloid near the air-water interface. From an electrostatic viewpoint, this analogy is obvious from the image-charge concept: A charged colloidal particle a distance $z = h$ from the air-water interface behaves as if there were another colloidal particle of the same charge at $z = -h$ (apart from a factor $1/2$ in the interaction potential). The resulting interaction is repulsive. But the analogy to the classical DLVO picture extends a little further: in both cases, electrostatic double-layer repulsion at large distances contrasts with a much stronger attraction at smaller distances. It is due to dispersion forces in the DLVO case, and caused by surface tension forces in our case. Important is that the repulsive double-layer barrier, preventing the particle from being pulled into the attractive well, is salt-dependent, and can thus be easily manipulated experimentally. In the same way as a colloidal suspension can be caused to become unstable, we can induce a colloidal particle to pop up to the air-water interface – by adding salt. Experiments in which this interesting effect has actually been observed are mentioned and discussed in the text.

3.5. Appendix

3.5.1. A: Solution of the Poisson-Boltzmann equation and the grand potential in the various coordinate systems

In our numerical scheme, the PB equation and the grand potential for the problem have been written and solved in different coordinate systems. They include BSC, TOC and TSC systems. Each coordinate system is suitable for a particular interface–colloid configuration (Fig. 3.1). They enable the complex system boundaries to be transformed into 2D rectangular forms. The BSC system is suitable when the particle center to interface separation distance is greater than the particle radius and has been described elsewhere in chapter 2. The TSC and TOC systems for touching and penetrated configurations respectively, are described here in a similar manner.

Under constant charge boundary condition, the BVP, eq. (3.1) can be written as:

$$\begin{array}{ll} \nabla^2\phi = \tilde{\kappa}^2 \sinh\phi & \mathbf{r} \in G \\ \mathbf{n}_c \nabla\phi = 4\pi\tilde{\sigma} & \mathbf{r} \in \partial G_c \\ \mathbf{n}_w \nabla\phi = 0 & \mathbf{r} \in \partial G_w \\ \phi = 0 & \mathbf{r} \to \infty \end{array} \tag{3.17}$$

where all lengths including the Laplacian have been scaled by the particle radius a; $\tilde{\kappa} = \kappa a$, $\tilde{\sigma} = a\sigma\lambda_B$. Any reduced length is indicated by the tilde ($\sim$) symbol.

Toroidal coordinates

The TOC system $(\alpha, \omega, \varphi)$ [73] is related to our (s, z) coordinates, where again for the radial $s(x, y)$; $x = (b \sinh\alpha \cos\varphi)/(\cosh\alpha - \cos\omega)$ and
$y = (b \sinh\alpha \sin\varphi)/(\cosh\alpha - \cos\omega)$, so that

$$\begin{aligned} s &= \frac{b \sinh\alpha}{\cosh\alpha - \cos\omega} \\ z &= \frac{b \sin\omega}{\cosh\alpha - \cos\omega}. \end{aligned} \tag{3.18}$$

The parameter, b is as defined in Fig. 3.9.

The coordinate surfaces include pairs of intersecting spherical bowls ($\omega = \pm\omega$). To make the system adaptable to our problem, one pair of the spherical bowls is assumed to correspond to the colloid and its image (Fig. 3.9(a)).

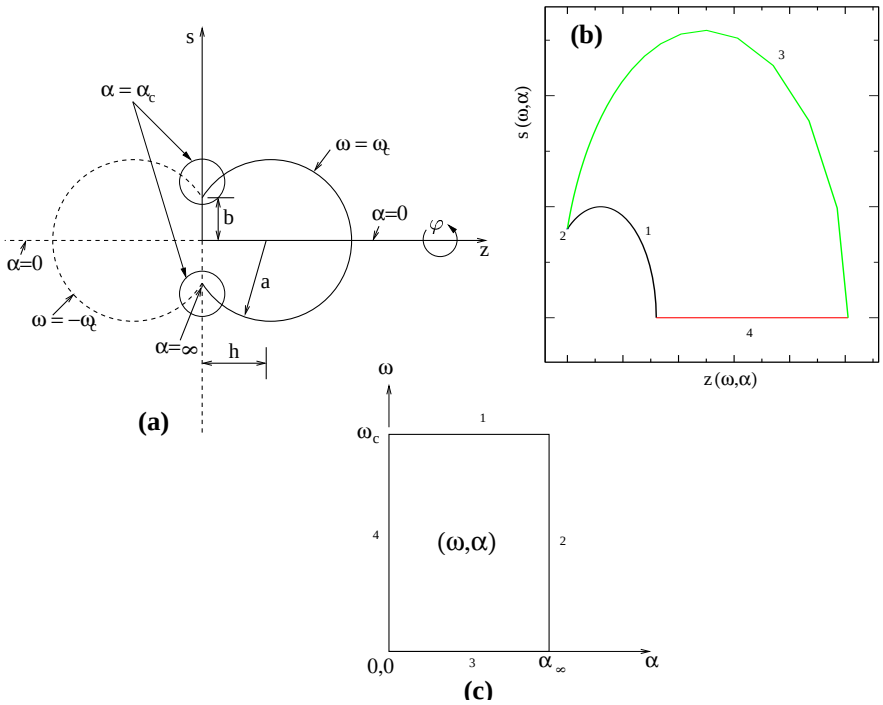

Figure 3.9: The toroidal coordinate system: (a) The coordinate surfaces are toroids of constant α (α_c), spherical bowls of constant ω ($\pm\omega_c$), and half planes about the z-axis (φ). Using eq. 3.18 the boundaries in (b) are mapped into the rectangle (c).

The equation of the coordinate surface of interest, the spherical bowls is given by [73],

$$s^2 + (z - b\cot\omega)^2 = \frac{b^2}{\sin^2\omega}\,. \tag{3.19}$$

The particle of radius a, centered at h is a surface of constant ω, ω_c with the following important relations:

$$\begin{aligned} a &= b/\sin\omega_c \\ h &= b\cot\omega_c \\ h/a &= \cos\omega_c \end{aligned}\quad . \tag{3.20}$$

We proceed to express eq. (3.17) in the (α,ω) coordinates, starting with boundary condition on the four sides of the rectangle (Fig. 3.9(c)):

$$\begin{aligned} \partial_\alpha\phi(\alpha_\infty,\omega) &= 0 \\ \partial_\omega\phi(\alpha,0) &= 0 \\ \partial_\alpha\phi(0,\omega) &= 0 \\ \partial_\omega\phi(\alpha,\omega_c) &= \left(\frac{b}{\cosh\alpha - \cos\pi}\right)(-4\pi\tilde{\sigma})\,. \end{aligned} \tag{3.21}$$

The Laplacian in the PB equation transforms as:

$$\begin{aligned}\nabla^2\phi &= \frac{\delta^3}{b^2\sinh\alpha}\left\{\frac{\partial}{\partial\alpha}\left(\frac{\sinh\alpha}{\delta}\frac{\partial\phi}{\partial\alpha}\right)+\sinh\alpha\frac{\partial}{\partial\omega}\left(\frac{1}{\delta}\frac{\partial\phi}{\partial\omega}\right)\right\}\\ &= \frac{\delta^3}{b^2}\left\{\frac{1}{\delta}\frac{\partial^2\phi}{\partial\alpha^2}+\frac{1}{\delta}\frac{\partial^2\phi}{\partial\omega^2}+\frac{(1-\cosh\alpha\cos\omega)}{\delta^2\sinh\alpha}\frac{\partial\phi}{\partial\alpha}-\frac{\sin\omega}{\delta^2}\frac{\partial\phi}{\partial\omega}\right\}\end{aligned} \tag{3.22}$$

where $\delta=\cosh\alpha-\cos\omega$. Equation (3.22) along with the boundary conditions eq. (3.21) are then applied in the Newton-Raphson iteration scheme in the form:

$$\frac{1}{\tilde{\kappa}}\nabla^2\phi_{n+1}-(\cosh\phi_n)\phi_{n+1}=\sinh\phi_n-(\cosh\phi_n)\phi_n, \tag{3.23}$$

where the index n is an iteration step.

The surface and volume integrals appearing in the grand potential (see eqs (2.11) and (2.11a) can be expressed in the present coordinates thus;

$$\begin{aligned}\int d\tilde{V} &\equiv \int\int\int \frac{\tilde{b}^3\sinh\alpha}{(\cosh\alpha-\cos\omega)^3}d\alpha d\omega d\varphi\\ &= 2\pi\int\int\frac{\tilde{b}^3\sinh\alpha}{(\cosh\alpha-\cos\omega)^3}d\alpha d\omega\end{aligned} \tag{3.24}$$

and

$$\int d\tilde{S}\equiv 2\pi\int\frac{\tilde{b}^2\sinh\alpha}{(\cosh\alpha-\cos\omega)^2}d\alpha. \tag{3.25}$$

The grand potential, following eq. (2.11) can then be written as

$$\begin{aligned}\tilde{\lambda}_B\beta\Omega(h) &= -\pi\tilde{\sigma}\int\phi_h\frac{\tilde{b}^2\sinh\alpha}{(\cosh\alpha-\cos\omega_c)^2}d\alpha\\ &\quad+\frac{\tilde{\kappa}^2}{4}\int d\alpha\int d\omega\,[\phi_h\sinh\phi_h-2(\cosh\phi_h-1)]\,\frac{\tilde{b}^3\sinh\alpha}{(\cosh\alpha-\cos\omega)^3}\end{aligned} \tag{3.26}$$

with $\tilde{b}=b/a$.

Tangent-sphere coordinates

The tangent-sphere coordinate system (μ,ν,φ) is similar to the toroidal coordinate system with the two fused spherical bowls now two tangent spheres. The coordinate surfaces are: the half-planes of constant φ, toroids of constant μ, and pairs of tangent spheres of constant ν $(\pm\nu_c)$, which are convenient for describing our system if the

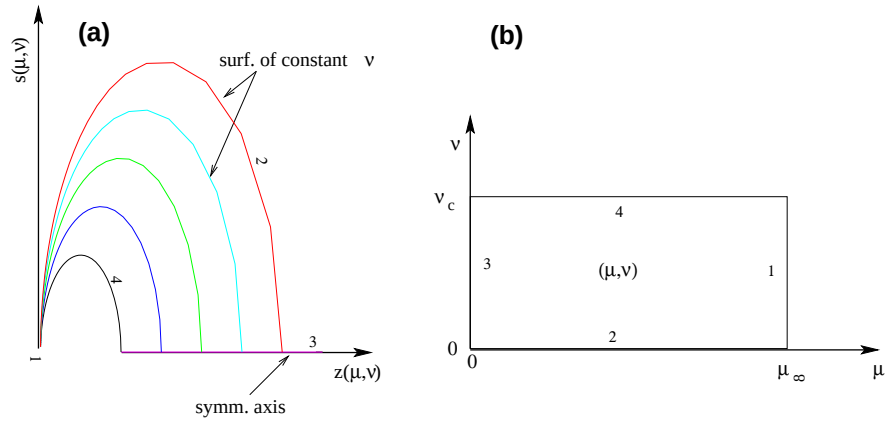

Figure 3.10: The tangent-sphere coordinate system: The surfaces numbered 1 ... 4 in the (s, z)-coordinates (a) forms the rectangular boundaries in (b) using eq. (3.27).

particle just touches the interface ($h = a$). Again, the second sphere is assumed to be the particle image. The configuration has cylindrical symmetry and relates with the coordinates (s, z) thus (see Fig.3.10):

$$\begin{aligned} s &= \frac{\mu}{\mu^2 + \nu^2} \\ z &= \frac{\nu}{\mu^2 + \nu^2} \end{aligned} \tag{3.27}$$

The surfaces of constant μ are toroids without center opening. The equation of the tangent sphere can be written as,

$$s^2 + \left(z - \frac{1}{2\nu}\right)^2 = \frac{1}{4\nu^2}. \tag{3.28}$$

That gives as in eq. (3.20) the following relations,

$$\begin{aligned} a &= 1/2\nu_c \\ h &= 1/2\nu_c \\ h/a &= 1\,. \end{aligned} \tag{3.29}$$

The BVP can be summarized in the following equations:

$$\begin{aligned} \gamma^2\frac{\partial^2\phi}{\partial\mu^2} + \gamma^2\frac{\partial^2\phi}{\partial\nu^2} + \gamma\frac{(\nu^2-\mu^2)}{\mu}\frac{\partial\phi}{\partial\mu} - 2\gamma\nu\frac{\partial\phi}{\partial\nu} &= \sinh\phi; \\ \partial_\mu\phi(\mu_\infty,\nu) &= 0 \\ \partial_\nu\phi(\mu,0) &= 0 \\ \partial_\mu\phi(0,\nu) &= 0 \\ \partial_\nu\phi(\mu,\nu_c) &= \left(\frac{1}{\mu^2+\nu_c^2}\right)(-4\pi\tilde{\sigma}), \end{aligned} \tag{3.30}$$

where $\gamma = \mu^2 + \nu^2$. The grand potential in this coordinate system can be derived as

$$\begin{aligned} \tilde{\lambda}_B \beta\Omega(h) &= -\pi\tilde{\sigma} \int \phi_h \frac{\mu}{(\mu^2 - \nu_c)^2} d\mu \\ &\quad + \frac{\tilde{\kappa}^2}{4} \int d\mu \int d\nu \left[\phi_h \sinh\phi_h - 2(\cosh\phi_h - 1)\right] \frac{\mu}{(\mu^2 - \nu^2)^3} \end{aligned} \tag{3.31}$$

Bispherical coordinates (η, θ, φ)

Having described the bispherical coordinate scheme fully in the previous chapter, it suffices here to write down the grand potential in this coordinate system as in eqs (3.26) and (3.31):

$$\begin{aligned} \tilde{\lambda}_B \beta\Omega(h) &= -\pi\tilde{\sigma} \int \phi_h \frac{\tilde{b}^2 \sin\theta}{(\cosh\eta - \cos\theta)^2} d\theta \\ &\quad + \frac{\tilde{\kappa}^2}{4} \int d\eta \int d\theta \left[\phi_h \sinh\phi_h - 2(\cosh\phi_n - 1)\right] \frac{\tilde{b}^3 \sin\theta}{(\cosh\eta - \cos\theta)^3}, \end{aligned} \tag{3.32}$$

where all symbols have their definitions as given in sec. 2.2.1,chapter 2.

3.5.2. B: The Atomic force microscope

The interaction of solid colloidal particles with fluid interfaces is often measured by the Atomic force microscope (AFM). Ducker *et al* [104] measured forces across water between a silica probe particle attached to the AFM cantilever and an air bubble sitting on the piezo-driven stage. Similar experiments have been reported by other workers [108, 110-112]. Chan *et al* [109] basing their study on AFM experiments have recently probed the effect of disjoining pressure on particle-fluid interface interaction in an analytic manner to describe the total force exerted on the probe particle as a function of the distance of the piezo stage. They also displayed numerical results based on the solution of the PB equation using the Derjaguin method [2], a reasonable method in the limit where the interface–colloid separation is much smaller than the particle radius, as for the AFM probe particle ($a \sim 1$ — 3μm).

The difficulty in analyzing AFM results lies mainly in converting the particle-piezo stage distance, l, and the cantilever deflection d (see Fig. 3.11(a)) to the particle–interface minimum separation, D_0 (in our study $D_0 = h - a$), a major parameter in theoretical schemes. The difficulty arises because the air-water interface (or bubble interface) is no longer planar as the particle approaches the interface but is deformed according to the elasticity of the interface. Sticking to the labels used by Chan *et al* [109] for the AFM setup, we outline below, a rather simple recipe for the conversion.

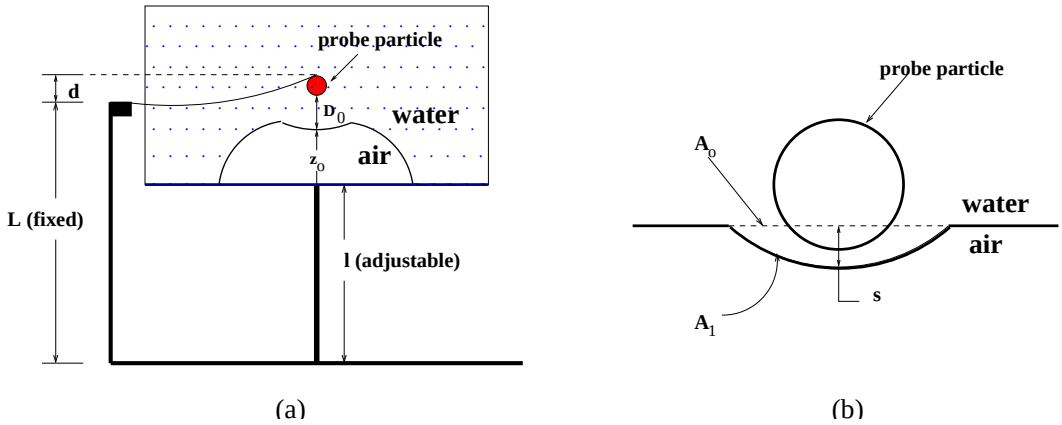

Figure 3.11: (a) Geometry of the AFM measurement. (b) Estimating the bubble "spring constant", k_b.

From Fig. 3.11(a) we observe that D_0 can be expressed as;

$$D_0 = d + l_0 - l \tag{3.33}$$

where $l_0 = L - 2a - z_0$. The direct measurable quantities are; L which is fixed as shown, l the adjustable piezo stage, a the particle radius and d, the cantilever deflection measured by light reflection technique. l_0 and hence z_0 the deformed height of the bubble can be estimated from the elastic properties of the interface. If the interface is assumed linearly elastic, then we may write the force F, exerted by the probe on the interface as;

$$F = k_b(z_1 - z_0) \tag{3.34}$$

where z_1 is the undeformed height of the bubble (also measurable [104]) and k_b is the effective "spring constant" of the interface. We also have that,

$$F = k_c d, \tag{3.35}$$

with k_c the spring constant of the AFM cantilever. Hence from eq. (3.34) and (3.35), we find that

$$z_0 = z_1 - \frac{k_c}{k_b} d \tag{3.36}$$

or

$$l_0 = l_1 + \frac{k_c}{k_b} d, \tag{3.37}$$

where $l_1 = L - 2a - z_1$.

What is now left is to estimate k_b. Consider the flat bubble surface deformed by the force on the particle, as shown in Fig. 3.11(b). Because the bubble is too large

compared to the particle, the particle sees a flat environment. The elastic free energy of changing the flat cross sectional area, A_0 to the depressed area A_1 can be written as;

$$E(s) = \gamma_b(A_1 - A_0) \tag{3.38}$$

where s $(= z_1 - z_0)$ is the height of the surface depression (Fig. 3.11(b)) and γ_b is the bubble-water surface tension ($\gamma_b = 0.072\text{N/m}$). It is hence straightforward to show that

$$A_1 - A_0 = \pi s^2, \tag{3.39}$$

so that

$$E(s) = \pi\gamma_b s^2. \tag{3.40}$$

The corresponding force, $F(s)$ is then,

$$\begin{aligned} F(s) &= 2\pi\gamma_b s \\ &= 2\pi\gamma_b(z_1 - z_0). \end{aligned} \tag{3.41}$$

Comparing eq. (3.41) and (3.34), we have,

$$k_b = 2\pi\gamma_b, \tag{3.42}$$

which remarkedly turns out to be simple and solely dependent on the elasticity of the bubble-water interface characterized by the surface tension γ_b. Putting all together, eq. (3.33) now becomes

$$D_0 = (h - a) = (1 + \frac{k_c}{2\pi\gamma_b})d + l_1 - l. \tag{3.43}$$

This relation would make it possible to compare the F over l force curves measured in the AFM experiment (with $F = k_c d$) with theoretical calculations like e.g., the forces derivable from the interaction potentials obtained in the present study.

4

Interaction and phase behaviour of 2D systems of macroions at an air-water interface

4.1. Introduction

Having established in chapter 3 that a charged colloidal particle (macroion) can be trapped at the air-water interface in a deep capillary surface energy well [12], we study here in the present chapter, a 2D system of such macroions trapped at the interface between air and an aqueous electrolyte solution (referred here again as the air-water interface). Such system has been studied theoretically by others before [92, 113]. Important in our context is the work of Terao *et al* [92] who have performed Monte-Carlo (MC) simulations in 2D, of colloidal particles at the air-water interface at low salt concentration and low surface particle densities. The major result of their work includes finding a two stage melting transition of 2D crystals with the hexatic phase intermediate between the solid and the fluid phases. However, this study may be inconclusive since some of the motivating experiments — including notably the observation of 2D colloidal crystals and clusters [12, 16, 34], and, more importantly, crystallization of proteins at the air-water interface [37, 114] — involve an additional dielectric interface apart from the air-water interface, which has not been considered in [92, 113].

The present chapter therefore focuses on the role of this additional surface. We address the question of how the phase behaviour of the 2D colloidal system at the air-water interface is affected when the system is further confined by some substrate having

different dielectric characteristics (dielectric constant ϵ_3) from that of the suspension. The additional interface is expected to induce effects due to confinement and image-charges, depending on the distance L between the air-water and the substrate-water interfaces. This in turn is expected to have consequences on the interaction and thus on the phase behaviour of the system. After first deriving a pair interaction potential that accounts for the additional dielectric substrate (sec. 4.2), we follow Ref. [92] and systematically probe in sec. 4.3 and 4.4, also via MC simulation, the effect of the additional substrate-water interface on the phase behaviour of the 2D colloidal system. The two key parameters of the our system are the dielectric constant ϵ_3 of the additional substrate and the distance L. In order to keep the number of variables as small as possible, we consider only three representative substrates, $\epsilon_3 = \infty$ (metal), $\epsilon_3 = 78.3$ (water) and $\epsilon_3 = 1$ (air), marking the extremes and thus spanning the possible range of changes expected due to the additional substrate.

Two classes of macroionic particles are investigated, namely, large and highly charged colloidal particles, such as latex particles and relatively smaller globular protein particles carrying only few charges. We warn again that modeling proteins as spherical colloids can certainly be a rather crude approximation, 'crude' in the sense that protein particles can be highly anisotropic. However, regarding e.g. the more general non-specific physico-chemical properties of the 2D systems of charged interfacial particles, the present study of 2D colloid arrays may offer certain insight, particularly into the question of whether or not the growing of 2D arrays of proteins can be influenced by an additional dielectric substrate. Indeed, protein particles in solutions have been reported to form various forms of arrays including crystals at the air-water interface with various types of supporting substrate [37, 114, 115]. The need to obtain 2D arrays of proteins arises due to the fact that large 3D single crystals are often difficult to obtain, and the subsequent structural analysis by x-ray techniques can be rather time-consuming. On the other hand, 2D arrays of proteins if obtained lend themselves to rapid analysis by electron microscopy techniques and requires only small amounts of sample material [116]. Another application of 2D protein arrays, showing the potential usefulness of these systems, is suggested in Ref. [117] where ferritin (a globular protein with iron core) arrays could be used as the component of an ultimate memory device.

It is obvious that the formation, quality, forms and stability of 2D arrays depend largely on the strength of the attractive and repulsive interparticle forces at play. The interaction between particles at air-water interface are governed by (i) lateral capillary forces [118-120], (ii) electrostatic forces [12, 13, 92, 121] for charged colloids, (iii) magnetic forces [122-124] for the case of magnetic particles, and (iv) the short-ranged van-der-Waals forces. We here concentrate exclusively on the second type of interparticle force. While the last two types of forces can be safely ignored in the

system under investigation, a word of caution is in order regarding the capillary forces.

The main cause of the lateral capillary forces is the deformation of the liquid surface, which is supposed to be flat in the absence of the particles. The larger the interfacial deformation created by the particle, the stronger the capillary interaction between them. Hence the origin of this force is essentially the particle weight. However, capillary forces can persist even for particles of vanishing size and weight, when particles, instead of being freely floating, are partially immersed (immersion capillary forces) in a thin liquid layer on a substrate [125]. The deformation of the liquid surface in this case is related to the wetting properties of the particle surface, i.e to the position of contact line and magnitude of contact angle, rather than to gravity. Hidalgo-Álvarez and coworkers [126] have, however, shown that for the sizes of latex particles commonly investigated in the literature (particle diameters $< 1\mu$m), lateral capillary forces can be neglected. And in the ignorance of any specific wetting properties we can also ignore the immersion capillary forces in this study. Wetting/de-wetting effects are also essential in reducing the total charge on the interfacial particle relative to its value in the bulk due to partial exposition to the low polarizability half space – the air (chapter 3).

We finally remark that one of the potentials investigated in [113] for structural analysis include that derived by Chang and Hone [127] for particles sandwiched between two dielectric walls (sandwich geometry). Similar studies on structures corresponding to systems in sandwich geometry abound, see e.g. [128, 129]. The sandwich system though very similar, is subtly different from the scenario of particles trapped at an interface, e.g. air-water (where additional dipole-dipole interaction plays a role) in the vicinity of a second substrate, e.g. glass, metal, e.t.c.

4.2. Formalism

We here wish to calculate the electrostatic interaction potential of two point-macroions a distance r apart, each carrying a total number, Z elementary charges e, trapped at the interface formed by a gaseous phase (air) of dielectric constant ϵ_1 (region 1) and an electrolyte solution of dielectric constant ϵ_2 (region 2), see Fig. 4.1(a). Next we introduce a substrate of dielectric constant ϵ_3 (region 3) such that the electrolyte could become a quasi-2D film of thickness L (Fig. 4.1(b)). Hence we have three distinct regions resulting in two interfaces; the ϵ_1/ϵ_2 interface we shall identify as the air-water or air-solution interface, and the ϵ_2/ϵ_3 interface we refer to as the substrate-water or substrate-solution interface, where substrate can be any material (including also air and water) without any mobile or static charges. Only the electrolyte (region 2) is allowed

to contain mobile microions, characterized by the inverse Debye screening length κ.

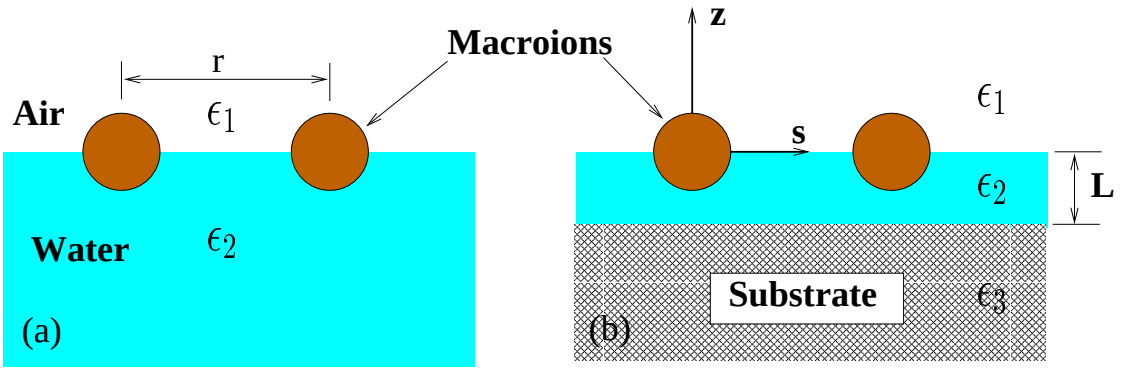

Figure 4.1: Two macroions, a distance r apart, trapped at an air-water interface; (a) no substrate and (b) with a dielectric substrate of separation distance L from the air-water interface.

4.2.1. Debye-Hückel theory in slab geometry

Within the DH theory, the electrostatic potential φ at a position $\mathbf{r}$ due to a point-source Ze located at $\mathbf{r}'$ in the vicinity of two parallel semi-infinite slabs separated by a distance L along the vertical axis, z can be given by the differential equation,

$$\nabla^2\varphi(\mathbf{r},\mathbf{r}') = \kappa_i^2\varphi(\mathbf{r},\mathbf{r}') - \frac{4\pi Ze}{\epsilon_i}\delta(\mathbf{r}-\mathbf{r}'), \tag{4.1}$$

where κ_i $(i = 1, 2, 3)$ is the inverse screening length in region i of dielectric constant ϵ_i. Equation (4.1) can be re-expressed for convenience as;

$$\frac{k_BT\epsilon_i}{4\pi Ze^2}[\nabla^2 - \kappa_i^2]\phi(\mathbf{r},\mathbf{r}') = -\delta(\mathbf{r}-\mathbf{r}'), \tag{4.2}$$

where $\phi = e\psi/k_BT$ is the normalized electrostatic potential. Expressing eq. (4.2) in cylindrical coordinates; $\mathbf{r} = \mathbf{r}(s, z)$, where $s = \sqrt{x^2+y^2}$, we have

$$\frac{k_BT\epsilon_i}{4\pi Ze^2}\left[\frac{\partial^2}{\partial s^2} + \frac{\partial^2}{\partial z^2} - \kappa_i^2\right]\phi(s,s',z,z') = -\delta(s-s')\delta(z-z'). \tag{4.3}$$

We take the Fourier transform (FT) of eq. (4.3) with respect to the coordinate variable, s to obtain;

$$\begin{aligned}\frac{k_BT\epsilon_i}{4\pi Ze^2}\left[-\mathrm{k}^2 + \frac{\partial^2}{\partial z^2} - \kappa_i^2\right]\tilde{\phi}(\mathrm{k},z,z') &= -\delta(z-z')\mathrm{e}^{-i\mathrm{k}\mathbf{s}'},\\ \frac{k_BT\epsilon_i}{4\pi Ze^2}\left[\frac{\partial^2}{\partial z^2} - (\mathrm{k}^2+\kappa_i^2)\right]\tilde{\phi}(\mathrm{k},z,z') &= -\delta(z-z'),\end{aligned} \tag{4.4}$$

where we have put $\mathbf{s}' = 0$ without loss of generality.

We can write eq. (4.4) for our earlier described model system where we assume that regions 1 and 3 contain no charges, i.e. $\kappa_1 = \kappa_3 = 0$, region 2 contains water with some finite amount of mobile microions of screening constant $\kappa_2 \equiv \kappa$. In the three regions we now have;

$$\begin{aligned}
\frac{k_B T \epsilon_1}{4\pi Z e^2}\left[\frac{\partial^2}{\partial z^2} - \mathrm{k}^2\right]\tilde{\phi}(\mathrm{k}, z, z') &= -\delta(z - z'); \qquad z < 0 \\
\frac{k_B T \epsilon_2}{4\pi Z e^2}\left[\frac{\partial^2}{\partial z^2} - (\mathrm{k}^2 + \kappa^2)\right]\tilde{\phi}(\mathrm{k}, z, z') &= -\delta(z - z'); \quad 0 < z < L \\
\frac{k_B T \epsilon_3}{4\pi Z e^2}\left[\frac{\partial^2}{\partial z^2} - \mathrm{k}^2\right]\tilde{\phi}(\mathrm{k}, z, z') &= -\delta(z - z'); \qquad z > L
\end{aligned} \tag{4.5}$$

The solution to the set of eqs (4.5) can conveniently be expressed in terms of the eigenfunctions in the three regions;

$$\begin{aligned}
\Psi_i^+(z) &= \mathrm{e}^{pz}, \\
\Psi_i^-(z) &= \mathrm{e}^{-pz}; \quad i = 1, 2, 3
\end{aligned} \tag{4.6}$$

where $p = \sqrt{\kappa^2 + \mathrm{k}^2}$.

In writing the solutions, we note that the potentials have to vanish at infinity, i.e. $\phi(\infty) \to 0$, in addition to the boundary conditions where we demand continuity of the potentials and their normal derivatives across the regions.

There are different possible solutions $\tilde{\phi}_i^n$, $i, n = 1, 2, 3$ to eq. (4.5) for various locations (z') of the point-source evaluated at various positions along z in the three regions. For example, $\tilde{\phi}_2^3$ is the potential at any point in region 2 (the ϵ_2-medium) due to the test ion in region 3. We shall however, narrow ourselves to $\tilde{\phi}_2^2(\mathrm{k}, z, z')$ where the point-source is located and observed in the solution (region 2). We will later take limit of $z' \to 0$ when the point-charge is adsorbed at the boundary between regions 1 and 2. Hence with $\tilde{\phi}_2^2(\mathrm{k}, z, z') \equiv \tilde{\phi}(\mathrm{k}, z, z')$ we have;

$$\begin{aligned}
\tilde{\phi}(\mathrm{k}, z, z') &= \left[A\Psi_2^+(z) + B\Psi_2^-(z)\right]\left[C\Psi_2^+(z') + D\Psi_2^-(z')\right] \\
&= AC\mathrm{e}^{p(z+z')} + BC\mathrm{e}^{-p(z-z')} + AD\mathrm{e}^{p(z-z')} + BD\mathrm{e}^{-p(z+z')}
\end{aligned} \tag{4.7}$$

The coefficients can be obtained from the boundary conditions as follows [81];

$$AC = \frac{2\pi Z \lambda_B}{p}\left[\frac{\tilde{\chi}_{32}\mathrm{e}^{-2pL}}{1 - \tilde{\chi}_{12}\tilde{\chi}_{32}\mathrm{e}^{-2pL}}\right], \tag{4.8}$$

$$BC = \frac{2\pi Z \lambda_B}{p}\left[\frac{\tilde{\chi}_{12}\tilde{\chi}_{32}\mathrm{e}^{-2pL}}{1 - \tilde{\chi}_{12}\tilde{\chi}_{32}\mathrm{e}^{-2pL}}\right], \tag{4.9}$$

$$AD = \frac{2\pi Z\lambda_B}{p}\left[\frac{1}{1-\tilde{\chi}_{12}\tilde{\chi}_{32}\mathrm{e}^{-2pL}}\right], \tag{4.10}$$

$$BD = \frac{2\pi Z\lambda_B}{p}\left[\frac{\tilde{\chi}_{12}}{1-\tilde{\chi}_{12}\tilde{\chi}_{32}\mathrm{e}^{-2pL}}\right], \tag{4.11}$$

where

$$\tilde{\chi}_{12} = \frac{\epsilon_2 p - \epsilon_1 \mathrm{k}}{\epsilon_2 p + \epsilon_1 \mathrm{k}}, \tag{4.12}$$

$$\tilde{\chi}_{32} = \frac{\epsilon_2 p - \epsilon_3 \mathrm{k}}{\epsilon_2 p + \epsilon_3 \mathrm{k}} \tag{4.13}$$

and $\lambda_B = \mathrm{e}^2/k_BT\epsilon_2$ is the familiar Bjerrum length. Substituting eqs (4.8 - 4.13) in eq. (4.7) and simplifying we obtain,

$$\begin{aligned}\tilde{\phi}(\mathrm{k},z,z') &= \frac{2\pi Z\lambda_B}{p}\mathrm{e}^{-p|z-z'|} + \frac{2\pi Z\lambda_B}{p}\left(\frac{1}{1-\tilde{\chi}_{12}\tilde{\chi}_{32}\mathrm{e}^{-2pL}}\right)\\ &\times\left(2\tilde{\chi}_{12}\tilde{\chi}_{32}\mathrm{e}^{-2pL}\cosh[p|z-z'|] + \tilde{\chi}_{12}\mathrm{e}^{-p(z+z')}\right.\\ &\left.+\,\tilde{\chi}_{32}\mathrm{e}^{-2pL}\mathrm{e}^{p(z+z')}\right)\ .\end{aligned} \tag{4.14}$$

We now take the inverse Fourier transform of eq. (4.14) to obtain the potential in real space, noting that the Fourier transform for a function of two variables $f(x,y) \equiv f(s)$, $(s = \sqrt{x^2+y^2})$ is

$$F(\mathrm{k}) = 2\pi\int_0^\infty sf(s)J_0(\mathrm{k}s)ds$$

and the inverse transform is

$$f(s) = \frac{1}{2\pi}\int_0^\infty \mathrm{k}F(\mathrm{k})J_0(\mathrm{k}s)d\mathrm{k}.$$

Then the inverse Fourier transform of $\tilde{\phi}(\mathrm{k},z,z')$, $\phi(s,z,z')$ is obtained as;

$$\begin{aligned}\phi(s,z,z') &= Z\lambda_B\int_0^\infty d\mathrm{k}\frac{\mathrm{k}}{p}J_0(\mathrm{k}s)\mathrm{e}^{-p|z-z'|}\\ &+Z\lambda_B\int_0^\infty d\mathrm{k}\frac{\mathrm{k}}{p}\left(\frac{J_0(\mathrm{k}s)}{1-\tilde{\chi}_{12}\tilde{\chi}_{32}\mathrm{e}^{-2pL}}\right)\\ &\times\left(2\tilde{\chi}_{12}\tilde{\chi}_{32}\mathrm{e}^{-2pL}\cosh[p|z-z'|] + \tilde{\chi}_{12}\mathrm{e}^{-p(z+z')} + \tilde{\chi}_{32}\mathrm{e}^{-2pL}\mathrm{e}^{p(z+z')}\right)\end{aligned} \tag{4.15}$$

We mention that Carnie and Chan [130] obtained a similar expression for the same problem, but due perhaps to an oversight omitted the e^{-2pL} factor in the coefficient of the cosh-function in eq. (4.15).

4.2.2. The pair interaction potentials

The appropriate ion-ion interaction for a pair adsorbed on the interface between media 1 and 2, may readily be obtained from eq. (4.15), by setting $z' = 0$ and $z = 0$, so that $s = r$. The resulting expression provides the value of the potential at distance r along the interface from an adsorbed point-ion of total charge Z. The pair interaction is equal to this potential evaluated at the appropriate pair separation, times the charge on the other ion. If both ions have the same number of charges Z then the pair interaction, $\beta U(r, L)$, is

$$\begin{aligned} \beta U(r,L) &= Z\phi(s=r, z=z'=0) \\ &= Z^2\kappa\lambda_B \int_0^\infty \mathrm{d}\ell \, \frac{\ell}{\tilde{\ell}} J_0(\kappa r\ell) \left[1 + \left(\frac{1}{1-\tilde{\chi}_{12}\tilde{\chi}_{32}\mathrm{e}^{-2\kappa L\tilde{\ell}}}\right)\right. \\ &\quad \left. \times \left(2\tilde{\chi}_{12}\tilde{\chi}_{32}\mathrm{e}^{-2\kappa L\tilde{\ell}} + \tilde{\chi}_{12} + \tilde{\chi}_{32}\mathrm{e}^{-2\kappa L\tilde{\ell}}\right)\right] \end{aligned} \tag{4.16}$$

where we let $\mathrm{k} = \kappa\ell$ so that $p = \sqrt{\kappa^2 + \kappa^2\ell^2} = \kappa\tilde{\ell}$, $\tilde{\ell} = (1+\ell^2)^{1/2}$. It can be seen immediately that in the limit of large L in which the problem reduces to that of only one interface (formed by media 1 and 2), eq. (4.16) reduces to the form obtained by Stillinger [40], namely

$$\beta U(r, L \to \infty) = 2Z^2\kappa\lambda_B\epsilon_2 \int_0^\infty \frac{\ell J_0(\kappa r\ell)}{\epsilon_2\tilde{\ell} + \epsilon_1\ell}\mathrm{d}\ell \, . \tag{4.17}$$

The same is not true of the expression derived in [130], due to the ommission pointed out.

We can now write eqs (4.16) and (4.17) for various values of $\tilde{\chi}_{12}$ and $\tilde{\chi}_{32}$ corresponding to various systems of interfaces in the slab geometry, and for finite and infinite slab thickness L . We will consider only the following representative cases: the air-water only, the air-water-metal, the air-water-air and the air-water-water systems, with the following acronyms: AW, AWM, AWA and AWW respectively.

Case I: Air-water only (AW) system

Here the appropriate pair interaction, $\beta U^{\mathrm{aw}}(r)$ results from eq. (4.17), with $\epsilon_1 = 1$ and $\epsilon_2 = 78.3$. As Hurd [13] has shown, eq. (4.17) can be separated into an exponential and algebraic decaying terms

$$\beta U^{\mathrm{aw}}(r) = \beta U^{\mathrm{yuk}} + \beta U^{\mathrm{Int}} \tag{4.18}$$

where the first term

$$\beta U^{\mathrm{yuk}} = 2Z^2\kappa\lambda_B \int_0^\infty \frac{\ell J_0(\kappa r\ell)}{\sqrt{1+\ell^2}}\mathrm{d}\ell \;=\; 2Z^2\kappa\lambda_B \frac{\mathrm{e}^{-\kappa r}}{\kappa r}, \tag{4.19}$$

is the familiar Yukawa potential with a factor 2, and the second term is

$$\beta U^{\rm Int} \;=\; -2Z^2\kappa\lambda_B \int_0^\infty \hat{\ell} J_0(\kappa r\ell) \left(\frac{\epsilon_{12}\hat{\ell}}{1+\epsilon_{12}\hat{\ell}}\right) {\rm d}\ell \tag{4.20}$$

with $\hat{\ell} = \ell/\tilde{\ell} = \ell/(1+\ell^2)^{1/2}$ and $\epsilon_{12} = \epsilon_1/\epsilon_2$. A numerical analysis of the integral term, eq. (4.20) shows that it grows from weakly negative values at very small pair separations to a positive maximum and decays algebraically to zero at large pair separations. The net interaction potential in eq. (4.18), however, remains repulsive for all range of interactions (see Fig. 4.2).

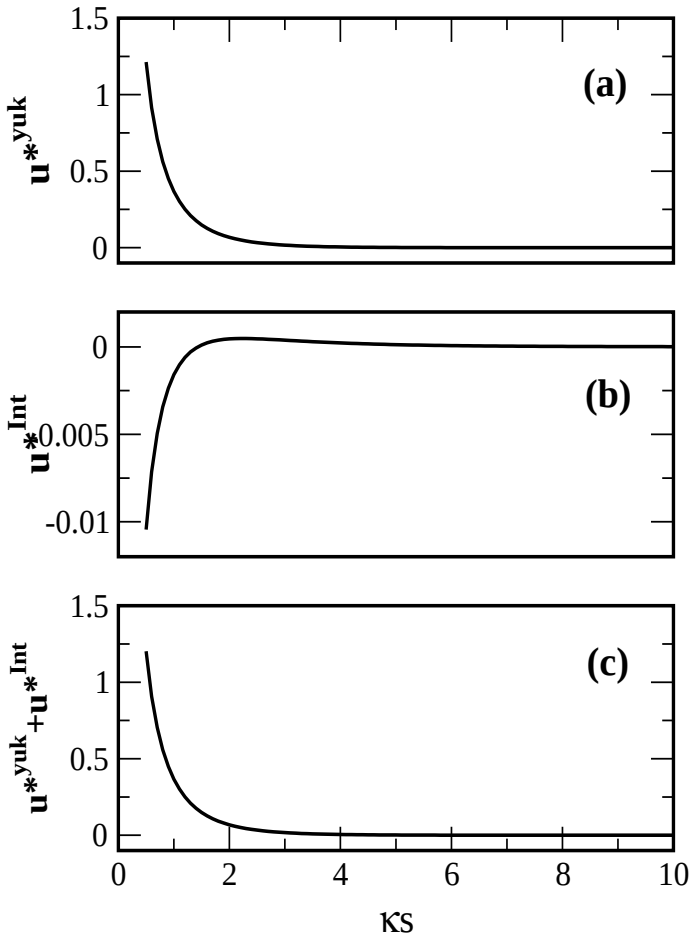

Figure 4.2: Analysis of eq. (4.18): (a) the exponential decay interaction $u^{*\rm yuk} = u^{\rm yuk}/2Z^2\kappa\lambda_B$ versus pair separation distance, κs. (b) the integral term, $u^{*\rm Int} = u^{\rm Int}/2Z^2\kappa\lambda_B$ versus κs and (c) the net interaction, equation (4.18) remains repulsive.

Case II: Air-water-metal (AWM) system

We first consider an approximate limiting case where $\tilde{\chi}_{12} = 1$ and $\tilde{\chi}_{32} = -1$. From eqs (4.12) and (4.13), these values correspond respectively to $\epsilon_{12} = \epsilon_1/\epsilon_2 = 0$, an approximate description of an air-water interface, and $\epsilon_{32} = \epsilon_3/\epsilon_2 = \infty$ for a metallic substrate-water interface. From eq. (4.16) the resulting pair potential, $\beta U^{\rm lim}$ is

$$\beta U^{\rm lim}(r, L) = 2Z^2\kappa\lambda_B \int_0^\infty \hat{\ell} J_0(\kappa r\ell) \tanh(\kappa L\tilde{\ell}) \mathrm{d}\ell \tag{4.21}$$

We see immediately that the approximation $\epsilon_{12} = 0$ is crude enough to kill the second term in eq. (4.18), i.e. eq. (4.20), leaving the system with only the Yukawa interaction, eq. (4.19). We will hence avoid this approximation, i.e. maintain $\tilde{\chi}_{12} \neq 1$, in our pair potentials. Then, from eq. (4.16), the pair interaction for the air-water-metal system, $\beta U^{\rm awm}$ is obtained as

$$\beta U^{\rm awm}(r, L) = 2Z^2\kappa\lambda_B \int_0^\infty \frac{\hat{\ell} J_0(\kappa r\ell)}{\coth(\kappa L\tilde{\ell}) + \epsilon_{12}\hat{\ell}} \mathrm{d}\ell \,. \tag{4.22}$$

Case III: Air-water-air (AWA) system

Here $\tilde{\chi}_{12} = \tilde{\chi}_{32}$. This situation would ideally represent particles suspended in a thin film of water in air. It would also model systems where the ϵ_3-substrate is a low polarizability medium ($\epsilon_3 \sim 1 \to 6$) where the ratio ϵ_{32} is of the same order as ϵ_{12}. The pair potential $\beta U^{\rm awa}(r, L)$ for this system is obtained as

$$\beta U^{\rm awa}(r, L) = 2Z^2\kappa\lambda_B \int_0^\infty J_0(\kappa r\ell) \left(\frac{\epsilon_{12}\hat{\ell}\tanh(\kappa L\tilde{\ell}) + 1}{\tanh(\kappa L\tilde{\ell}) + 2\epsilon_{12}\hat{\ell}} \right) \mathrm{d}\ell \tag{4.23}$$

Case IV: Air-water-water (AWW) system

In this case, $\epsilon_2 = \epsilon_3$ so that $\tilde{\chi}_{32} = (\tilde{\ell} - \ell)/(\tilde{\ell} + 1)$. This represents a hypothetical situation where the substrate has the same dielectric constant as water but without mobile charges. It exposes the effect of the confining substrate on the interaction without image-charge forces. The pair potential is obtained as follows,

$$\beta U^{\rm aww}(r, L) = 2Z^2\kappa\lambda_B \int_0^\infty J_0(\kappa r\ell) \left(\frac{\tanh(\kappa L\tilde{\ell}) + 1/\hat{\ell}}{(1/\hat{\ell} + \epsilon_{12}\hat{\ell})\tanh(\kappa L\tilde{\ell}) + \epsilon_{12} + 1} \right) \mathrm{d}\ell \,. \tag{4.24}$$

The potentials above are still in their integral forms. Unfortunately they cannot be performed analytically without severe approximations. We have therefore performed

the integrals numerically in order to capture sufficient details in the electrostatic interaction. Figure 4.3(a-c) shows the variation of the pair potentials with the pair separation, κr for various interfaces' separation distances, κL. The full solid curve is for the AW system, eq. (4.18) (no substrate) corresponding to $\kappa L = \infty$ for any of the other cases: βU^{awm}, βU^{awa} and βU^{aww} for the AWM, the AWA and the AWW systems respectively. The latter (AWW), is plotted in Fig. 4.3(a) to show the small but finite effect of pure confinement without any dielectric change across the substrate-water interface. The plots clearly show how the pair interaction between two ions trapped at an air-water interface is modified by bringing a substrate from the bulk of the solution to a finite distance very close to the air-water interface. Of particular interest is the opposing effects of the two extreme classes of substrates (AWM and AWA) being investigated. While the effect of decreasing the AWA interfaces' separation κL is enhancing the repulsive pair interaction (Fig. 4.3(b)), the effect of the same action for the AWM system is weakening the repulsive interaction, becoming very short ranged for very small κL (Fig. 4.3(c)). Fig. 4.3(a) for the AWW shows small but similar effect as the AWA system, and confirms again that confinement leads to repulsive interaction. The AWW system will not be investigated further, as its behaviour can be predicted from that of the AWA.

This behaviour can again be explained with the electrostatic image-charge forces discussed in sec. 2.3.1 (see e.g., eq. (2.18) and Fig. 2.3). When a metal substrate ($\epsilon_3 \gg \epsilon_2$) is brought close the air-water interface, the image-charge of the macroion in the metal is of the same magnitude but opposite in sign as the real-charge. The total potential observed at the position of the second macroion is then the sum of terms—positive and negative. The potential then tends to vanish as $L \to 0$. It is the direct opposite in the case of a substrate of the dielectric constant of air ($\epsilon_3 \ll \epsilon_2$). The macroion image-charge in such a substrate is almost the same magnitude and of same sign as the real-charge and the total potential due to the macroion increases in magnitude as $L \to 0$. Electrostatic screening of charges by electrolyte ions does not change this picture qualitatively, but leads just to an additional screening factor in the potential (see e.g., eqs (2.27) and (2.28)). Now, for our case with two point-charges at the air-water interface, this implies that one point-charge (the test charge) sees the potential of two other charges, namely the real charge $+Ze$ at $z = 0$ and its image-charge $-Ze(+Ze)$ at $z = 2L$ in the AWM(AWA) systems respectively. The electrostatic potential at the position of the test charge and thus the interaction potential then reduces in the AWM system and increases in the AWA, relative to the value it has in the absence of a substrate.

Figure 4.3 is plotted only up to a few κr. To reveal the full range functional behaviour of the potentials, we replot Fig. 4.3 in log-log scale up to $\kappa r = 20$. The

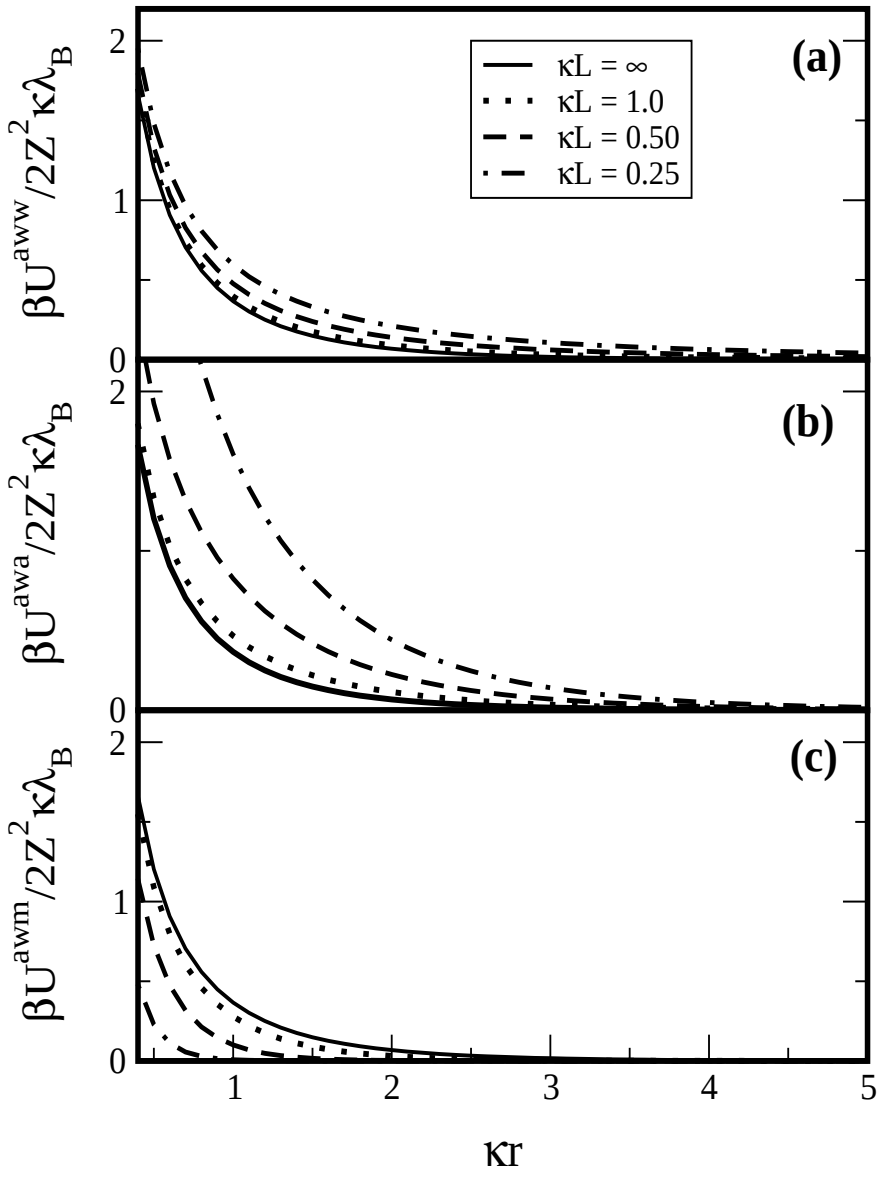

Figure 4.3: Linear plot of pair the potentials, $\beta U(r, L)$ versus pair separation distance, κr for the various system of interfaces; (a) the air-water-water (AWW), (b) the air-water-air (AWA) and (c) the air-water-metal (AWM). The solid line, $\kappa L = \infty$ corresponds to the air-water only (AW) system.

result is shown in Fig. 4.4(a) and (b) for only the AW, AWA and AWM systems. The plots show for various κL, dominant exponential decay at short pair separations and algebraic ($\sim r^{-3}$) decay at large separations, in agreement with Hurd [13]. The $u^{\text{yuk}} = \beta U^{\text{yuk}}/2Z^2\kappa\lambda_B$ of eq. (4.19) is included to emphasize the deviation of the potentials from the pure Yukawa potential decay.

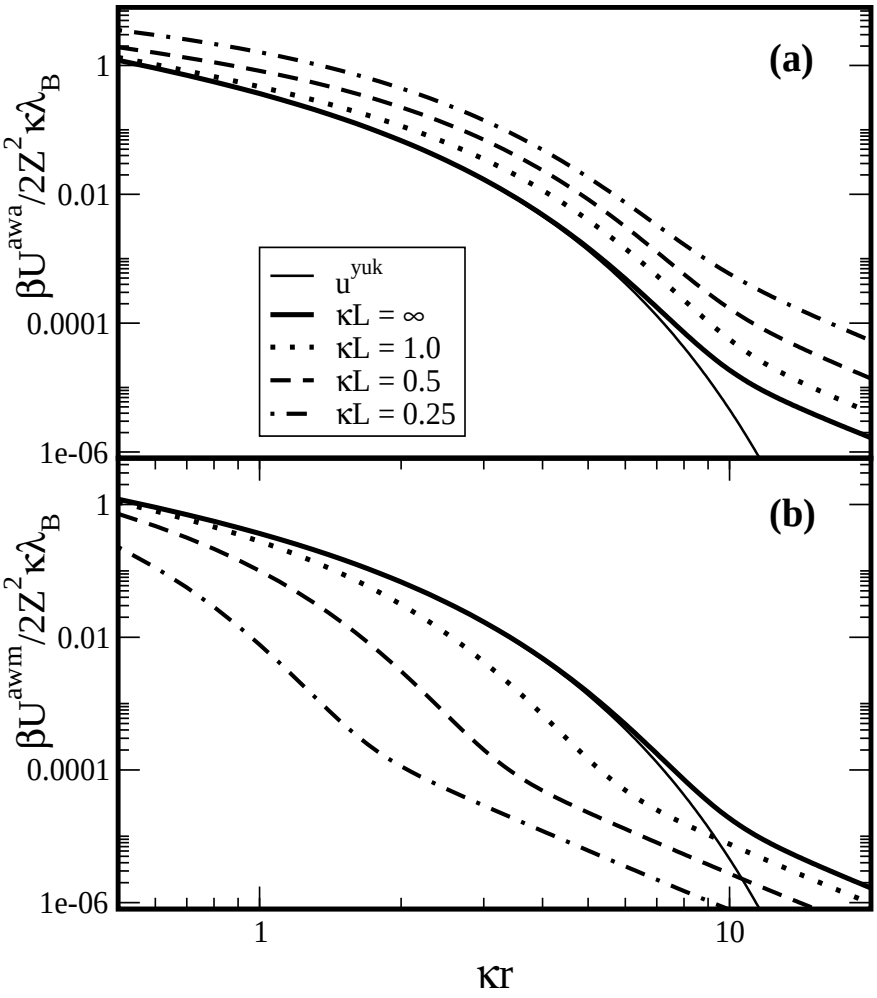

Figure 4.4: Log-log plot of the pair potentials, $\beta U(r, L)$ versus the pair separation, κr for; (a) the AWA system and (b) the AWM system. The thin solid line u^{yuk} is the pure Yukawa exponential decay, eq. (4.19). The AWW system is not included.

We have thus established that the presence of an additional interface has both qualitative and quantitative effect on the pair interaction of macroions adsorbed at an air-water interface. In what follows we are going to probe these potentials further for structural effects on 2D colloidal suspension of particles trapped at an air-water interface via MC simulation.

4.3. One-component Monte-Carlo simulation model

Good fits of the pair potentials, eqs (4.18),(4.22) and (4.23), have been made to obtain energy parameters used in the canonical ensemble MC simulation of the quasi 2D system of colloidal particles trapped at an air-water interface with and without additional substrate interfaces. On the one-component level, only the configurations of the macroions are sampled. The microionic degrees of freedom are averaged out; the pair potential is thus an effective potential. The fit formulas are of the general form for the reduced potential

$$u(\kappa r, \kappa L) = \frac{b_1 \mathrm{e}^{-b_2(\kappa r)}}{(\kappa r)^{b_3}} + \frac{b_4}{(\kappa r)^{b_5}}, \tag{4.25}$$

where $u(\kappa r, \kappa L) = \beta U(\kappa r, \kappa L)/2Z^2\kappa\lambda_B$ with $\beta U(\kappa r, \kappa L)$ as given in eqs (4.18), (4.22) and (4.23). Values of the parameters b_i $(i = 1, 2, 3, 4, 5)$ for various different values of κL and the three systems AWM, AWA and AW are listed in Table 4.3 in the appendix. The AWW system is not considered.

In the simulation, the particles are no longer taken to be point-like ions, but have finite size of diameter $2a$. Hence the density of the 2D system of particles is best described by the particle surface fraction $\phi_{\mathrm{surf}} = \pi a^2 \rho_{nd}$, where $\rho_{nd} = N/S_{\mathrm{box}}$ is the number density with N the total number of the particles in the simulation box of surface area S_{box}. The new pair interaction $(\beta U \to \beta V)$ then includes a hardcore part,

$$\beta V(r) = \begin{cases} \infty; & r < 2a \\ 2(Z/g_\infty)^2 \ \lambda_B \kappa \ u(\kappa r, \kappa L); & r \geq 2a, \end{cases} \tag{4.26}$$

where, the introduction of finite size for the macroions demands the familiar DH correction of the total charge, Z in the form, $Z \to Z/g_\infty$, see eq. (2.32), sec. 2.3.2. The validity of this correction in the present situation is doubtful since only a half of the particle surface is assumed immersed in the aqueous phase and hence only this part carries surface charges. But since for the sizes of colloidal particles being considered here, the g_∞-factor makes only a small difference, we will leave it at that. It is convenient to work with reduced units and we take a as the new unit length scale in the following. Then the independent parameters of our calculation are ϕ_{surf}, $\Lambda = Z^2\lambda_B/a$, $\zeta = \kappa a$ and L/a. Equation (4.26) becomes

$$\beta V(r/a) = \begin{cases} \infty; & r/a < 2 \\ 2\Lambda/g_\infty^2 \ \zeta \ u(\zeta r/a, \zeta L/a); & r/a \geq 2 \end{cases} . \tag{4.27}$$

Table 4.1: Possible combinations of the parameters, Z, a, κ and λ_B resulting to the various values of the reduced parameters, Λ and ζ.

$\Lambda = Z^2\lambda_B/a$	$\zeta = \kappa a$	Z	a(nm)	κ^{-1}(nm)	λ_B(nm)
3433.0	0.250	500	50.0	200.0	0.714
3433.0	0.167	500	50.0	300.0	0.714
1752.0	0.250	350	50.0	200.0	0.714
171.4	0.175	20	3.5	20.0	1.500
87.5	0.175	20	3.5	20.0	0.766

Table 4.1 shows possible combinations of the parameters, Z, a,κ and λ_B resulting in the values of Λ and ζ used in the analysis of the simulation results. In all simulation runs, the 2D rectangular simulation box, with aspect ratio $2:\sqrt{3}$ contained a total of $N = 1024$ particles. The preferred aspect ratio makes the box a unit cell of the target crystal structure (triangular lattice). This minimizes the influence of the simulation box upon the structure of the system. We varied the surface fraction, $\phi_{\rm surf}$, only up to 2% for the latex particles, where the average particles' separation distance is about 6 particle diameters, thus remaining in the low concentration regime. For the proteins however, the variation was up to 20%. Particles were moved only in the lateral $x-y$ directions with periodic boundary conditions according to the standard Metropolis algorithm [131]. Each starting configuration consisted of particles uniformly distributed over the simulation box on a triangular lattice. The systems were equilibrated with about 20000 to 50000 MC cycles by monitoring the energy. One MC cycle corresponds to N (= 1024) attempted moves of a particle. About 5000 to 10000 MC cycles were used to obtain the statistical averages of the density dependent quantities characterizing the particle structures at the interface. These quantities are; the bond orientational order parameter Φ_6, the 2D pair-correlation function $g(r)$ and the orientational correlation function $g_B(r)$, introduced in the following:

The order parameter Φ_6 was introduced by Nelson and Halperin [132] to characterize the structural order in 2D systems. It is viewed as the absolute value of the sixth Fourier component of the bond angle distribution function, which is constant in the isotropic fluid and consists of six equally spaced peaks in the solid phase. It can be given as [92, 133]

$$\Phi_6 = \left\langle \frac{1}{N}\sum_{m=1}^{N}\frac{1}{N_b}\sum_{n=1}^{N_b} \mathrm{e}^{6i\theta_{mn}} \right\rangle . \tag{4.28}$$

The angular brackets indicate the configurational average and θ_{mn} is the angle between some fixed axis (e.g., x or y axis) and the bond joining the $m^{\rm th}$ particle with another $n^{\rm th}$ neighbouring particle, and N_b denotes the number of such particle-

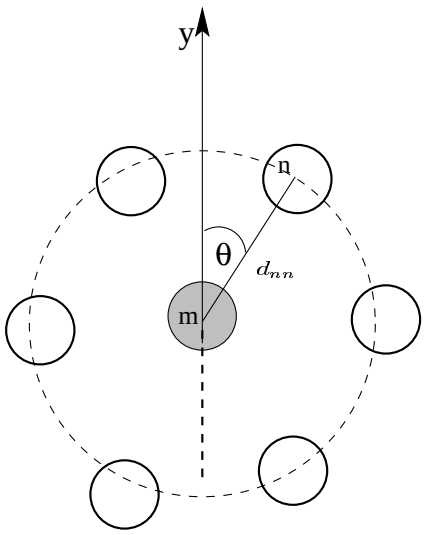

Figure 4.5: Illustrating the determination of the bond orientational order parameter: θ is the angle between a fix axis y and a line joining the centers of a reference particle m and a neighbouring one n whose center-center separation must be equal or less than d_{nn}, the mean separation distance.

neighbour bonds. Various definitions of particle-neighbour distances have been given in the literature, but as long as the shell of the next-nearest neighbours is excluded, details of the neighbourhood definition have a negligible influence on the results [134]. In this present work, we declare two particles as neigbours if their center-center separation is equal or less than $d_{nn} = 1/\sqrt{\rho_{nd}}$, the mean separation between particles in a system of 2D number density ρ_{nd}. The square of the absolute value of the bond orientational order parameter $|\Phi_6|^2$ is used to characterize the structural order of the system [129]. When the system belongs to the fluid phase, $|\Phi_6|^2 \sim 0$. On the other hand, $|\Phi_6|^2 \sim 1$ when the particles form perfect crystalline order of triangular lattice structure.

For further clarification on the structure and phase behavior of the system, the pair-correlation function $g(r)$ and the orientational correlation function $g_B(r)$ are also determined by MC simulation. The $g(r)$ determines the translational order of the particles and can be defined as [6]

$$\begin{aligned} g(r) &= \langle \delta(\mathbf{r}')\delta(\mathbf{r}' - \mathbf{r}) \rangle \\ &= \left\langle \frac{S_{\text{box}}}{N^2} \sum_i \sum_{j>i} \delta(\mathbf{r} - \mathbf{r}_{ij}) \right\rangle , \end{aligned} \tag{4.29}$$

where S_{box} is the 2D volume of the simulation box. On the other hand, the particles'

bond-orientational order is determined by the $g_B(r)$ defined as [135],

$$\begin{aligned} g_B(r) &= \langle \psi_6^*(\mathbf{r}')\psi_6(\mathbf{r}'-\mathbf{r})\rangle \,/\, \langle \delta(\mathbf{r}')\delta(\mathbf{r}'-\mathbf{r})\rangle\,, \\ &= \left\langle \sum_i \sum_{j>i} \psi_6(\mathbf{r}_i)\psi_6^*(\mathbf{r}_j)\delta(\mathbf{r}-\mathbf{r}_{ij}) \right\rangle \Big/ g(r), \end{aligned} \tag{4.30}$$

where $\psi_6(\mathbf{r}_m)$, $m \equiv i,j$ is the local bond-orientational order parameter

$$\psi_6(\mathbf{r}_m) = \frac{1}{N_b}\sum_{n=1}^{N_b} \mathrm{e}^{6i\theta_{mn}}. \tag{4.31}$$

The bond-orientational correlation function is often used to identify the so called hexatic phase where a system possesses short range translational order but a quasi-long range orientational order, being intermediate between the solid crystal phase and the fluid phase. The region in parameter space of existence of the hexatic phase in most systems is very narrow. Hence in order not lose focus on the main aim of this study, we will not pay much attention in identifying this intermediate phase.

4.4. Results and discussion

4.4.1. Latex particles

From the equilibrium states of the various systems studied (AW, AWA and AWM), we investigate the concentration dependence of the squared bond-orientational order parameter $|\Phi_6(\phi_{\mathrm{surf}})|^2$, as well as the pair-correlation function $g(r)$ and the bond-orientational correlation function $g_B(r)$, with a view to understanding the electrostatic influence of supporting substrates on the structural behaviour of charged particles trapped at an air-water interface.

Figure 4.6 shows the variation of the order parameter $|\Phi_6|^2$ with the surface fraction ϕ_{surf}. The two outer curves correspond to fixed distances $L/a = 4.0$ in the AWA and AWM systems, while the middle curve corresponds to particles of the AW system ($L \to \infty$) in the absence of any additional interface. The other two parameters are fixed at $\Lambda = 3433$ and $\kappa a = 0.25$. These parameters are typical of latex particles in highly de-ionized water (for example: $\kappa^{-1} = 200$nm, $a = 50$nm, $\lambda_B = 0.714$nm and $Z \approx 500$, see Tab 4.1). Any other possible combination of the parameters leading to the same values for Λ and κa will lead to the same result. In all three curves, we see that $|\Phi_6|^2 \sim 0$ for a range of colloid densities, indicating that the systems belong to the fluid phase. Then, there appears to be a critical density at which the system

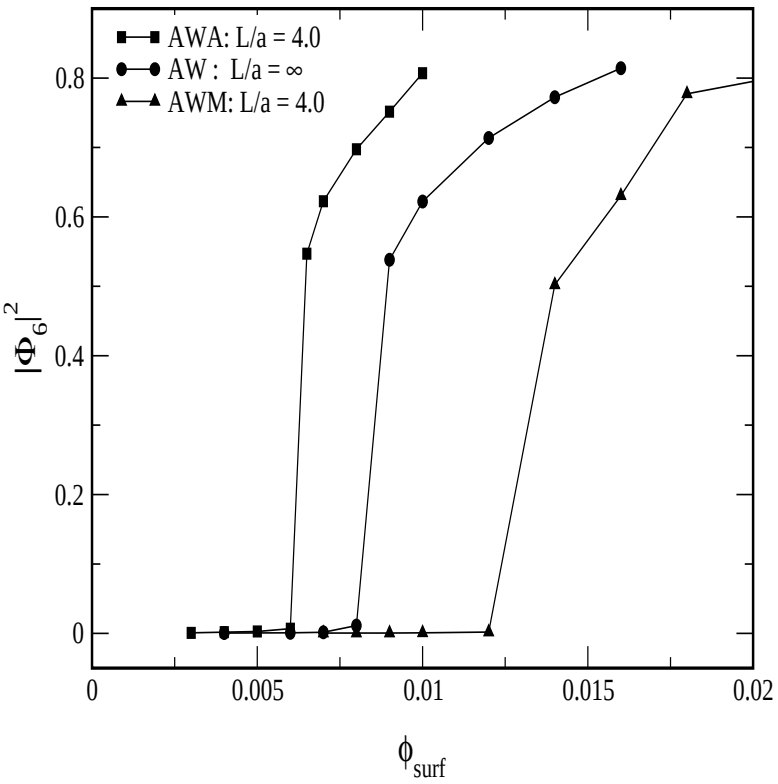

Figure 4.6: The square of the orientational order parameter, $|\Phi_6|^2$ versus the particle surface fraction ϕ_{surf} for the air-water only system (AW), the air-water-air (AWA) and the air-water-metal (AWM) systems when the reduced interfaces separation distance, L/a, is held at 4.0. Other fixed parameters are: $\Lambda \approx 3433$ and $\kappa a = 0.25$.

experiences a jump in the order parameter (to $|\Phi_6|^2 \approx 0.5$) when the system makes transition to the crystalline phase. This $|\Phi_6|^2$ behaviour is quite in agreement with that presented in Ref. [92]. The substrate-water interface again as in the case of the interaction potentials shows a reversing effect in going from the AWA system to the AWM system with respect to the AW system. The AWA system exhibits crystals at densities where the AW and AWM systems shows fluid structures, obviously due to the enhanced repulsive pair interaction potential observed in Fig. 4.3, while bringing a metallic surface near to the 2D system at the air-water interface induces a shift of the freezing density to higher densities. This confirms that, and shows how the additional dielectric substrate affects the crystallization behavior of the 2D colloidal system.

To further expose the distinct effects of the two classes of interfaces, we characterize in Fig. 4.7 the structural features of the systems (parameters as in Fig. 4.6) at a particular density, $\phi_{\text{surf}} = 0.008$. Figure 4.7 shows (a) equilibrated configuration snapshots of

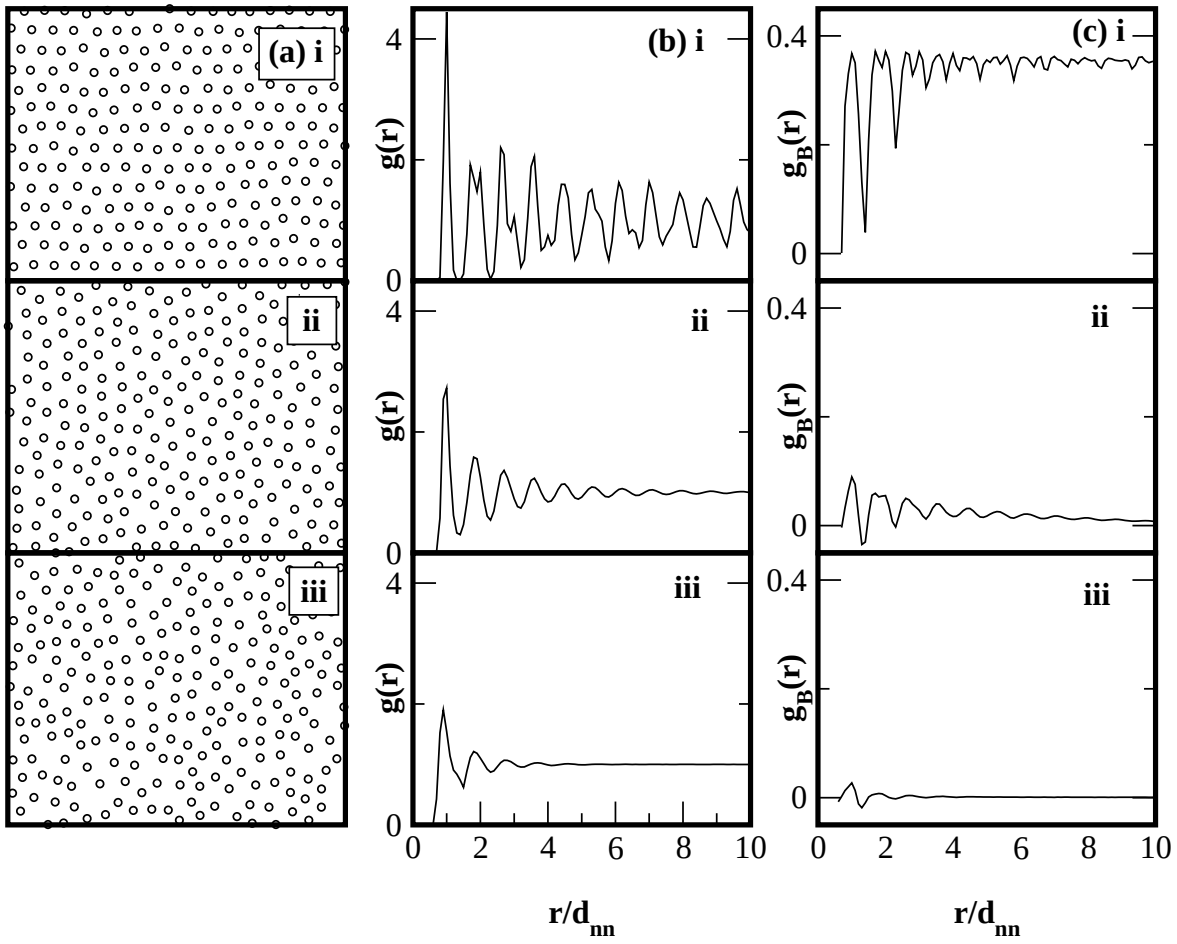

Figure 4.7: Two dimensional structural characterization of the particles trapped at the air-water interface at $\phi_{\rm surf} = 0.008$. The columns: (a) snapshots, (b) the pair-correlation function $g(r)$ and (c) the bond-orientational correlation function $g_B(r)$, and the rows: (i) the AWA system ($L/a = 4.0$), (ii) the AW system ($L/a = \infty$), and (iii) the AWM system ($L/a = 4.0$). Other fixed parameters are as in Fig. (4.6). $d_{nn} = \sqrt{\rho_{nd}}$ is the mean interparticle distance at the given density $\rho = \phi_{\rm surf}/\pi a^2$.

the particles, (b) the pair-correlation functions $g(r)$ and (c) the orientational-correlation function $g_B(r)$, for the three systems: (i) AWA: $L/a = 4.0$, (ii) AW: $L/a = \infty$ and (iii) AWM: $L/a = 4.0$. The figure reveals that at $\phi_{\rm surf} = 0.008$, the AWA system displays clearly a solid phase from the $g(r)$ with quasi-long range translational order, and crystalline order from the point of view of $g_B(r)$ with finite and long-ranged non-decaying values. At the same density, the AWM system shows an isotropic fluid phase where both $g(r)$ and $g_B(r)$ display short range order. The snapshots directly clarify these features. Intermediate between the systems discussed is the no substrate AW system. In this system, while the $g(r)$ shows a short range order, $g_B(r)$ appears quasi-long

ranged, showing a slow decay to zero. This behaviour is an evidence of the existence of the hexatic phase in the melting transition of 2D colloidal suspension at the air-water interface investigated in Ref. [92].

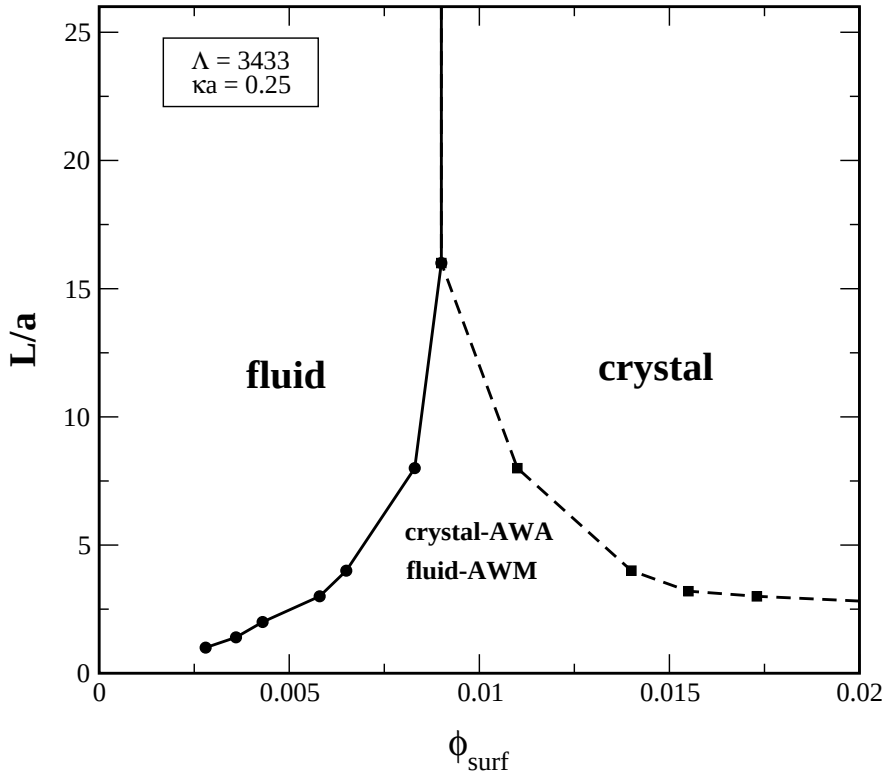

Figure 4.8: Phase diagram in the $[\phi_{\rm surf} : L]$ plane for a set of system parameters corresponding to $\Lambda = 3433$ and $\kappa a = 0.25$. The regions of the indicated phases are: isotropic fluid phase (**fluid**), crystalline solid phase (**crystal**), and either of both phases depending on the dielectric nature of the additional supporting substrate. In the AWA system, this region is crystalline (**crystal-AWA**), while it is fluid in the AWM system (**fluid-AWM**).

In what follows, we will not invest much effort in locating the exact transition density from the isotropic fluid phase to the crystalline solid phase, or vice versa, often achieved by the cummulant method [134]. We will rather assume that transition occurs at around the jump in $|\Phi_6|^2$, i.e., at values of $\phi_{\rm surf}$ corresponding to $|\Phi_6|^2 \approx 0.5$, which is reasonable from the point of view of Fig. 4.6 discussed. Figure 4.8 is a phase diagram based on our model, obtained with the above criterion by systematically calculating $|\Phi_6|^2$ as a function of $\phi_{\rm surf}$ as in Fig. 4.6, for varying values of L/a. In this diagram, the reduced parameters are again $\Lambda = 3433$ and $\kappa a = 0.25$. The figure shows in what regions of the lines drawn for the two systems, AWA and AWM, one expects to find

the fluid phase and the crystalline solid phase. The region labeled 'crystal-AWA' and 'fluid-AWM' belongs to the crystal phase for the AWA system and to the fluid phase for the AWM system. It is seen that at large L, the two lines join into one with values equal to those obtained for the AW system.

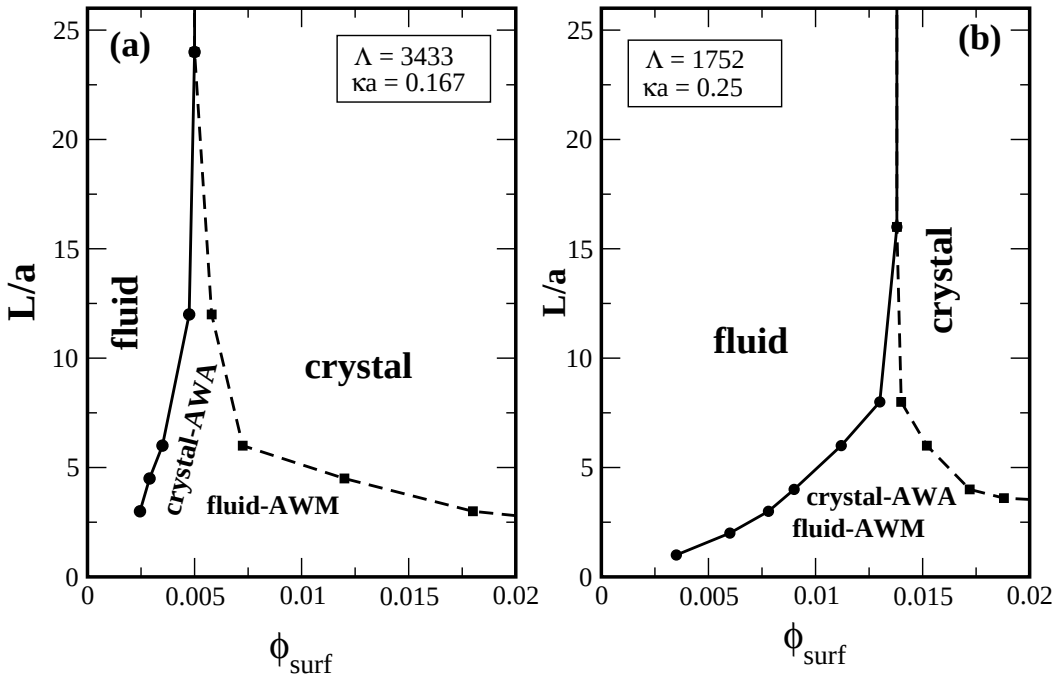

Figure 4.9: Same as in Fig. (4.8) but for (a) $\kappa a = 0.167$: the crystal phase is dominant, and (b) $\Lambda = 1752$: the fluid phase is dominant.

Figure 4.9(a) and (b) show the effect of changing the reduced parameters, Λ and κa. In Fig. 4.9(a), Λ is as in Fig. 4.8 while κa is decreased to 0.167. This could imply, for example, reduction in the screening by reducing the ionic strength of the electrolyte solution (e.g. from $\kappa^{-1} = 200$nm, to $\kappa^{-1} = 300$nm for a fixed $a = 50$nm). This is equivalent to decreasing κL in Fig. 4.3 which leads to stronger and weaker repulsive pair interactions in the AWA and AWM systems respectively. The overall effect on the phase diagram is a quantitative shift in favour of the crystal phase. In Fig. 4.9(b), $\kappa a = 0.25$ as in Fig 4.8 but Λ takes a smaller value, 1752, realized for example by decreasing Z (see Tab 4.1). Again from Fig. 4.3, this will lower the amplitude of the pair potentials for all the systems — AWA, AWM and AW, producing again a shift in the phase diagram but now in favour of the fluid phase.

4.4.2. Protein particles

In the light of the results of the preceding section, we extend the simulations to parameters relevant to protein particles at the air-water interface. Some protein particles studied at the air-water interface are known to be of the order of a few nanometers in dimensions and carry quite small numbers of charges. The net charge on a protein particle is pH dependent and can be varied from negative to positive, taking a vanishing value at the iso-electric point of the protein solution. See Table (4.2) for a list of a few proteins and some of their relevant characteristics. We investigate again the possible influence of a supporting substrate on the phase behaviour of protein particles at the air-water interface. We see immediately from Table (4.2) that the electrostatic coupling quantity, Λ will be very small (~ 100) for any realistic combination of the composite parameters, compared to the latex particles. This is essentially due to the low net charge carried by proteins. We will therefore focus only on the AWA model, which according to the results on latex particles enhances the tendency to crystallize and therefore provides the only possible chance of finding the crystal phase at reasonable particle densities.

Table 4.2: Some proteins particles studied at the air-water interface with some relevant properties and sources.

Protein particle	Tertiary structure	Dimensions (nm × nm × nm)	Hydrodyn. radius (nm)	Charge (pH)	Ref.
Lysozyme	globular	4.5 × 3.0 ×3.0	1.967	+9 (7.0), +12 (3.5)	[97], [136]
BSA*	globular	14.0 × 3.8 ×3.8	3.579	-17 (7.0)	[97]
β-Casein	disordered coil		3.579	-13 (7.0)	[97]
Myoglobin	globular	4.4 × 4.4 ×2.5		+19 (3.5), -5 (9.5)	[136]
Ribonuclease	globular	3.8 × 2.8 ×2.2		+13 (3.5)	[136]
Apoferritin**	globular		6.000	*undetermined*	[137]/ [138]

* Bovine serum albumin

** Apoferritin is the protein, ferritin with a spherical core of about 6nm in diameter containing iron oxide [138]

In the simulations, we probed $\Lambda = 87.54$ and 171.42. The former value could correspond to; $2a = 7.0\text{nm}$, $Z = 20$, and $\lambda_B = 0.766\text{nm}$ (water: T = 278K, $\epsilon_2 = 78.3$), while the latter is obtained by increasing λ_B to 1.5nm assuming a lower polarizability solution of dielectric constant, $\epsilon_2 \approx 40.0$. This assumption is not unreasonable considering that in experiments of protein crystallization, the protein solution is often a concoction whose resultant dielectric constant may be well below that of water. However, the

AWA acronym will still be used to describe the resulting air-solution-air system. For $\epsilon_2 = 40$, a different set of fit parameters must be obtained and are shown in Table 4.4 in the appendix. For salt concentrations typical of protein solutions [97, 136], we fixed κa at 0.175.

Figure 4.10(a) shows the variation of the order parameter $|\Phi_6|^2$ with the surface fraction $\phi_{\rm surf}$ when the AWA interfaces' separation distance L is equal to the particle radius ($L/a = 1.0$). The figure shows that with $\Lambda = 87.54$, the protein particles could not form crystal for the range of surface fraction shown. But increasing Λ to 171.4, the order parameter performs the characteristic jump (here at $\phi_{\rm surf} = .018$) to a high value, so that we can expect well defined crystalline structure at $\phi_{\rm surf} = 0.02$ at the air-solution interface. Figure 4.10(b) shows that the crystalline order existing at the

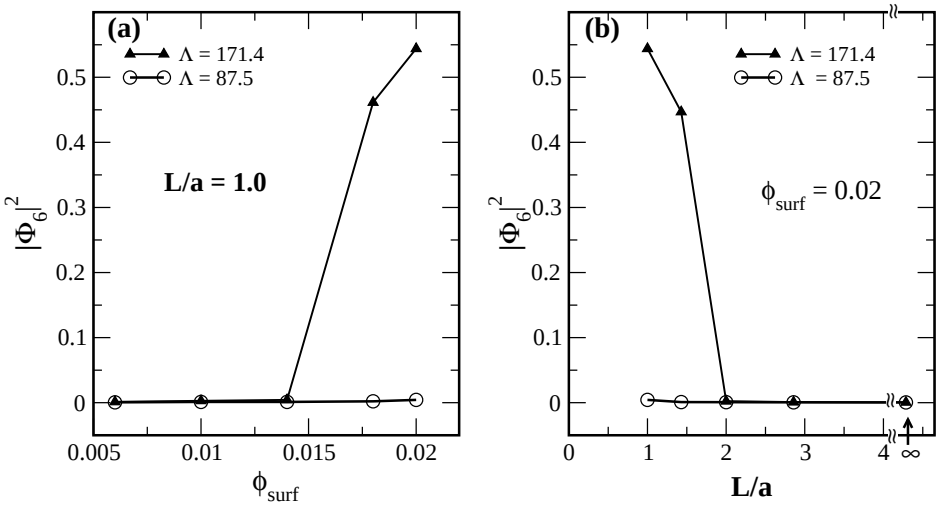

Figure 4.10: The order parameter $|\Phi_6|^2$ versus (a) surface fraction $\phi_{\rm surf}$ and (b) air-water/substrate-water separation distance L/a, for sets of parameters appropriate for protein particles at air-solution interfaces as labeled. In both (a) and (b), $\kappa a = 0.175$.

surface fraction, $\phi_{\rm surf} = 0.02$ in Fig. 4.10(a) collapses to an isotropic fluid phase with also a sudden plunge in the order parameter $|\Phi_6|^2$, when L/a is increased from 1.0. The point on the horizontal axis $L/a = \infty$ corresponds to the AW system (i.e. air-solution only interface).

In Fig. 4.11, we plot the $[\phi_{\rm surf} : L]$-phase diagram for the protein particles ($\Lambda = 171.4$, $\kappa a = 0.175$) with the same freezing criteria used for Figs 4.8 and 4.9 for the latex particles. But unlike the latter, the AWM branch is not included due to the earlier given reason. The protein phase diagram (Fig. 4.11) while qualitatively identical to the latex particle ones, however shows much larger region in $[\phi_{\rm surf} : L]$ plane for the fluid

phase. The system exhibits the crystal phase only at rather very high surface densities, about an order of magnitude larger in comparison with densities for the latex particle. Fig. 4.11 reveals how effective the additional substrate now becomes in promoting crystallization: already at relatively large separations of $L/a = 5$ one observes a clear shift of the freezing transition point from its original value (no substrate) at about $\phi_{\text{surf}} = 0.18$ to $\phi_{\text{surf}} = 0.15$, and at $L/a = 2.5$ freezing sets in already at $\phi_{\text{surf}} = 0.06$, that is, at a protein surface fraction which is a factor 3 smaller than it is in the no substrate system! Figures 4.10 and 4.11 thus demonstrate that, using the

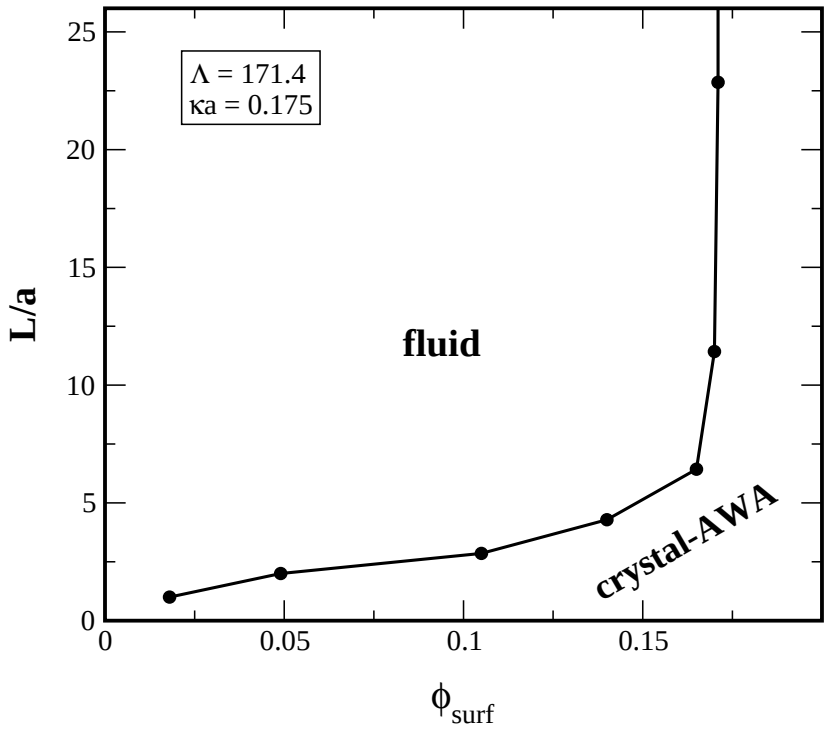

Figure 4.11: Phase diagram for a set of system parameters corresponding to $\Lambda = 171.4$ and $\kappa a = 0.175$ appropriate for protein particles, obtained only for the AWA system.

model pair interaction potentials described in this work, a low polarizability supporting substrate, whose dielectric constant is much smaller than that of water ($\epsilon_3 \ll \epsilon_2$), is capable of inducing crystallization in an otherwise fluid 2D protein system when the separation distance between the substrate and air becomes comparable to the particle size. We however also remark that at such high densities, the average particles' separation distances, d_{nn} become comparable to the particles' size. Apart from the technical problem of requiring more particles in the simulation (which demands more computation time), the neglect of the van-der-Waals attractive forces (which become

more effective with increasing salt concentration) in the model then becomes certainly less justifiable. Also, when $L/a \to 1$, for the small protein size, the use of the DH mean-field theory which neglects correlation of the microions should also be questionable.

4.5. Summary and conclusion

The present chapter has considered the pair interaction potential of two macroions adsorbed at the boundary between an aqueous electrolyte and a gaseous medium, with and without the presence of an additional dielectric substrate in close vicinity of the air-water interface. We considered only three but representative substrate-solution interfaces giving rise to the following system of interfaces: air-water-metal (AWM), air-water-air (AWA) and air-water-water (AWW). Metal represents media of dielectric constants much higher than water ($\epsilon_{\text{metal}} \sim \infty$), air represents media on the opposite end ($\epsilon_{\text{air}} \sim 1$), while the AWW system model systems where the substrate is of the same polarizability as the electrolyte (water). Two similarly charged particles at an air-water interface are known to interact via repulsive electrostatic dipole-dipole potential in addition to the well known Yukawa-like screened Coulomb potential. We showed that the presence of the additional interface results in a modification of the total electrostatic repulsive interaction potential, enhancing it in the case of the AWA system but with a diminishing effect in the AWM system. Applying these model pair interaction potentials, we investigated via MC simulation the density dependent quasi 2D structural and phase behaviour of two classes of colloidal particles, namely, highly charged spheres, such as latex particles and charged globular protein particles, using the bond orientational order parameter, the pair and the bond-orientational correlation functions.

In the case of latex particles, we obtained fluid to crystal transition phase diagrams in the particle density-interfaces separation distances plane $[\phi_{\text{surf}} : L]$ for low salt concentrations. While the AWA system facilitates formation of crystals at low particle concentration relative to the air-water only (AW) system, the AWM system behaves otherwise, in accordance with the opposing behavior of their pair interaction potentials. This then is the essential conclusion of this chapter: it is possible to influence the crystallization behavior of 2D systems of charged particles at the air-water interface by an additional dielectric substrate, brought into the neighbourhood of the air-water interface. This might bear some relevance for protein crystallization in 2D. The positive influence of the AWA system on 2D crystallization of latex particles motivated the extension of the model to investigate 2D crystallization of proteins, where the total charge on the particle is very low ($Z \sim 15$). The protein particles phase diagram obtained

showed some sets of system parameters where it is possible to form 2D crystals when the interfaces separation distance, L becomes comparable with the particles' sizes. The results obtained in this study should be insightful enough to guide the experimentalist in choosing materials and substrate interfaces for growing 2D structures, e.g. crystals at air-solution interfaces.

4.6. Appendix

4.6.1. A: The fit parameters for the pair interaction potentials

In Tables 4.3 and 4.4, we tabulate for reproducibility purposes, the fit parameters b_i, in the fit function $f(r,b) = b_1 e^{-b_2(\kappa r)}/(\kappa r)^{b_3} + b_4/(\kappa r)^{b_5}$, for the interaction potentials $u = \beta U/2Z^2\kappa\lambda_B$ with βU from eqs. (4.18),(4.22), and (4.23). To obtain very accurate fits for the potentials, it was necessary to separate the pair separation distance, κr into small and large.

Table 4.3: The fit parameters b_i for $\epsilon_1 = 1.0$ and $\epsilon_2 = 78.3$. The values corresponding to κL marked '*' are obtained for the air-water-air system, '**' are for the air-water-metal system, and $\kappa L = \infty$ is for the air-water only system.

	κr									
	Small separation: $\kappa r = 0 - 7$					Large separation $\kappa r = 7 - \infty$				
κL	b_1	b_2	b_3	b_4	b_5	b_1	b_2	b_3	b_4	b_5
0.25*	4.36968	1.03332	0.38666	0.05188	1.41822	6.75770	0.79906	1.34639	0.75897	3.20032
0.35*	3.16919	1.06816	0.32458	0.07366	1.87064	4.61932	0.84437	1.16922	0.39803	3.20639
0.50*	2.13406	1.01331	0.39440	0.05023	2.22335	4.72500	0.80606	1.49737	0.16537	3.13671
0.75*	1.30101	0.870893	0.662179	0.02989	2.39797	1.92150	0.91642	0.86393	0.09282	3.20049
1.00*	0.99245	0.77318	0.91866	0.00996	2.51205	1.39635	0.93328	0.78978	0.05493	3.18530
2.00*	0.95501	0.95065	1.01137	0.00543	1.35189	0.76352	0.94202	0.80309	0.02030	3.10277
4.00*	0.98485	0.99191	1.00018	0.00115	1.36693	1.29557	0.90959	1.42098	0.01608	3.07225
∞	0.98395	0.99158	1.00029	0.00126	1.57368	0.81882	1.02088	0.81871	0.02700	3.28884
4.00**	0.98562	0.99227	1.00009	0.00083	1.38556	1.07694	0.98345	1.09445	0.01593	3.07056
2.00**	1.01685	1.03296	0.98923	-0.00379	1.36667	3.47061	1.02433	1.93716	0.01384	3.04663
1.00**	1.23932	1.47238	0.90124	-0.00658	1.46043	102.86300	0.437491	7.39092	0.00796	3.02246
0.75**	1.43582	1.91032	0.83769	-0.00451	1.55401	0.00520	0.58665	2.31473	0.00469	2.95943
0.50**	1.86138	2.89575	0.73788	-0.00177	1.81432	-8.46E-05	0.10370	1.58336	0.0028	2.90339
0.25**	2.84005	5.92461	0.64324	-1.44E-05	5.43621	-4.17E-06	0.21541	0.32290	0.00059	2.76656

Table 4.4: The fit parameters b_i for $\epsilon_1 = 1.0$ and $\epsilon_2 = 40.0$ obtained for protein particles in the air-solution-air system.

	κs									
	Small separation: $\kappa s = 0 - 7$					Large separation $\kappa s = 7 - \infty$				
κL	b_1	b_2	b_3	b_4	b_5	b_1	b_2	b_3	b_4	b_5
0.175	5.90557	1.11571	0.30643	0.19672	1.30551	16.69520	0.46874	2.73382	2.20759	3.08202
0.250	4.24392	1.10785	0.29197	0.14138	1.51621	9.89539	0.60330	2.20350	1.26082	3.13354
0.350	2.83067	1.00914	0.38945	0.08782	1.69163	7.10615	0.67153	1.97503	0.67289	3.14514
0.500	1.73127	0.84728	0.60044	0.05126	1.81383	4.73814	0.73498	1.73526	0.34197	3.14931
∞	0.97308	0.98551	1.00007	0.00154	1.14008	2.00690	0.82914	1.92410	0.02845	3.02717

5

The Cell model method for interfacial suspensions

5.1. Introduction

As in the previous chapter, the present one involves suspensions of colloids near typical dielectric interfaces. But as opposed to the former where studies were based on the DH theory and one-component MC, we here come back to the non-linear PB theory, and primitive MC simulations, in cell model approximations. In a primitive MC simulation, all types of ions in the suspension are explicitly accounted for. The work in this chapter will reveal the influence of the other macroions in the suspension on the total force on a macroion near a dielectric interface as opposed to the work in chapter 2 where only a single macroion was considered. Another comparison with the system in chapter 2 is that the wall is also hard and impenetrable. Again the key words here as in all other chapters, include image-charges and confinement effects. We also show how these effects can modify the effective charge of the interfacial macroion.

The cell model approximation is a common method to reduce the complicated many-body problem of a macroionic colloidal suspension to an effective one-body system [139-144]. A difficult alternative to the cell model is the many-body primitive (MBP) model. In this model, the solvent is treated as a continuum, being characterized by just its dielectric constant. The macro- and microions are modeled as charged hard spheres in the solvent, though the microions are often also treated as point-charges. A major limitation of the MBP model is that the total number of particles, N (macroions plus microions) that can be simulated is rather small being limited by the speed and

efficiency of computation. This is because N is proportional to the total charge on the macroion Z. For example, in a system of N_m macroions, each releasing $N_c = Z$ monovalent counterions (microion), the total number of particles $N = N_m(1 + Z)$. Addition of salt ions further increases the number. In their various studies relating to colloidal suspensions, Linse *et al.* [145-149] have made steady progress in the number of particles simulated, achieving recently, $Z = 60$, which for a mere $N_m = 80$ macroions results in $N = 4880$ particles, quite a large number for any average computers. One further approximation to the MBP model is to eliminate the microionic degrees of freedom. This results in the one-component model, in which the charged colloids and their atmospheres of microions are averaged into *dressed* macroions. The *dressing* microions are characterized by the Debye screening constant κ. This method enables the use of more macroions in simulations, as has been used already in the previous chapter in 2D systems of colloids at the air-water interface. The use of the one-component model is mainly justified when one is not particularly interested in the actual distribution of the microions but rather in the equilibrium configuration of the macroions. A less approximate approach is the description, on a mean field level in which for a colloidal suspension, one has to solve the multi-centered PB equation for every possible colloidal configuration $\{\mathbf{R}\}$ to obtain the mean-field electrostatic potential $\phi(\{\mathbf{R}\})$ and then the appropriate thermodynamic functions [78].

The cell model approximation provides a way out of the difficulties or shortcoming of the above described methods provided its own assumptions are tolerable. These assumptions include:

1. Each macroion is located in a cell whose volume equals the volume per macroion in the suspension.

2. Every macroion has identical environment and hence every cell is identical in volume and shape.

3. Each cell is electrically neutral, and the cell boundaries, whichever geometry is assumed, are assumed to be surfaces of zero electric field.

It therefore suffices to consider just one cell instead of the whole suspension. The many-body effects as opposed to an isolated macroion, come from the boundary conditions on the cell surfaces as well as the macroion density or volume fraction relating to the cell volume.

The cell model can be constructed and analyzed for various geometrical shapes of the cell, e.g. spheres, cubes, cylinders, e.t.c., and for various configurations or positions of the macroion in the cell — centric or eccentric, see Refs [78, 150-152] for some details.

We will be concerned here mainly with constructing and describing interfacial cells where the boundaries of the cell are no longer just only the fictitious constructs, but include real walls whose dielectric constant may be sharply different from that of the suspension. As usual, we will look for effects due to image-charges and confinements.

This chapter is divided into two main parts: In the first part, the essential features and results of an interfacial cylindrical PB cell model [78, 153] are presented. More details can be found in the latter references. The presentation is necessary for completeness, since the PB methods in the previous chapters have produced only effective interactions. The second part is devoted to a primitive MC simulation in a similar but cubic cell model, the geometry of the cell in each technique being for convenience. Results from both techniques are compared and discussed where possible.

5.2. Interfacial Poisson-Boltzmann cell model

5.2.1. The cylinder model

The charge-stabilized colloidal suspension is here being modeled by colloidal charged spheres that are suspended in a solvent and surrounded by microions. A finite concentration n_m of these spherical macroions is assumed, so that the volume per macroion is $V_{WS} = 1/n_m$ (this is equal to the Wigner-Seitz (WS) cell volume in the crystalline phase). The macroion has a radius a and fills a volume $V_m = 4\pi a^3/3$. Each bears Z positive charges and thus produces the same number of singly charged, negative, point-like counterions, whose concentration then is $c_0 = Z/\tilde{V}_{WS}$ with $\tilde{V}_{WS}$ being the part of the WS cell volume that is not already occupied by the macroion, $\tilde{V}_{WS} = V_{WS} - V_m$. For simplicity of calculation, the system is assumed salt-free, i.e. the microions are made up only by the counterions. This assumption is good for highly de-ionized solutions and/or for suspensions of sufficiently high concentration.

The forces between the macroions are determined by the (inhomogeneous) distribution of the microionic fluid between them. On a mean-field level of description, this distribution of the mobile microions can be calculated from the PB equation [154]. Though being originally designed for the case of isolated charged objects in an ionic solution, the PB theory applies equally well to concentrated suspensions of charged colloids, provided the cage of neighboring macroions is modeled by a cell of finite volume, to which the macroion is confined. The entire problem of finding the density distribution then reduces to solving the PB equation inside a single cell only. In a bulk suspension, each macroion is assumed to be located at the center of its cell, and all the cells of the suspension have the same volume and shape, most commonly spheri-

cal cells [5, 155]. The presence of the other particle of the suspension are taken into account by the appropriate choice of the boundary conditions. The boundary conditions plus the PB equation then constitutes a BVP whose solution provides the mean electrostatic potential and thus a microionic density distribution. From it, one can then derive general thermodynamic quantities of the suspension, such as, for instance, the osmotic pressure [5], or more specific quantities, such as the effective pair-forces between the particles [151].

Considering here a suspension that borders to a dielectric interface, a cell model is suggested that is adapted to a planar interfacial wall (Fig. 5.1). The WS cell of a colloidal particle near to a dielectric interface is now assumed to have the shape of a cylinder of radius r_0 and length z_1 (the z-axis is perpendicular to the wall, with $z = 0$ defining the interface). r_0 is given by the volume of the WS cell, $V_{WS} = \pi r_0^2 z_1$, with the additional assumption that the cell has the same aspect ratio as a cube, $z_1 = 2r_0$. The macroion inside this cell is situated at $z = z_0$ and $r = 0$. At $z = 0$, the dielectric constant of the medium changes from ϵ' to ϵ.

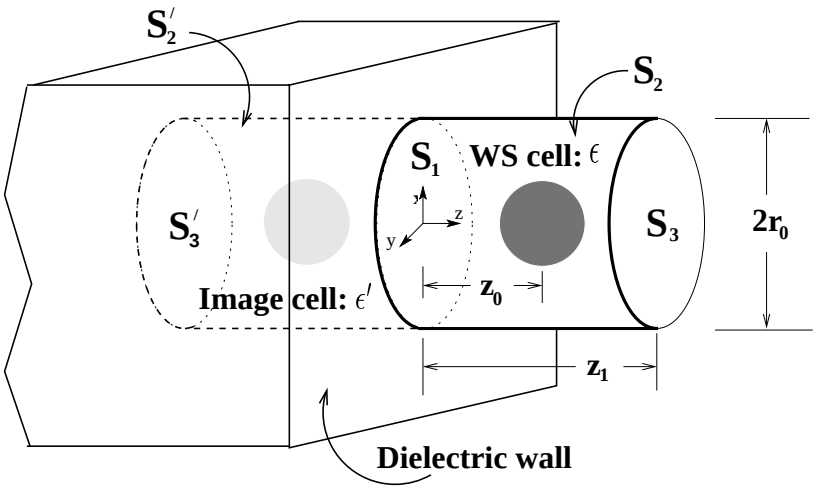

Figure 5.1: The interfacial cell model: a colloid of charge Ze is located at a position z_0 inside a cylindrical Wigner-Seitz (WS) cell of length z_1 and radius r_0 with $2r_0 = z_1$. This cell is filled with Z counterions and confined by three surfaces S_1, S_2 and S_3, of which S_1 is a dielectric interface where the dielectric constant of the medium changes from ϵ to ϵ'. In the ϵ' medium, there is the mirror image of the original cell, the image cell, with the confining surfaces S_1, S_2' and S_3'.

Inside this interfacial cell, the PB equation (in cylindrical coordinates) to be solved in the salt-free case under consideration reads,

$$\nabla^2 \phi(r, z) = 4\pi \lambda_B \rho(r, z) \tag{5.1}$$

with a charge density $\rho(\mathbf{r})$ that depends on ϕ, the now familiar normalized mean electric potential, in the following way

$$\rho(r,z) = c_0 \mathrm{e}^{\phi(r,z)} \Theta(R(r,z) - a) + \rho_m(r,z) \; . \tag{5.2}$$

The charge distribution $\rho(r,z)$, eq. (5.2), consists of two terms of which the first is the contribution of the microions in the region exterior to the colloid. This is ensured by the Θ step function, which changes from zero to one when its argument becomes greater than zero. R is the radial distance from the center of the colloid, $R^2 = r^2 + (z - z_0)^2$. The second term in eq. (5.2), ρ_m, is the charge distribution of the colloid, whose charges are usually assumed to be homogeneously smeared out over the colloidal surface. To reduce grid errors in the numerical procedure, they are however taken to be homogeneously distributed in a thin spherical shell near to the colloidal surface. This shell is defined by the two radii b and a ($b < a$, $a - b << a$). The colloidal charge density then reads

$$\rho_m = -\frac{3Z\Theta(a-R)\Theta(R-b)}{4\pi(a^3 - b^3)} \; , \tag{5.3}$$

and is not dependent on the electrostatic potential.

In order to be able to set up a BVP, one has to specify the boundary conditions for the cylinder cell. Let us label the three confining surfaces of the cell S_1, S_2 and S_3, the first one being the interface to the dielectric medium, the second is the surface of the cylinder and the last is the surface bordering the next cell towards the bulk suspension (see Fig. 5.1). If for the moment one assumes the colloidal particle to be located at the center of the cell, $z_0 = 0.5 z_1$, then the boundary conditions at S_2 and S_3 follow from the assumption that the corresponding surfaces lie sufficiently near to the mid-planes between two neighbouring colloids where, for symmetry reasons, the electric fields exactly cancel out. The boundary condition at the S_1 surface follows from the requirement that the jump in the normal component of the electric displacement field across the interface must be equal to the surface charge density, $-e\sigma$ at the interface. Put together, the following BVP is obtained:

$$\begin{aligned}
\left(\partial_r^2 + \tfrac{1}{r}\partial_r + \partial_z^2\right)\phi(r,z) &= 4\pi\lambda_B\Big(c_0 \mathrm{e}^{\phi(r,z)}\Theta(R-a) + \rho_m(r,z)\Big) \\
S_1 : \qquad \epsilon \partial_z \phi\big|_{z=0+} &= \epsilon' \partial_z \phi\big|_{z=0-} + 4\pi e^2 \beta \sigma \\
S_2 : \qquad \partial_r \phi &= 0 \\
S_3 : \qquad \partial_z \phi &= 0 \; .
\end{aligned} \tag{5.4}$$

In addition, one requires that (i) the potential is continuous across the interface and that (ii) the WS cell must be electrically neutral. One therefore chooses the additive constant of ϕ such that

$$c_0 \int_{\tilde{V}_{WS}} \mathrm{e}^{\phi} dV = Z + \Sigma \; ; \tag{5.5}$$

because the total number of counterions in a cell equals the sum of the colloidal charge number plus the interfacial charge number, $\Sigma = \sigma\pi r_0^2$.

It is more convenient to work in reduced units and for all length scales the radius a of the colloid is taken as the unit in the following. Recalling that $c_0 = Z/\tilde{V}_{WS}$ and realizing that

$$\tilde{V}_{WS} = V_m \frac{1-\phi_{vol}}{\phi_{vol}} \tag{5.6}$$

with $\phi_{vol} = V_m/V_{WS}$ being the volume fraction and $V_m = 4\pi/3$ the volume of the colloidal particle, eq. (5.4) using eqs (5.3) and (5.6) can be written as

$$\begin{array}{rrcl} & \left(\partial_r^2 + \frac{1}{r}\partial_r + \partial_z^2\right)\phi(r,z) & = & 3\tilde{\lambda}_B Z\left(\frac{\phi_{vol}}{1-\phi_{vol}} e^{\phi(r,z)}\Theta(R-1) - \frac{\Theta(1-R)\Theta(R-b)}{1-b^3}\,,\right) \\ S_1: & \partial_z\phi\big|_{z=0+} & = & \frac{\epsilon'}{\epsilon}\partial_z\phi\big|_{z=0-} + 4\pi\tilde{\sigma} \\ S_2: & \partial_r\phi & = & 0 \\ S_3: & \partial_z\phi & = & 0\,, \end{array} \tag{5.7}$$

where $\tilde{\lambda}_B = \lambda_B/a$ and $\tilde{\sigma} = a\lambda_B\sigma$. From eq. (5.7), one can notice that the input parameters of the whole problem have been reduced to just four independent input parameters, which are the volume fraction ϕ_{vol}, the ratio of dielectric constants ϵ'/ϵ, the scaled colloidal charge $Z\tilde{\lambda}_B$ and the scaled interfacial surface charge $\tilde{\sigma}$. The parameter b ($b < 1$) also appearing in eq. (5.7), has been introduced for technical reasons only and does not affect the results.

That the problem can be reduced to four independent parameters only, is owed to the fact that the PB equation in the salt-free case scales with $Z\lambda_B/a$, an observation made also by Groot [155]. This scaling property is lost when salt ions are present which is the main reason for considering the salt-free limit. It enables one to study the problem by playing through only four parameters. However, since the main interest here is to study the image-charge effects on colloidal particles, the problem is simplified further by setting $\sigma = 0$.

In a purely electrostatic problem, the complicated boundary condition at S_1 in eq. (5.7) is satisfied by means of the image-charge method, where every ion of charge q in the neighborhood of the dielectric wall has an image-charge, $q\chi$ in the $z < 0$ half-space. The factor χ first defined in eq. (2.18) can be expressed as,

$$\chi = \frac{1-\epsilon'/\epsilon}{1+\epsilon'/\epsilon} \tag{5.8}$$

For the most experimentally relevant cases, it suffices to investigate the ratios ϵ'/ϵ between zero and one only, so that χ varies between $\chi = 1$ (for $\epsilon'/\epsilon = 0$) and $\chi = 0$ (for

$\epsilon'/\epsilon = 1$). That means that the image-charges for $\epsilon'/\epsilon = 0$ will have the same sign and magnitude as the original charges, while they will be nonexistent when $\epsilon'/\epsilon = 1$. The image-charge method can be applied directly in MC simulation, but only implicitly in a PB problem, through the boundary conditions as e.g., the iterative procedure explained below to solve eq. (5.7) [78, 153].

Note that the BVP of eq. (5.7) leads back to a bulk cell problem, if we choose $\sigma = 0$ and $\epsilon' = 0$. For then, the electric field at all three sides are the same in accordance with the symmetry requirement in a bulk situation. The only difference to the standard PB cell model [5, 155] then remains the cylindrical shape of the cell as opposed to the spherical cells usually assumed. But with regards to the density profiles, this difference has proven to be insignificant. At first, one might think that a choice $\epsilon' = \epsilon$ should give the bulk situation; but from eq. (5.8), we know that $\epsilon' = 0$ means that the image-charges take the maximum values ($\chi = 1$). The ion distribution in the cell at $z > 0$ thus has perfect mirror picture at $z < 0$. The latter then simulate the density distribution in a next neighbour cell in bulk. Hence, for symmetry reasons, the normal component of the electric field must vanish at $z = 0$. The bulk situation is thus recovered.

In the iterative procedure, the boundary condition at S_1 when $\epsilon' \neq 0$, is utilized to link the potential at $z > 0$ to the potential at $z < 0$ which is a solution to the Laplace equation. To calculate the potential at $z < 0$ an image cell in the negative half-space ($z \leq 0$) is constructed, where the dielectric constant is ϵ' (see Fig. 5.1). It is the mirror image of the original interfacial cell at $z \geq 0$, with confining surfaces; S_1, S_2' and S_3'. There are no real charges in this cell, so the problem to solve is the following BVP,

$$\begin{array}{rrcl} & \left(\partial_r^2 + \frac{1}{r}\partial_r + \partial_z^2\right)\phi(r,z) & = & 0 \\ S_1: & \phi\big|_{z=0} & = & v(r) \\ S_2': & \partial_r\phi & = & 0 \\ S_3': & \partial_z\phi & = & 0.\,, \end{array} \tag{5.9}$$

with a potential $v(r)$ at S_1 to be specified soon. Equation (5.9) has the following solution

$$\phi(r,z) = \sum_{m=1}^{\infty} A_m J_0(y_{0m}\frac{r}{r_0}) \cosh\left(y_{0m}\frac{z+z_1}{r_0}\right) \tag{5.10}$$

where the coefficients A_m are given by

$$A_m = 2\Big(\cosh\left(y_{0m}\frac{z_1}{r_0}\right) r_0^2 J_0^2(y_{0m})\Big)^{-1} \int_0^{r_0} v(x) x J_0(y_{0m}\frac{x}{r_0}) dx\,. \tag{5.11}$$

In these expressions, J_0 and J_1 are respectively the Bessel functions of order zero and

one, and y_{0m} is the m^{th} root of the function J_1. The derivative of eq. (5.10) at $z = 0$ is

$$\partial_z \phi(r,0) = \sum_{m=1}^{\infty} B_m J_0(y_{0m}\frac{r}{r_0}) \int_0^{r_0} v(x) x J_0(y_{0m}\frac{x}{r_0}) dx \tag{5.12}$$

with

$$B_m = \tanh\left(y_{0m}\frac{z_1}{r_0}\right) \frac{2y_{0m}}{r_0^3 J_0^2(y_{0m})}\,. \tag{5.13}$$

With eqs (5.9) to (5.13), an iterative scheme to solve eq. (5.7) can be given. Let $\phi^{(n)}$ be the potential in the n^{th} iteration cycle. To obtain this potential one needs to know $\partial_z \phi^{(n)}\big|_{z=0+}$, which can now be obtained from eq. (5.12). This expression in turn is based on the knowledge of the potential at $z = 0$, that is on $v(r)$, for which the potential from the previous iteration step $\phi^{(n-1)}$ is taken. Equation (5.7) can be rewritten once more as follows,

$$\begin{array}{rrcl}
 & \left(\partial_r^2 + \frac{1}{r}\partial_r + \partial_z^2\right)\phi^{(n)}(r,z) & = & 3\tilde{\lambda}_B Z\left(\frac{\phi_{vol}}{1-\phi_{vol}} \mathrm{e}^{\phi^{(n)}(r,z)} \Theta(R-1) - \frac{\Theta(1-R)\Theta(R-b)}{1-b^3}\,,\right) \\
S_1: & \partial_z \phi^{(n)}\big|_{z=0+} & = & \frac{\epsilon'}{\epsilon}\left(\sum_{m=1}^{\infty} B_m J_0(y_{0m}\frac{r}{r_0}) \int_0^{r_0} \phi^{(n-1)}(x,0) x J_0(y_{0m}\frac{x}{r_0}) dx\right) \\
 & & & +4\pi\tilde{\sigma} \\
S_2: & \partial_r \phi^{(n)} & = & 0 \\
S_3: & \partial_z \phi^{(n)} & = & 0\,,
\end{array} \tag{5.14}$$

plus the condition

$$c_0 \int_{\tilde{V}_{WS}} \mathrm{e}^{\phi^{(n)}} dV = Z + \Sigma\,; \tag{5.15}$$

for the choice of the additive constant of $\phi^{(n)}$. The coefficients B_m appearing in eq. (5.14) are to be taken from eq. (5.13). As an initial value for the potential one can take the solution of eq. (5.7) for $\epsilon' = 0$. In practice, one varies the ratio ϵ'/ϵ starting from $\epsilon'/\epsilon = 0$ and takes the solution for a given value of this ratio as an initial guess for the next higher value.

5.2.2. Force on the colloidal sphere

Given the solution ϕ from eq. (5.14), the force acting on the colloid can be calculated. Due to cylindrical symmetry, this force is directed in z direction with z component, F_z. It can be obtained by integrating the stress-tensor $\vec{\vec{T}}$,

$$\vec{\vec{T}} = \left(\Pi + \frac{\epsilon}{8\pi}E^2\right)\vec{\vec{I}} - \frac{\epsilon}{4\pi}\vec{E}\vec{E}\,, \tag{5.16}$$

(Π is the local osmotic pressure, $\vec{E}$ the electric field) over a surface S enclosing the colloidal particle,

$$F_z = \int_S dS\, \vec{n} \cdot \vec{\vec{T}} \cdot \vec{e}_z \,. \tag{5.17}$$

$\vec{n}$ is a unit vector directed normal to the surface S, $\vec{e}_z$ is a unit vector in the positive z direction. A natural choice for the enclosing surface are the three surfaces confining the cylindrical cell, i.e. S_1, S_2 and S_3. Equation (5.17) can be evaluated to take the form:

$$\gamma F_z = \gamma F(z=0) - \gamma F(z=z_1), \tag{5.18}$$

where the factor $\gamma = 4\lambda_B\beta$ renders the force dimensionless, and

$$\gamma F(z) = \int_0^{r_0} \Big[\frac{6\tilde{\lambda}_B Z \phi_{vol}}{1-\phi_{vol}} \mathrm{e}^{\phi(r',z)} + \Big(\partial_r \phi(r',z)^2 - \partial_z \phi(r',z)^2\Big)\Big] r' dr' \,. \tag{5.19}$$

The first term in eq. (5.19) is due to the local osmotic pressure while the second accounts for the stress induced by the electric field.

5.2.3. Results and discussion: Poisson-Boltzmann cell model

We seek to obtain an idea as to what an effect a dielectric interface will have on the structure of a concentrated colloidal suspension, and this means in particular, if there is an additional wall–induced force acting on an interfacial colloid. In the framework of the interfacial cell theory presented above, we are now in the position to answer this question with the help of eqs (5.14) and (5.18). As mentioned earlier we expect two distinct relevant effects namely, confinement and image-charge effects. By confinement effect, we mean that the electrolyte is confined to the half-space where $z > 0$ by the very existence of the wall. A spherical double layer around a colloidal particle approaching this wall will therefore become distorted and this distortion will necessarily cost free energy. Therefore, repulsion is to be expected, when the particle is sufficiently close to the wall for this effect to occur. Image-charges exert additional forces on the ions in the interfacial cell. To predict their effect on the colloidal particle, we need to remember that the colloid is located at the center of a cell that borders not only to the dielectric medium (at S_1, see Fig. 5.1) but also to the next cell bordered by S_3. The ions inside the interfacial cell will therefore be exposed not only to the image-charges from the region $z < 0$ but also to the charges of the neighboring cell at $z > z_1$. It is again necessary to point out that these charges do not appear explicitly in the PB scheme, but enter the calculation through the boundary conditions in eq. (5.14). This is the reason why the actual force in eq. (5.18) is the difference between two terms: one

arising from the image-charges, $\gamma F(0)$, the other from the charges in the neighboring cell, $\gamma F(z_1)$.

For all cases where $\chi < 1$, we can thus predict an attractive net force pulling the colloid towards the wall because the image-charges with a charge of χq will exert a force that is, though repulsive, not strong enough to balance the forces from the corresponding ions in the cell at $z > z_1$, i.e. $\gamma F(0) < \gamma F(z_1)$ in eq. (5.18). The effect resulting from this charge imbalance has been termed "image-charge effect" [78, 153]. When $\epsilon' = 0$ ($\chi = 1$), the image-charges are expected to match the charges from $z > z_1$, and a totally symmetrical, bulk-like situation is recovered where there is no net force on the colloidal particle, $\gamma F(0) = \gamma F(z_1)$.

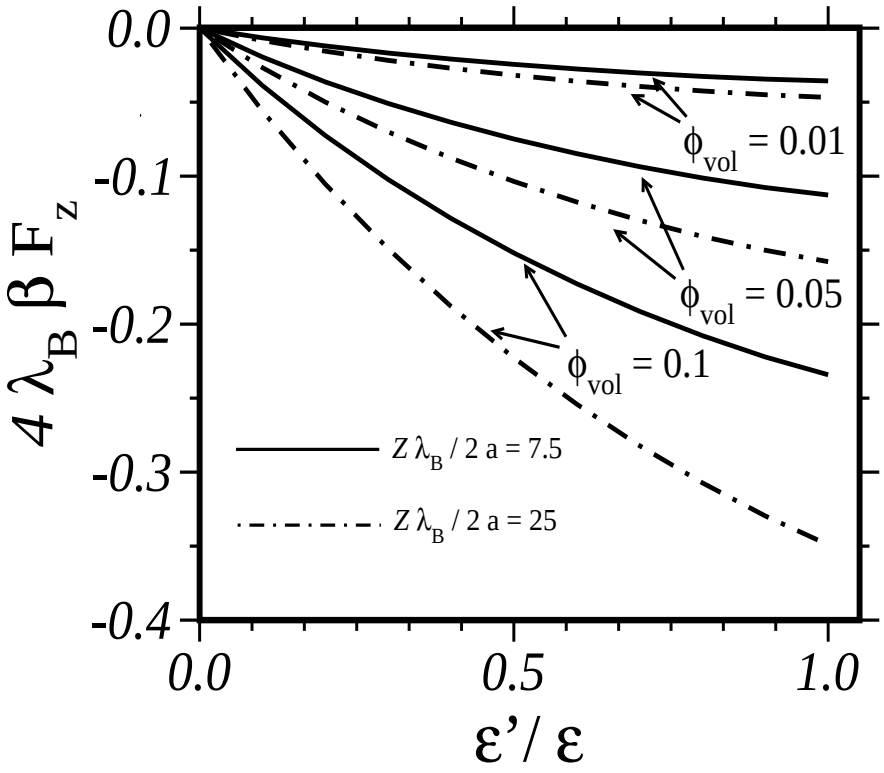

Figure 5.2: The total force acting on a colloid located at the center of an interfacial cell for varying ratios of ϵ'/ϵ. The force is attractive and grows with increasing volume fraction ϕ_{vol} and scaled colloidal charge $Z\lambda_B/2a$.

Figure 5.2 gives the net force acting on the colloidal particle in the center of its cell as a function of the ratio ϵ'/ϵ for various values of $Z\tilde{\lambda}_B$ and ϕ_{vol}. The figure shows that, indeed, for a centric configuration of the colloidal particle in the cell, the force acting on the colloid is always attractive and directed towards the wall. The force-free position for the colloid is therefore expected to lie at some point $z < z_1/2$. This should

be so because the imbalance between $\gamma F(0)$ and $\gamma F(z)$ and thus the net force is largest when the image-charges vanish, i.e. when $\epsilon' = \epsilon$, and that it is zero when $\epsilon' = 0$. The force increases with growing ϵ'/ϵ, with increasing volume fraction and with increasing colloidal charge,

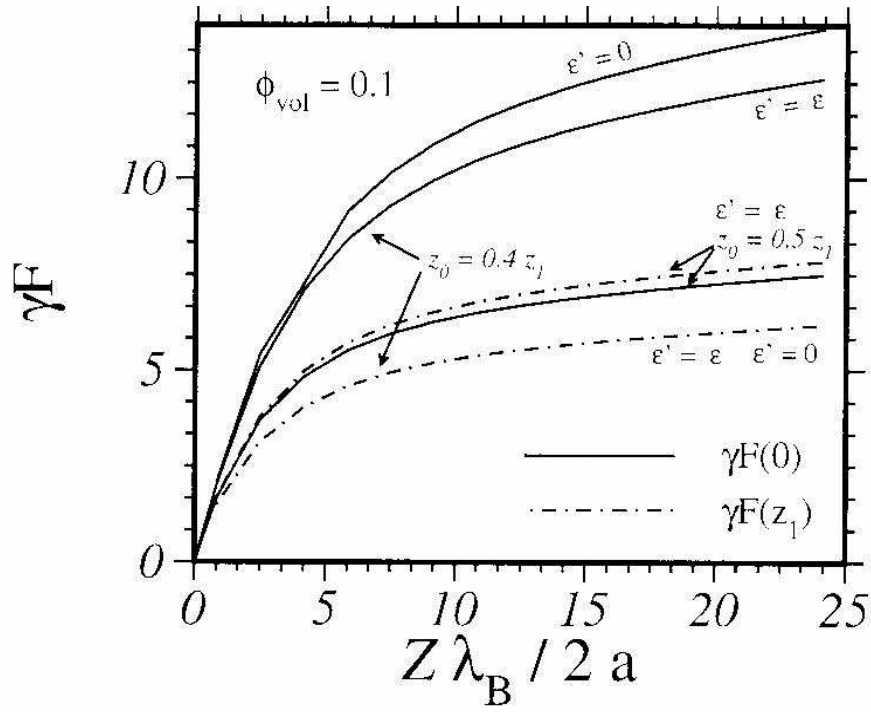

Figure 5.3: The partial forces $\gamma F(0)$ and $\gamma F(z_1)$ acting on the colloid a centric position ($z_0 = 0.5z_1$) and when its center position is shifted to $z_0 \approx 0.4z_1$ (closer to the wall), as a function of the reduced colloidal charge $Z\lambda_B/a$. The net force follows if the force $\gamma F(z_1)$ acting from the bulk side is subtracted from $\gamma F(0)$. In the eccentric case the net force is always positive as against the centric case in Fig. 5.2.

To investigate the full effect of confinement, the colloid is displaced slightly from its centric position. This results to different boundary conditions and a new and more complicated BVP. This is discussed further in Ref. [78, 153]. The result however shows that for wall-colloid distances z_0 a little smaller ($z_0 \approx 0.4z_1$) than half of the mean bulk colloid–colloid distance z_1, the net force on the colloid becomes invariably repulsive due to the strong confinement effect (see Fig 5.3). This holds for all values of ϵ'/ϵ between zero and one, all volume fractions and all scaled colloidal charges $Z\lambda_B/a$. That the latter statement is true even though we stopped at only $Z\lambda_B/2a = 25$, follows from the well-known phenomenon of ion condensation, a typical feature of the nonlinear PB theory [71, 5, 155]. Values for the scaled charges higher than $Z\lambda_B/2a = 25$ will therefore produce no new results.

5.3. The cell model in Monte-Carlo simulation

The PB-BVP and results given in the preceeding sections show that a slight perturbation in the wall–colloid separation distance from a centric position in the interfacial cell results in the net force on the colloidal particle being repulsive. In this section we use a cubic cell in MC simulations to complement the PB results by addressing the effects of the counterions correlation, and whether the results are changed when the counterions are allowed to have a finite core radius, since these cannot be treated within the PB scheme described above. To see how big the finite-size effect can become, we study the extreme situation where the colloid touches the dielectric wall (Fig. 5.4(a)). Here finite-size effects can be expected to be most pronounced because of the spatial confinement of the ions in the narrow region between the colloid and the wall. For counterions with both finite and vanishing core radii, we will calculate the free energy for a colloid in such a touching position and compare it with the free energy for the colloid in a bulk suspension (Fig. 5.4(b)). If this energy difference is positive and only weakly dependent on the counterion size, we may conclude that the results of the PB calculation remain the same even for counterions of finite size. We also follow in the manner of Groot [155] to determine the possible effective charge of an interfacial colloid.

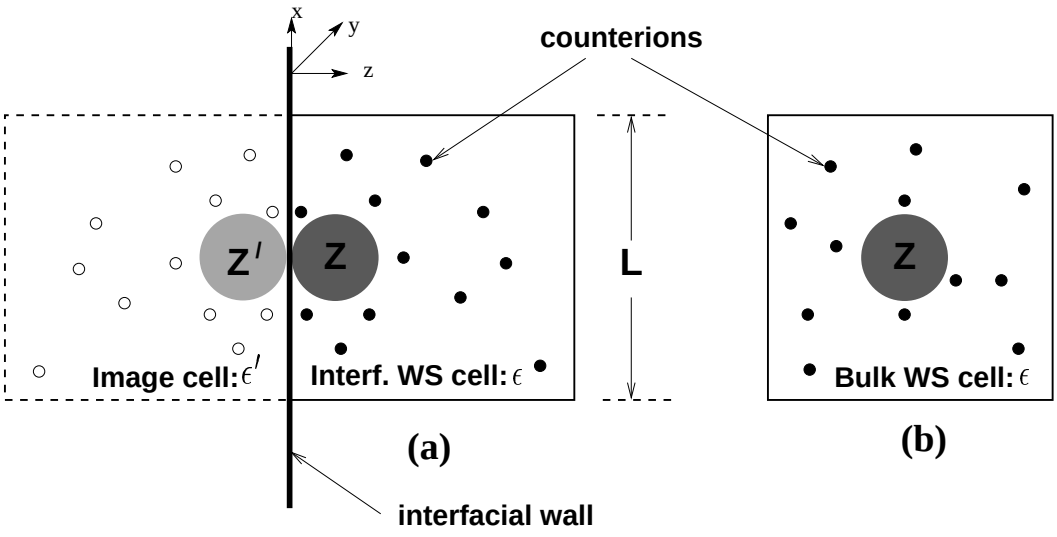

Figure 5.4: The cubic cell model: (a) An interfacial cell containing a colloid of total charge, Z and it cloud of counterions in a medium of dielectric constant, ϵ. The colloid here is shifted along the z-axis from its usual center position to touch the interface wall. The image of the cell is drawn behind the interface (dielectric constant ϵ), showing the colloid image of charge Z' and its image-counterions. (b) A bulk cell, far from the interface wall. There are no images.

5.3.1. Computational details

Our MC simulation setup is based on the cubic cell model — a macroion of radius a and charge Ze in a cubic cell of length L ($x \in [-L/2, L/2]$, $y \in [-L/2, L/2]$, and $z \in [0, L]$) neutralized by inhomogeneously distributed microions and suspended in water of dielectric constant $\epsilon = 78.3$. The cell model MC simulation is usually performed in a fixed configuration of the single macroion while the microions (counterions) are allowed to explore the configuration space. In the bulk situation (Fig. 5.4(b)), it is conventional to fix the macroion at the body center of the cubic cell. Hence we locate the macroion at the Cartesian position $(x, y, z) = (0, 0, L/2)$. We shall call this the Bulk scheme (BS). Here, no dielectric interface is involved and hence no image-charge effects. For a WS cell at the interface (Fig. 5.4(a)), we have the Interface scheme (IS), where the macroion is made to touch the ϵ' dielectric wall at $z = 0$, i.e., its position is at $(0, 0, a)$.

The simulations were performed in the canonical ensemble (constant-NVT) at room temperature corresponding to the Bjerrum length of $\lambda_B = 0.715$nm. The cell volume (and thus L) is determined by the macroion volume fraction $\phi_{vol} = V_m/L^3$. In the following simulations, $\phi_{vol} = 0.01, 0.05, 0.10$ are investigated. We again consider the salt free case where the microions are all monovalent counterions. We have already noticed that the PB equation then scales with $Z\lambda_B/a$. Beyond the mean-field level, this, of course, ceases to be valid, and our MC results will also depend on the ratio λ_B/a. We study values for $\lambda_B/2a$ ranging from $\lambda_B/2a = 0.6$ (small particle) to $\lambda_B/2a = 0.03$ (large particle).

In each scheme, the macroion remains fixed, and the counterions are moved through the cell to sample the configuration space according to the traditional Metropolis algorithm [131]. Periodic boundary condition, minimum image convention or Ewald summation schemes [6, 7] are not applied in summing the Coulomb interactions. This is a consequence of the cell model which assumes that contributions from neighboring cells are negligible. The validity of this approximation has been tested against a periodically repeated system where the Ewald summation scheme was applied [155, 156] and found to be reasonable. In the IS, the situation is similar to an electrolyte confined between a charged and an uncharged planner walls described by Wennerström *et al* [142]

In the BS, the total configurational potential energy of the ions,

$$\beta U = \sum_{i<j} \beta u_{ij}(r_{ij}) \,, \tag{5.20}$$

is averaged over the simulation, calculated in each run using the pair interaction po-

tential ($\beta = 1/k_BT$)

$$\beta u_{ij}(r_{ij}) = u_{ij}^{rep} + \frac{q_i q_j \lambda_B}{r_{ij}}\,, \tag{5.21}$$

where the charge valence q_i is Z ($5 \leq Z \leq 300$) for the macroion and -1 for the counterions. The term u_{ij}^{rep} is the repulsive hard-sphere interaction

$$u_{ij}^{rep} = \begin{cases} \infty & \text{if } r_{ij} < d_{ij} \\ 0 & \text{if } r_{ij} > d_{ij} \end{cases} \tag{5.22}$$

where d_{ij} is the minimum distance of the centers of the i^{th} and j^{th} ions. $d_{ij} = (d_m + d_c)/2$ for a macroion-counterion pair, and $d_{ij} = d_c$, for a counterion-counterion pair, with $d_m = 2a$ being the macroion diameter. The counterion diameter d_c is chosen to be 0.425nm and zero (point-charge).

In the IS system, the electrostatic image-charges of all ions in the solvent have to be taken into account. An ion i with charge $q_i e$ and coordinate (x_i, y_i, z_i) in the positive half-space, $z > 0$, has an image i' located at $(x_i, y_i, -z_i)$ in the ϵ' medium whose charge is $q_i' e = \chi q_i e$ with χ defined in eq. (5.8). These image-charges contribute to the potential in the ϵ medium, hence the total internal energy U, for N real ions in the cell becomes the sum of contributions from the real charges, eq. (5.21), and image-charges (u^{im}). Thus:

$$U = \sum_{i<j} \left[u_{ij}(r_{ij}) + u_{ij}^{im}(r_{ij}) \right] + \sum_i u_i^{im}(z_i) \tag{5.23}$$

where $u_{ij}(r_{ij})$ is the real charge contribution, eq. (5.21),

$$\beta u_{ij}^{im}(r_{ij}) = \frac{\lambda_B \chi q_i q_j}{\left[x_{ij}^2 + y_{ij}^2 + (z_i + z_j)^2 \right]^{1/2}} \tag{5.24}$$

is the real–image pair interaction potential, and

$$\beta u_i^{im}(z_i) = \frac{1}{2} \frac{\lambda_B \chi q_i^2}{2 z_i} \tag{5.25}$$

is the interaction potential of a real charge with its own image (self-image potential energy). The factor $\frac{1}{2}$ that appears explicitly in the self-image energy and implicitly in the $u_{ij}^{im}(r_{ij})$ pair energies is clarified in the following:

Let us consider, for simplicity, only two ions i and j (each having a single charge e) located respectively at $\mathbf{r}_i = (x_i, y_i, z_i)$ and $\mathbf{r}_j = (x_j, y_j, z_j)$ in a medium of dielectric constant ϵ, and close to a wall of dielectric constant ϵ'. This results in the formation of image-charges i' and j' located at $\mathbf{r}_{i'} = (x_i, y_i, -z_i)$ and $\mathbf{r}_{j'} = (x_j, y_j, -z_j)$ respectively

for i and j. Then the relative distances between the ions (real and image) are: r_{ij} for i and j, $r_{ij'}$ for i and j', $r_{i'j}$ for j and i', $r_{ii'} = 2z_i$ between i and i', and finally $r_{jj'} = 2z_j$ between j and j'. The potential ψ at the position of i is;

$$\psi_i \;=\; \frac{e}{\epsilon r_{ij}} + \frac{\chi e}{\epsilon r_{ij'}} + \frac{\chi e}{2\epsilon z_i} \tag{5.26}$$

where $\chi e = e(\epsilon - \epsilon')/(\epsilon + \epsilon')$ is the charge on an image-ion. The first term is due to the real ion j, the second due to its image j' and the third term is from the self image i'. The potential at j is the same as eq. (5.26) except that i and j are interchanged. Therefore the total electrostatic potential energy, $\beta U \;= \frac{\beta}{2}\int \rho\psi \; dV$ for a system of ions now becomes

$$\beta U = \frac{\lambda_B}{r_{ij}} + \frac{\lambda_B \chi}{2}\left(\frac{1}{r_{ij'}} + \frac{1}{r_{i'j}} + \frac{1}{2z_i} + \frac{1}{2z_j}\right) . \tag{5.27}$$

This equation cleanly separates into purely real (first term) and real–image interactions, showing explicitly the factor 1/2 in the real–image interaction. For planar interfaces $r_{ij'} = r_{i'j}$. We can generalize eq. (5.27) for N ions each of charge $q_k e$ in the region ϵ, and find

$$\beta U \;=\; \lambda_B \sum_{i<j}^{N}\left(\frac{q_i q_j}{r_{ij}} + \frac{\chi q_i q_j}{r_{ij'}}\right) + \frac{\lambda_B}{2}\sum_{i=1}^{N}\frac{\chi q_i^2}{2z_i}, \tag{5.28}$$

which is same as eq. (5.23). In eq. (5.28) the factor 1/2 is implicit in the real–image pair interaction and care must be taken to avoid double counting.

The total configurational energies were averaged over the simulation as in the previous scheme. For both schemes, in each MC run, the system was equilibrated for about 45000 - 90000 MC cycles, depending on the Coulomb coupling strength, and averages taken in the next 15000-30000 cycles. One MC cycle here corresponds to an attempted move of all mobile ions in the system. Equilibration was ensured by arriving at roughly the same energy by starting the simulation from a completely random configuration corresponding to infinite temperature, and starting from a condensed configuration of the counterions on the macroions.

For the determination of the effective charge of the macroions, the counterion density, $\rho^*(r)$ in the region between $1.2a$ (a being the radius of the macroion) and the edges of the cell was used. This is similar to the method used by Groot [155]. The scheme is illustrated in Fig. 5.5: (a) for the IS and (b) for the BS. The effective charge Z^* is defined as

$$Z^* = \frac{V_a}{V_b}\int_{|r|>1.2a} \rho^*(r) d^3r, \tag{5.29}$$

where V_a is the volume available to the counterions, V_b is the volume over which the density is integrated in eq. (5.29), and the volume ratio ensures that the effective charge

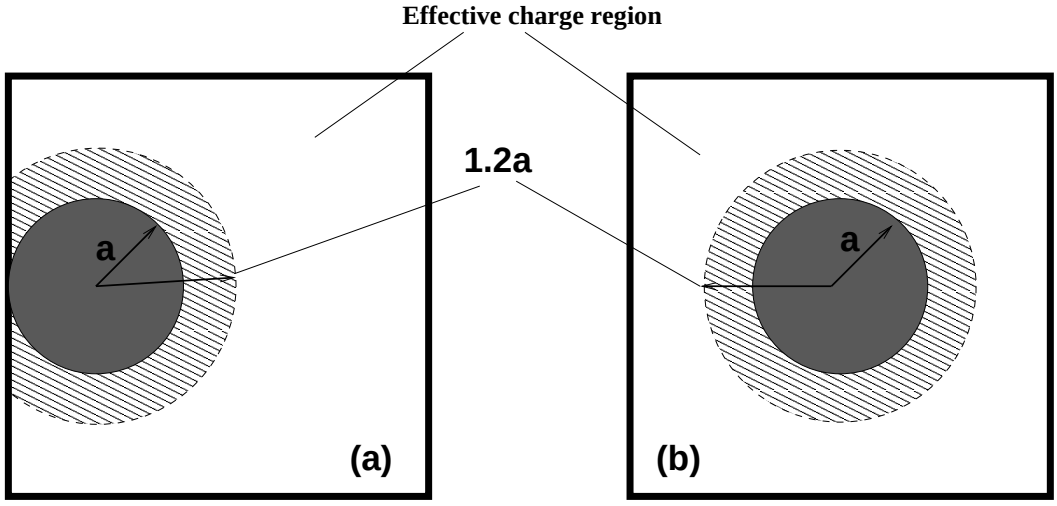

Figure 5.5: The scheme for the effective charge measurement: (a) the Interface scheme (IS) and (b) the Bulk scheme (BS). The effective charge of the macroion (radius a) is determined by the counterion density in the region outside the visual sphere of radius $1.2a$.

Z^* coincides with the bare charge Z for homogeneous density profiles, i.e., for $\lambda_B \to 0$ and $Z \to 0$

5.3.2. Results and discussion: Monte-Carlo/Poisson-Boltzmann

Interaction energies

The scaling of the PB equation with $Z\lambda_B/2a$ has been demonstrated by Groot [155] for the effective macroion charges. Likewise the configurational energy per counterion scales with $Z\lambda_B/2a$ in the sense that $\langle \beta U \rangle / Z = f(Z\lambda_B/2a)$, where f is a unique function and $\langle U \rangle$ is the ensemble average energy. This scaling behavior implies that properties of particles, which simulation is presently out of reach (as for instance, micron particles with $Z \sim 10^4$), can be extrapolated from data of particles that can easily be simulated. For example, if we characterize a system whose coupling strength is $Z\lambda_B/2a = 10$ (i.e $\lambda_B/2a = 0.1, Z = 100.0$), then we can predict the behavior of all systems with the same coupling strength (e.g. $\lambda_B/2a = 0.01, Z = 1000.0$).

Figure 5.6 shows the energy per ion $\langle \beta U \rangle / Z$ against the scaled macroion charge $\lambda_B Z/2a$, in the bulk situation, together with the PB scaling function. In consistence with Groot's observation on effective charges [155], the MC energies gradually move away from perfect scaling shown by PB (which provides the upper limit), as the coupling increases from $\lambda_B/2a = 0.03$ (large particle, $d_m = 23.8$nm in water) to

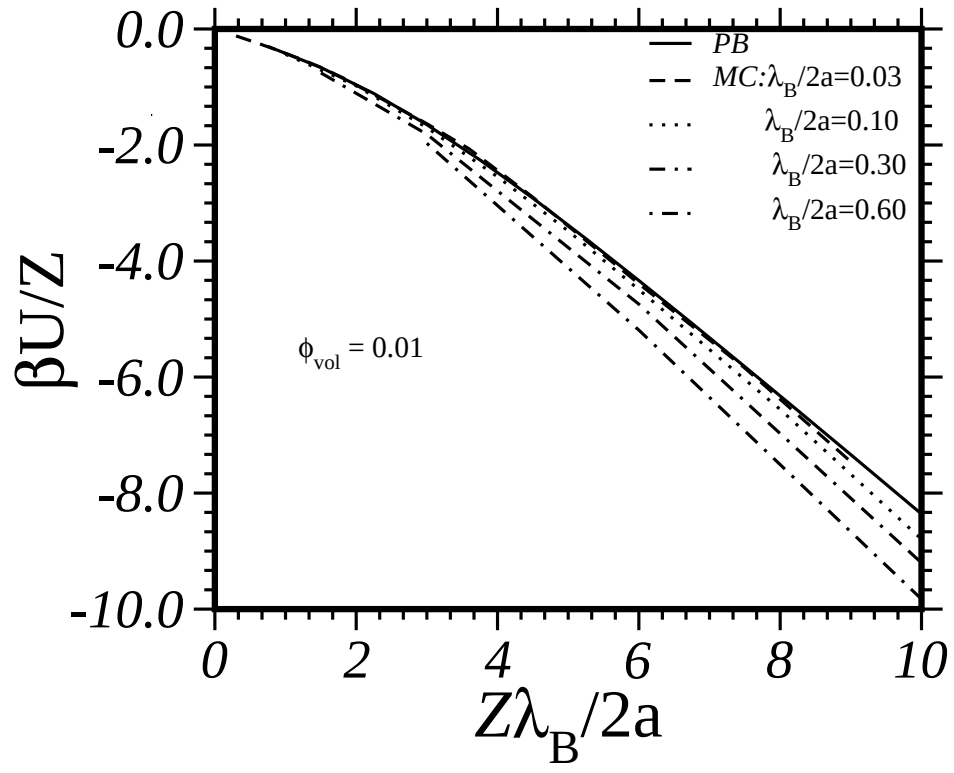

Figure 5.6: The average total internal energy per counterion, $\langle \beta U \rangle / Z$ as a function of the scaled colloidal charge, $Z\lambda_B/2a$. The solid line is the result of the PB cell theory, while the dashed, dotted lines and their combinations are results of MC simulations for the various scaling parameter $\lambda_B/2a$. All points in the figure were obtained at 1% macroion volume fraction.

$\lambda_B/2a = 0.6$ (small particle, $d_m = 1.2$nm). This behavior is due to ion-ion correlation among the counterions which is well accounted for in MC but neglected by PB theory. Fig. 5.6 confirms once more the well-known fact that PB becomes correct in the limit $\lambda_B/a \to 0$.

A more interesting result is the quantity $\Delta\langle \beta U \rangle / Z = (\langle \beta U_{IS} \rangle - \langle \beta U_{BS} \rangle)/Z$ which measures the electrostatic internal energy gain or loss per counterion between the two macroion configuration systems (BS and IS), as a function of $Z\lambda_B/2a$. Figure 5.7(a) shows $\Delta\langle \beta U \rangle / Z$ vs $Z\lambda_B/2a$ for (i) an $\epsilon/\epsilon' = 0.08$ interface (typical of a glass-water interface) and (ii) three macroion volume fractions $\phi_{\rm vol} = 0.01$, 0.05 and 0.10. Figure 5.7(a) shows *negative* $\Delta\langle \beta U \rangle / Z$ values for high $Z\lambda_B/2a$ coupling for all the three ϕ_{vol}. This means that from the purely electrostatic point of view, the situation where the colloid touches the wall can become energetically more favorable than the bulk situation where it is in the center of its cell in an isotropic environment. This result is first surprising considering the large repulsive self-image interaction, eq. (5.25), of

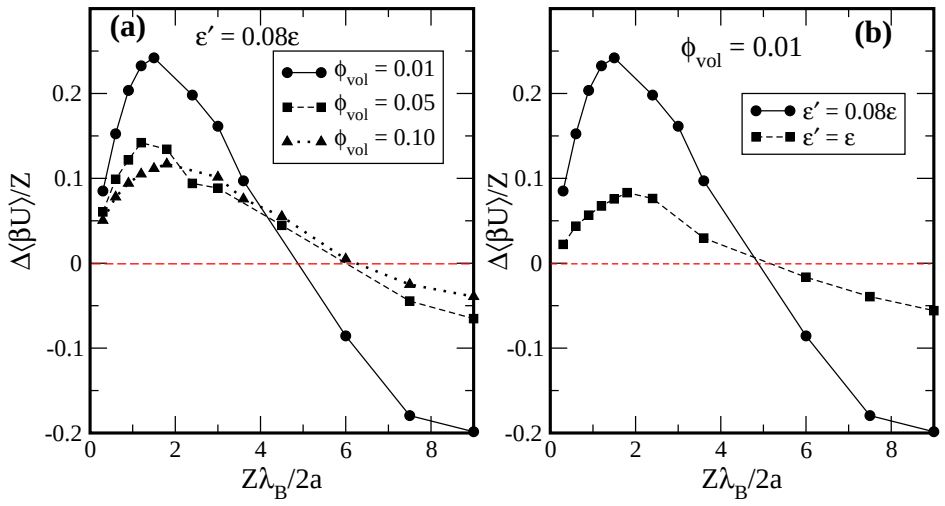

Figure 5.7: The variation of the internal energy difference $\Delta\langle\beta U\rangle/Z$ with the macroion Coulomb coupling parameter $Z\lambda_B/2a$ for a finite counterion diameter $d_c = 4.25$: (a) For $\epsilon' = 0.08\epsilon$ and the volume fraction $\phi_{\rm vol} = 0.01,\ 0.05,\ 0.10$. (b) For a fixed $\phi_{\rm vol} = 0.01,\ \epsilon' = 0.08\epsilon$ and $\epsilon' = \epsilon$.

the colloid in the IS. The crossing-over behavior of $\Delta\langle\beta U\rangle/Z$ with increasing coupling strength can be understood as follows: The positive $\Delta\langle\beta U\rangle/Z$ for small $Z\lambda_B/2a$ is in the regime of small electrostatic coupling, where the density profile is only weakly sensitive to both the position of the colloidal particle and the image-charges. The positive value of $\Delta\langle\beta U\rangle/Z$ is then caused by the strong (unscreened) repulsion of the colloid by its own image. The change of sign of this quantity in the regime of strong electrostatic coupling, on the other hand, can be attributed to the fact that there are much more counterions attracted to the colloidal surface in the IS than in the BS. This is due to the "contact" of the colloid (with charge Z) and its image (with charge χZ) in the wall situation where the counterions are now attracted by a total charge $(1+\chi)Z = 1.85Z$ being much larger than the colloidal charge Z in the BS. The preferred region for these counterions is the wedge region between the colloid surface and the wall where the counterion density is particularly high. The image-charge contribution to the crossing over becomes clear from Fig. 5.7(b) which directly compares $\epsilon'/\epsilon = 0.08$ with $\epsilon'/\epsilon = 1$. In the later, there are no image-charges.

The above analyzes have not accounted for the entropic effect due the inhomogeneous distribution of the counterions in the system. Actual adsorption should be determined from the total free energy. A direct determination of free energy or entropy is not possible from the constant-NVT MC simulations [6, 7]. Nevertheless, we can determine the total free energy difference ΔA from $\Delta\langle\beta U\rangle$ presented above through

the following thermal integration [157]

$$\frac{\Delta A}{Z} = \int_0^{\beta} \frac{\Delta\langle U\rangle}{Z} d\beta' \,, \tag{5.30}$$

which by a change of variables we transform into an integral over the function $f(x) = \Delta\langle\beta U(x)\rangle/Z$ with $x = Z\lambda_B/2a$

$$\frac{1}{Z}\Delta\beta A(Z\lambda_B/2a) = \int_0^{Z\lambda_B/2a} f(x)dx \,. \tag{5.31}$$

The free energy difference as a function of $Z\lambda_B/2a$ is plotted in Fig. 5.8 for: the case $\epsilon'/\epsilon = 0.08$ ($\chi = 0.85$), i.e., when the image-charges are almost fully switched on; two volume fractions, $\phi_{vol} = 0.01,\ 0.10$; and for point-charge ($d_c = 0$) and finite size ($d_c = 4.25$Å). Figure 5.8 reveals that the effect of the finite size of the counterions is relatively small and the free energy difference is always positive for both volume fractions.

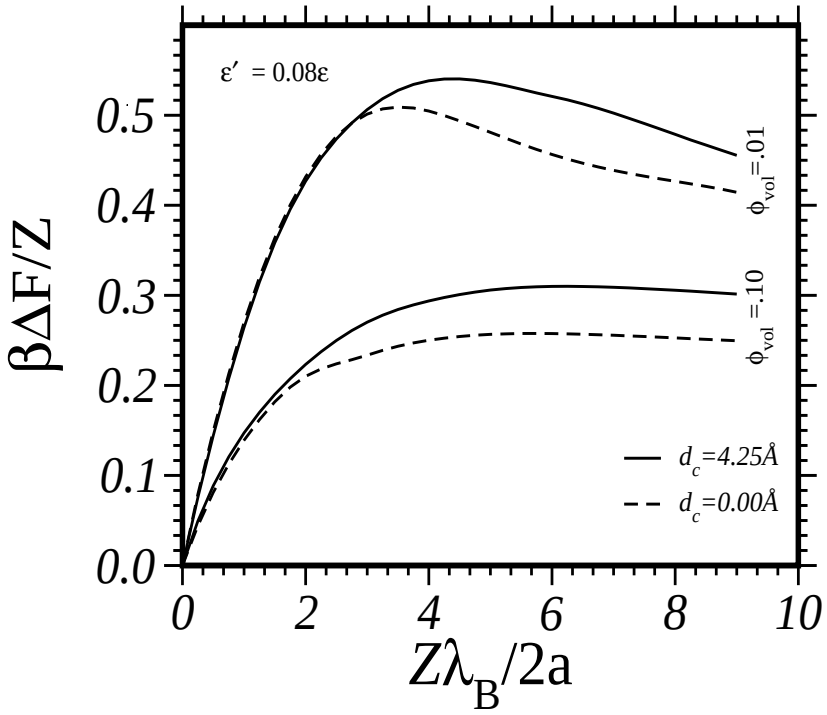

Figure 5.8: The free energy difference per counterion, $\beta\Delta A/Z$, obtained by integrating the $\Delta\langle\beta U\rangle/Z$ of Fig. 5.7. The labels are as defined in Fig. 5.7. The plots show the small but finite effect of the changing the counterions from point-charges to finite size ions.

For the finite size counterions only, Fig. 5.9 shows an extension of the result in Fig. 5.8 to distinct dielectric interfaces, including $\epsilon' \gg \epsilon$ realized for example in the

case of metal-water interfaces. Here is plotted the free energy difference as a function of $Z\lambda_B/2a$ for: three volume fractions and three distinct interfaces namely $\epsilon'/\epsilon = 0.08$, $\epsilon'/\epsilon = 1.0$ (dielectric continuity — no image-charges but confinement) and $\epsilon'/\epsilon = \infty$ (e.g. metal-water interface). While the first two interfaces show positive free energy difference for all ϕ_{vol} as in Fig. 5.8, the later is seen to be negative again for all ϕ_{vol}. In this case ($\epsilon'/\epsilon = \infty$) the image-charges are opposite in sign and equal in magnitude to the real charges in the WS cell. Consequently, point-ions cannot be used, otherwise, ions can collapse on each other to produce unphysically high energies. The height of the repulsive barrier or the depth of attraction as the case may be decreases with increasing volume fraction, ϕ_{vol}. The $\epsilon'/\epsilon = \infty$ interface is however not discussed any further in this chapter.

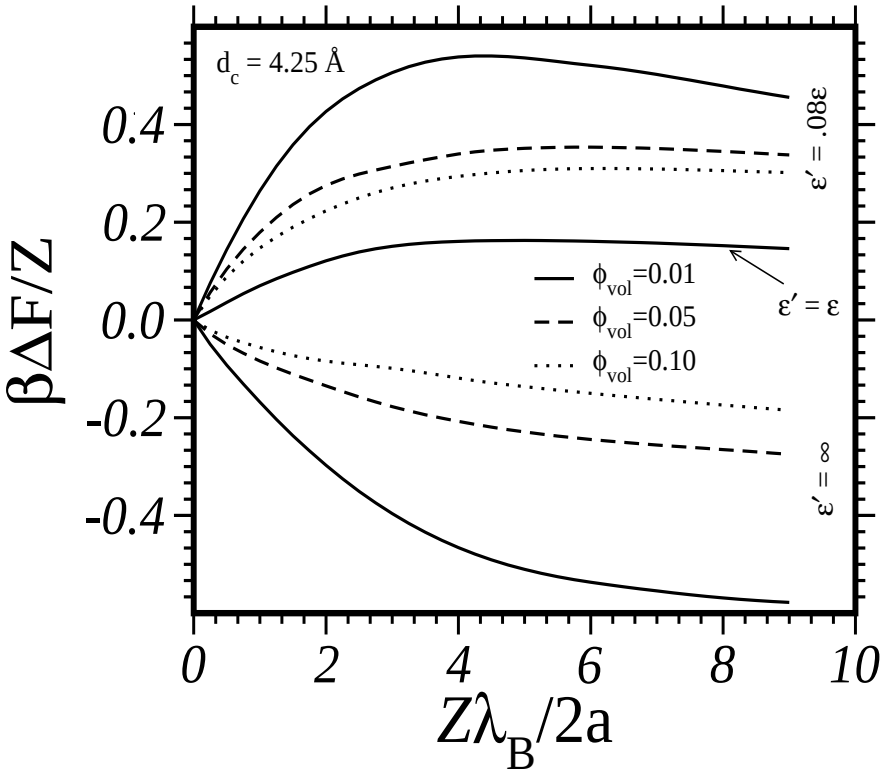

Figure 5.9: The free energy difference per counterion, $\beta\Delta A/Z$, as in Fig. 5.8 for finite size counterions; for various interfaces (ϵ'/ϵ) and volume fractions ϕ_{vol}.

We have seen from Fig. 5.7 that the configurational energy difference for large coupling strength becomes negative. The positive free energy difference of Fig. 5.8 must therefore be due to a negative entropy difference that over-compensates $\Delta\langle\beta U\rangle/Z$. In view of the confinement effect analyzed in the previous section, the explanation

for this can obviously be found in the reduction of counterion entropy due to the distortion of the double layer from its spherical shape when the colloid touches the wall. We thus again end up with the recognition that for small wall–colloid distances this confinement effect is a significant mechanism that hinders the colloid from becoming adsorbed to the wall. Figure 5.8 indicates that this result remains unchanged even if the counterions have finite size. However, in the unlikely limit where the electrostatic internal energy is dominant (vanishing configurational entropy), there exist conditions where the adsorption of the colloid at the wall is favourable, in spite of its own repulsive image-charge.

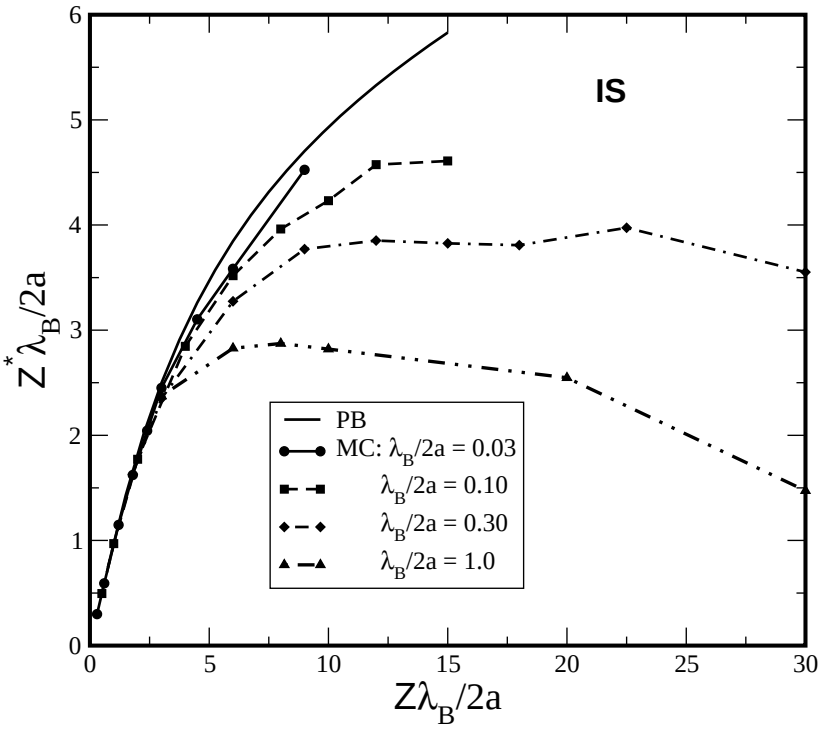

Figure 5.10: The scaled effective charge $Z^*\lambda_B/2a$ against the scaled bare charge $Z\lambda_B/2a$ for various values of $\lambda_B/2a$: 0.03, 0.10, 0.30 and 1.0 in the MC. The PB curve as usual forms the upper limit.

Effective charges

We have estimated the effective charge, Z^* of the macroion for various bare charges, Z, and the coupling parameter $\lambda_B/2a$ using method illustrated in Fig. 5.5. Figure 5.10 shows a plot of scaled effective charge, $Z^*\lambda_B/2a$ against the scaled bare charge $Z\lambda_B/2a$ for various values of $\lambda_B/2a$, in the IS system. The curves are also similar for the BS system. This behaviour of the curves is in qualitative agreement with that of

Groot [155] (spherical cell model), namely, that the effective charge exhibits a maximum rather than a plateau, when the coupling, $\lambda_B/2a$ becomes large.

What is worth pointing out here is how the effective charge of a macroion at the interface (the IS system) Z^*_{IS} compares with the effective charge of the same macroion in the bulk (the BS system) Z^*_{BS}. It turns out, interesting, as shown in Fig. **??**, that Z^*_{IS} becomes smaller than Z^*_{BS} as the bare charge increases for a given coupling. This is also true of the results from the PB cell theory included in the plots.

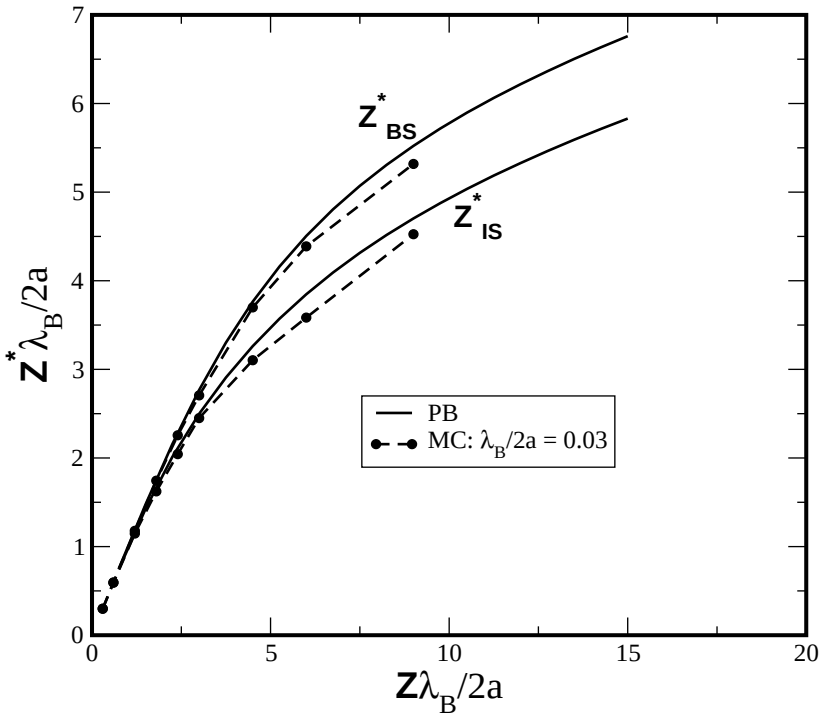

Figure 5.11: Comparison between the effective, $Z^*\lambda_B/2a$ for a macroion in the bulk (Z^*_{BS}) and for the macroion at the interface (Z^*_{IS}) for PB and MC ($\lambda_B/2a = 0.03$).

The explanation of this phenomenon can be viewed in this way: In the IS system, the macroion is pressed to the wall, and hence very close to its own image-charge resulting to a net charge (real plus image) almost double of the real charge for, e.g. the glass-water interface under consideration. Consequently, more counterions are attracted close to the surface of the macroion, in the region $a < r \leq 1.2a$, (Fig. 5.5), thereby increasing the ion density near the macroion surface. This leads to lower effective charge in comparison with the bulk system where there are no image-charges.

5.4. Summary and conclusion

Any charged object in the neighborhood of an interface between media of different dielectric constants, experiences image-charge forces arising from the dielectric discontinuity. In a concentrated suspension of macroions (these can be everything from a globular protein to a simple latex particle), these forces compete with the usual double-layer forces between the macroions. A macroion next to such an interface experience an anisotropic environment: towards the bulk-side it has the next neighbour colloid screened in the usual way by its microions, while towards the wall it sees the image-charge of its own charge and those of its double layer. Since the image-charges in most experimentally relevant cases are weaker than the real charges, this imbalance leads to an attractive wall-induced force on the colloid.

In this chapter, we have been concerned with the question how strong this attraction can become and whether it could overcome, in principle, the confinement-induced repulsion that is due to the distortion of the double-layer through the wall. To answer this question, we have suggested a cell model where the colloid plus its counterions is confined to a finite volume that is just the reciprocal of the colloidal density. The ion distribution inside this cell can then be calculated from the PB equation. Of crucial importance are the boundary conditions at the cell boundaries because it is through them that the physics of the problem come into play. By requiring the electric field to vanish at one side of the cell, while accounting for the dielectric jump at the other, we take account of the anisotropic environment of the interfacial colloid, with there being a colloid in the next neighbor cell, on one side, and an interface, on the other.

In our MC simulation, we have proposed a cell model in cubic approximation of the Wigner-Seitz cell. The centric configuration of the macroion was compared with the situation where the macroion is fixed on the surface of the substrate interface which results in distortion of the counterionic atmosphere around the colloid and maximum effect of surface polarization due to image-charges. Free energy calculation for the class of dielectric interfaces commonly encountered in experiments ($\epsilon' \leq \epsilon$) reveals that this adsorbed configuration of the macroion is never favoured relative to the bulk situation where confinement and image-charge effects are absent. This result holds for both finite-size and point-like counterions. Further application of cell model methods to investigate macroion effective charges show that at the interface (for $\epsilon' < \epsilon$), the effective charges become smaller than the bulk values for large bare charges. Correspondence between the PB and MC results reveals the importance of the counterions correlation not included in the PB schemes.

6

Summary and Outlook

The work presented in this thesis has considered a set of closely related problems bordering on, the effect on charged colloidal spherical particles in microionic solutions, due to the presence of interfacial substrates which often have different dielectric constants as that of the solution. We have considered mainly interaction potentials of these colloids with the interfaces (wall–colloid or interface–colloid potentials) and also interactions among themselves (colloid–colloid potentials) in the presence of one or more similar or dissimilar interfaces. We have also investigated structural and phase behaviour of these interfacial colloids, resulting from the interaction potentials. As tools for our studies, we have worked within the framework of PB theories and MC simulations. While we have obtained interesting and useful results in the various studies carried out, it is necessary to point out some shortcomings and possible ways of improvement in future studies.

In chapters 2 and 3, the wall–colloid interaction potentials obtained are considered "effective" in the sense that they considered interaction of an interfacial wall with just a single colloidal particle in a medium that in reality hosts other interacting colloids. While the effective potentials can be useful as we have shown from the agreement with experiment (Fig. 2.13), a lot still remains to be done to include the many-body effects present in actual colloidal suspensions. The cell model approximation method presented in chapter 5, which is supposed to take care of the many-body effects, is itself based on assumptions which are hardly satisfied in colloidal suspensions. They include mainly, that every colloidal macroion has the same environment, which can only be true in crystalline order of the macroions. A more accurate technique of many-body description of a colloidal suspension termed Poisson-Boltzmann — Molecular dynamics

(PB-MD) hybrid method has been suggested [78]. This method essentially combines a continuous PB description of the electrolyte microions with a MD simulation of the colloidal macroions: One solves the PB equation in an electrolyte solution of microions for a fixed colloidal configuration $\{\mathbf{R}\}$ and in the external field of the macroions, from which the net force on each macroion is deduced. This force is then used in a MD simulation to generate a new configuration. The force calculated in this manner is expected to be superior to the pair-force commonly used in the one-component system. The one significant flaw of the method (PB-MD hybrid) is the neglect of correlation between the microions which is a characteristic of mean-field PB theories. Dobnikar *et al* [158] have applied this hybrid method to plot the solid – liquid phase diagram of charge stabilized colloidal suspensions. Further studies are therefore suggested with the PB-MD hybrid method, with extension to the interfacial regions where additional image-charge forces are expected to play important roles.

Chapter 3 dealt with the effective interaction of the single colloidal macroion with specifically an air-water interface which can be penetrated by the colloid. We discussed how an electrostatic double layer *adsorption* barrier (barrier to pushing the colloid from the bulk solution to the interface) resulting from such interaction can be lowered considerably by increased salt concentration, to initiate trapping by surface tension forces at the interface. We also conceptualized an 'electrostatic trap' in the sense that calculated electrostatic *desorption* barriers, (barrier to pushing the colloid from interface back to the solution) are much larger than the adsorption barriers, for the same set of system parameters. Within the validity of the effective potentials used in arriving at these conclusions, our results are correct and reliable as far as the colloid is still in the solvent (water), i.e. there is indeed an electrostatic energy barrier to the approach of the colloid in water to the air-water interface. But the analysis so far, as the charged colloid emerges at the air-water interface still leaves much to be desired. We have analyzed the electrostatic and surface tension forces without; (a) accurate description of the detailed discharging mechanism of the de-wetting part of the particle's surface as it pops to the interface, if at all discharging occurs, and (b) realistic description of the meniscus, following the deformability of the air-water interface. These should be done in future studies, and only then can we be certain that the observed stability of colloidal particles trapped at the air-water interface is due mainly to surface tension forces as we have been led to conclude in chapter 3.

Finally, in chapter 4, within the linear DH theory, we have considered the pair interaction potentials of charged colloidal particles assumed trapped at the air-water interface. We found that introducing additional substrate interfaces parallel and very close to the air-water interface can affect the pair potentials in a particular way, depending on the dielectric constant of the substrate relative to water. We then applied

the pair potentials in a one-component Monte Carlo simulation to obtain fluid – crystal phase diagrams in the $[L : \phi_{\text{surf}}]$ parameter plane, where L is the separation distance between the two interfaces and ϕ_{surf} is the surface fraction of the interfacial colloid. The main result is as follows: A substrate, e.g. air whose dielectric constant is much smaller than that of solvent, e.g. water, enhances the repulsive pair interaction and consequently induces crystallization with decreasing L at densities where the system particles exhibits fluid order in the absence of the substrate. A substrate, e.g. metal whose dielectric constant is much larger than that of the solvent behaves in the opposite way. The investigation was also extended to parameters appropriate for globular proteins with the result that the substrate, if of the former type can facilitate crystallization only when L becomes very thin, being comparable to the protein particle size, and at much higher surface fractions (Fig. 4.11).

However, while these results are insightful and correct at the macroion and salt concentrations investigated, the real picture may be different at extreme densities. At very high densities, the van-der-Waals attractive forces must be included, especially when the particles are very close to a substrate of the metal type where the electrostatic interaction appears to vanish. At very low macroion densities, when the average separation distances between the particles are so large that both the van-der-Waals and electrostatic forces become vanishingly weak, lateral capillary forces which are known to be long-ranged [159], should be taken into account. The lateral capillary

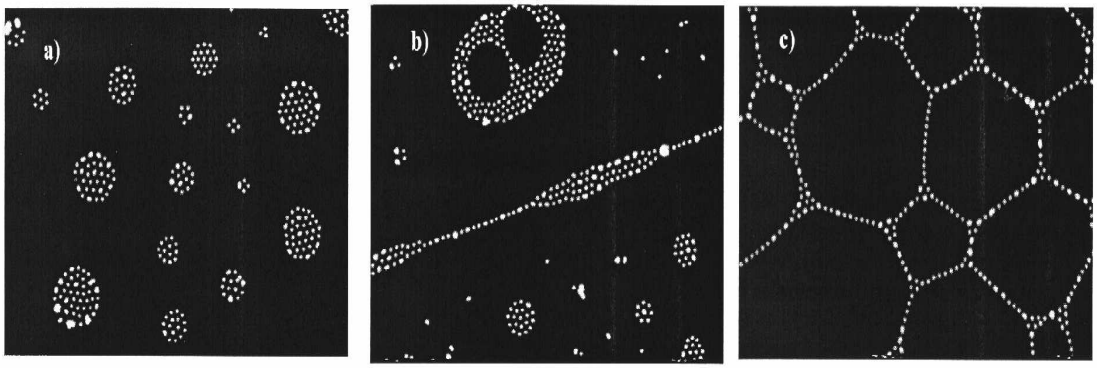

Figure 6.1: Optical microscopy images of (a), (b) clusters, voids, and chains and (c) foam-like structures formed by 1 μm colloidal particles at the air-water interface

interactions can result from the weight or the wetting of particles at the interface, and are known to be attractive for two similar particles on a liquid interface [160, 118, 120]. Such an attractive interaction will result in a secondary minimum in the total interaction potential (DLVO plus capillary) at large pair distances. Recently, Majía-Rosales *et al* [161] have used model square potentials to demonstrate via computer simulations,

that the depth and range of such secondary minima may be responsible for the various 2D arrays of colloidal particles observed at the air-water interface, in addition to just the isotropic-fluid and crystal orders that result from our model potentials. Some of these 2D arrays are shown in Fig. 6.1 taken from Ref. [161]. It is therefore necessary in future studies, to look at specific systems and make accurate description of meniscus formation and wetting properties of the particles for any hope of accurate interpretation of experimental observations and data.

The most basic deficiency of most of the studies reported here is the use of the PB mean-field theory itself. As has been mentioned at various points, this theory totally neglects the interionic correlations. The effect of this neglect has been demonstrated in Fig. 5.6, where we have compared energies calculated from the primitive MC simulation model and from the PB theory in the salt-free limit. In this limit the PB energies scale with the coupling parameter λ_B/a. The comparison in the figure confirmed the fact that the mean-field PB theory becomes correct in the limit of low electrostatic coupling ($\lambda_B/a \to 0$). The accuracy of the results presented should therefore be subject to this limit.

Acknowledgments

I would like to thank Prof. Dr. Rudolf Klein for giving me the opportunity to work in his group (LS Klein) and for his continued support. I am immensely grateful to PD Dr. Hans-Hennig von Grünberg for his kind understanding and very close supervision of this work. I thank my colleagues in the LS Klein group: Cartsen Russ, Christian Fleck, Jure Dobnikar, all who read parts the manuscript; Yong Chen, Uli Herz and of course the secretary, Marianne Griesser for their various assistance. Giorgio Pastore, Haiyan Zhang, Annie Wakata and many other friends are gratefully acknowledged for special encouragements.

I am also very grateful to Tania Simeoni for being by me all the time, and my family in Nigeria especially my mother Priscilla who remained in warm contact. I salute the memory of my late father, Martin whose love and words to me still live. Finally, I thank my God for his love and mercy.

References

1. J.T.G. Overbeek, *Colloid and surface chemistry* (MIT CAES, Massachusetts, 1985), Vol. 1.

2. E.J.W. Verwey and J.T.G. Overbeek, *Theory of the stabilty of lyophobic colloids: The interaction of sol particles having an electric double layer* (Elsevier, Amsterdam, 1948).

3. J.N. Israelachvili, *Intermolecular and surface forces* (Academic Press, London, 1992).

4. R. Klein, *Colloids as model systems for condensed matter physics* (Summerschool lectures, August, 1999).

5. S. Alexander, P.M. Chaikin, P. Grant, G.J. Morales, and P. Pincus, J. Chem. Phys. **80**, 5776 (1984).

6. M.P. Allen and D.J.Tildesley, *Computer simulation of liquids* (Clarendon Press, Oxford, 1987).

7. D. Frenkel and B. Smit, *Understanding molecular simulation* (Academic Press, London, 1996).

8. K.S. Schmitz, *Macroions in solution and colloidal Suspension* (VCH, New York, 1993).

9. D. Evans and H. Wennerström, *The Colloidal Domain: Where Physics, Chemistry, Biology, and Technology Meet* (VCH, New York, 1994).

10. G. Nägele, Phys. Rep. **272**, 215 (1996).

11. A.K. Arora and B.V.R. Tata, *Ordering and Phase Transitions in Charged Colloids* (VCH Publishers, New York, 1996).

12. P. Pieranski, Phys. Rev. Lett. **45**, 569 (1980).

13. A.J. Hurd, J.Phys. A: Math. Gen. **18**, L1055 (1985).

14. R. Kesavamoorthy, M. Rajalakshmi, and B.C. Rao, J.Phys.: Condens. Matter **1**, 7149 (1989).

15. R. Kesavamoorthy, M. Rajalakshmi, and B.C. Rao, J.Phys.: Condens. Matter **3**, 7973 (1991).

16. R. Kesavamoorthy, C.B. Rao, and B. Raj, J.Phys.: Condens. Matter **5**, 8805 (1993).

17. S. Tandon, R. Kesavamoorthy, and S.A. Asher, J. Chem. Phys. **109**, 6490 (1998).

18. W. Firshein, Annu. Rev. Microbiol. **43**, 89 (1989).

19. I.M. Verma and N. Somia, Nature **389**, 239 (1997).

20. J.P. Behr, Bioconjugate Chem. **5**, 382 (1994).

21. B. Maier and J.O. Rädler, Phys. Rev. Lett. **82**, 1911 (1999).

22. J.O. Rädler, I. Koltover, T. Salditt, and C.R. Safinya, Science **275**, 810 (1997).

23. I. Gambu and B. Roux, J. Phys. Chem. **B 101**, 6066 (1997).

24. K.E. Forsten, R.E. Kozack, D.A. Lauffenburger, and S. Subramaniam, J. Phys. Chem. **98**, 5580 (1994).

25. E. Allahyarov, I. DAmico, and H. Löwen, Phys. Rev. Lett. **81**, 1334 (1998).

26. D. Goulding and J-P. Hansen, Mol. Phys. **95**, 649 (1998).

27. D. Goulding and J-P. Hansen, Europhys. Lett. **46**, 407 (1999).

28. W.R. Bowen and A.O. Sharif, Nature **393**, 663 (1998).

29. J.C. Neu, Phys. Rev. Lett. **82**, 1072 (1999).

30. G.M. Kepler and S. Fraden, Phys. Rev. Lett. **73**, 356 (1994).

31. J.C. Crocker and D.G. Grier, Phys. Rev. Lett. **77**, 1897 (1994).

32. D.G. Grier, Nature **393**, 621 (1998).

33. A.J. Hurd and D.W. Schaefer, Phys. Rev. Lett. **54**, 1043 (1985).

34. G.Y. Onoda, Phys. Rev. Lett. **55**, 226 (1985).

35. F. Ghezzi and J.C. Earnshaw, J.Phys.: Condens. Matter **9**, L517 (1997).

36. J. Ruiz-Garcia, R. Gamez-Corrales, and B. Ivlev, Physica **A 236**, 97 (1997).

37. H. Yoshimura, M. Matsumoto, S. Endo, and K. Nagayama, Ultramicroscopy **32**, 265 (1990).

38. W.B. Russel, D.A. Saville, and W.R. Schowalter, *Colloidal Dispersions* (Cambridge University Press, Cambridge, 1989).

39. H. Löwen and J-P. Hansen, Annu. Rev. Phys. Chem. **51**, 209 (2000).

40. F.H. Stillinger, J. Chem. Phys. **35**, 1584 (1961).

41. A.E. Larsen and D.G. Grier, Nature **385**, 230 (1997).

42. M.D. Carbajal-Tinoco, G. Cruz de León, and J.L. Arauz-Lara, Phys. Rev. E **56**, 6962 (1997).

43. G. Cruz de León and J.L. Arauz-Lara, Phys. Rev. E **59**, 407 (1999).

44. E. Allahyarov, I. DAmico, and H. Löwen, Phys. Rev. E **60**, 3199 (1999).

45. J.E. Sader and D.Y.C. Chan, J. Colloid Interface Sci. **213**, 268 (1999).

46. J.E. Sader and D.Y.C. Chan, Langmuir **16**, 324 (2000).

47. E. Trizac and J.L. Raimbault, Phys. Rev. E **60**, 6530 (1999).

48. E.R. Dufresne, T.M. Squires, M.P. Brenner, and D.G. Grier, Phys. Rev. Lett. **85**, 3317 (2000).

49. T. Sladitt, I. Koltover, J. Rädler, and C.R. Safinya, Phys. Rev. Lett. **79**, 2582 (1997).

50. K. Wagner, D. Harris, V. Kahl S. May, J.O. Rädler, and A. Ben-Shaul, Langmuir **26**, 303 (2000).

51. P. Sens and J.F. Joanny, Phys. Rev. Lett. **84**, 4862 (2000).

52. F. Luo D.C. Prieve and F Lanni, Faraday Discuss. Chem. Soc. **83**, 297 (1987).

53. J.Y. Walz, Curr. Opin. Colloid Interface Sci. **2**, 600 (1997).

54. D.C. Prieve, S.G. Bike, and N.A. Frej, Faraday Discuss. Chem. Soc. **90**, 209 (1990).

55. D.C. Prieve and N.A. Frej, Langmuir **6**, 396 (1990).

56. S.G. Bike and D.C. Prieve, Int. J. Multiphase Flow **16**, 727 (1990).

57. M.A. Brown and E.J. Staples, Langmuir **6**, 1260 (1990).

58. S.K. Robertson, A.F. Uhrick, and S.G. Bike, J. Colloid Interface Sci. **202**, 208 (1998).

59. J.C. Earnshaw, J.Phys. D. appl. Phys. **19**, 1863 (1986).

60. D. Haughey and J.C. Earnshaw, Colloid Surf. A **106**, 237 (1996).

61. A. van Blaaderen and P. Wiltzius, Science **270**, 1177 (1995).

62. D.G. Grier and C.A. Murray, J. Chem. Phys. **100**, 9088 (1991).

63. S.L. Carnie and D.Y.C. Chan, J. Colloid Interface Sci. **155**, 297 (1993).

64. S.L. Carnie and D.Y.C. Chan, J. Colloid Interface Sci. **161**, 260 (1993).

65. S.L. Carnie, D.Y.C. Chan, and J.S. Gunning, Langmuir **10**, 2993 (1994).

66. S.L. Carnie, D.Y.C Chan, and J. Stankovich, J. Colloid Interface Sci. **165**, 116 (1994).

67. J. Stankovich and S.L. Carnie, Langmuir **12**, 1453 (1996).

68. J.E. Sader, S.L. Carnie, and D.Y.C. Chan, J. Colloid Interface Sci. **171**, 46 (1995).

69. P. Warszynski and Z. Adamczyk, J. Colloid Interface Sci. **187**, 283 (1997).

70. S. Bhattacharjee and M. Elimelech, J. Colloid Interface Sci. **193**, 273 (1997).

71. L. Belloni, Colloids Surf. **A 140**, 227 (1998).

72. L. Belloni, J.Phys.: Condens. Matter **12**, R549 (2000).

73. P. Moon and D.E Spencer, *Field theory handbook*, 2nd ed. (Springer, NY, 1971).

74. L.N. McCartney and S.J. Levine, J. Colloid Interface Sci. **30**, 345 (1969).

75. J.E. Ledbetter, T.L. Croxton, and D.A. McQuarrie, Can. J. Chem **59**, 1860 (1981).

76. E.N. Houstis, W.F. Mitchell, and T.S. Papatheodorou, Int. J. Numer. Methods Eng. **19**, 665 (1983).

77. E.N. Houstis, W.F. Mitchell, and J.R. Rice, ACM Trans. Math. Software **11**, 379 (1985).

78. H. H. von Grünberg, *Charged colloids at interfaces and in suspension* ((Habilitation thesis), University of Konstanz, 2001).

79. R.R. Netz, Phys. Rev. E **60**, 3174 (1999).

80. R.R. Netz and H. Orland, Europhys. Lett. **45**, 726 (1999).

81. R.R. Netz, Eur. Phys. J. **E 3**, 131 (2000).

82. R.R. Netz and H. Orland, Eur. Phys. J. **E 1**, 203 (2000).

83. A.B. Glendinning and W.B. Russel, J. Colloid Interface Sci. **93**, 95 (1983).

84. E. Schmutzer, Z. Phys. Chem. **204**, 131 (1955).

85. E. Durand, *Electrostatique* (Masson, Paris, 1966), Vol. III.

86. S.L. Carnie and G.M. Torrie, in *Adv. Chem. Phys.*, edited by I. Prigogine and S.R. Rice (Wiley, New York, 1987), Vol. 56, p. 141.

87. C. Wagner, Physik. Z. **25**, 474 (1924).

88. L. Onsager and N.N.T. Samaras, J. Chem. Phys. **2**, 528 (1934).

89. S.A. Palkar and A.M. Lenhoff, J. Colloid Interface Sci. **165**, 177 (1994).

90. H.H. von Grünberg, L. Helden, P. Leiderer, and C. Bechinger, J. Chem. Phys. **114**, 10094 (2001).

91. R.K. Kalia and P. Vashishta, J. Phys. C **14**, L643 (1981).

92. T. Terao and T. Nakayama, Phys. Rev. E **60**, 7157 (1999).

93. D.J. Robinson and J.C. Earnshaw, Phys. Rev. A **46**, 2045 (1992).

94. J. Ruiz-Garcia and B. Ivlev, Mol. Phys. **95**, 371 (1998).

95. T. Watanabe, M. Shiga, K. Asai, and K. Ishigure, Mol. Crys. and Liqu. Crys. **327**, 135 (1999).

96. K.Zahn and G. Maret, Phys. Rev. Lett. **85**, 3656 (2000).

97. T. Sengupta and S. Damodaran, Langmuir **14**, 6457 (1998).

98. F. MacRitchie, in *Physical Chemistry of Biological Interfaces*, edited by A. Baszkin and W. Norde (Marcel Dekker, New York, 2000).

99. S.R. Chetan and D. Srinivasan, Langmuir **16**, 9468 (2000).

100. W.A. Weyl, J.Colloid Sci. **6**, 389 (1951).

101. R.J. Good, J.Phys Chem **61**, 810 (1957).

102. A. Frumkin, Electrochim. Acta **2**, 351 (1960).

103. J.R. Farrel and P.J. McTique, J. Electroanal. Chem **139**, 37 (1982).

104. W.A. Ducker, Z. Xu, and J.N. Israelachvili, Langmuir **10**, 3279 (1994).

105. A. Parsegian, Nature **221**, 844 (1969).

106. M. Quesada-Perez, A. Moncho-Jorda, F. Martinez-Lopez, and Hildalgo-Alvarez, J. Chem. Phys. **115**, 10897 (2001).

107. F. MacRitchie and A.E. Alexander, J. Colloid Sci. **18**, 464 (1963).

108. O. I. Vinogradova, G.E. Yakubov, and H.J. Butt, J. Chem. Phys. **114**, 8124 (2001).

109. D.Y.C. Chan, R.R. Dagastine, and L.R. White, J. Colloid Interface Sci. **236**, 141 (2000).

110. M.L. Fielden, R.A. Hayes, and J. Ralston, Langmuir **12**, 3721 (1996).

111. H.-J. Butt, J. Colloid Interface Sci. **166**, 109 (1994).

112. M. Preuss and H.-J. Butt, Langmuir **14**, 3164 (1998).

113. B. Löhle and R. Klein, Physica **A 235**, 224 (1997).

114. H. Yoshimura, S. Endo, M. Matsumoto, K. Nagayama, and Y. Kagawa, J. Biochem. **106**, 958 (1989).

115. K. Nagayama, in *Adv. in Biophys.*, edited by Setsuro Ebashi (Elsevier, Limerick, 1997), Vol. 34, p. 3.

116. E.E. Uzgiris and R.D. Kornberg, Nature **301**, 125 (1983).

117. F.C. Meldrun, B.R. Heywood, and S. Mann, Science **257**, 522 (1992).

118. P.A. Kralchevsky and N.D. Denkov, Curr. Opinion Colloid Interf. Sci. **6**, 383 (2001).

119. P.A. Kralchevsky and K. Nagayama, *Particles at fluid interfaces and membranes: attachment of colloid particles and proteins to interfaces and formation of two dimensional arrays* (Elsevier, Amsterdam, 2001).

120. P.A. Kralchevsky and K. Nagayama, Adv. Colloid Interf. Sci. **85**, 145 (2000).

121. R. Aveyard, J.H. Clint, and V.N. Paunov, Langmuir **16**, 1969 (2000).

122. A.S. Dimitrov, T. Takahashi, K. Furusawa, and K. Nagayama, J. Phys. Chem. **100**, 3163 (1996).

123. T. Takahashi, A.S. Dimitrov, and K. Nagayama, J. Phys. Chem. **100**, 3157 (1996).

124. K. Zahn, R. Lenke, and G. Maret, Phys. Rev. Lett. **82**, 2721 (1999).

125. P.A. Kralchevsky and K. Nagayama, Langmuir **10**, 23 (1994).

126. F. Martinez-Lopez, M.A. Cabrerizo-Vilchez, and R. Hidalgo-Alvarez, J. Colloid Interface Sci. **232**, 303 (2000).

127. E. Chang and D Hone, J. Phys. France **49**, 25 (1988).

128. H. Löwen, J.Phys.: Condens. Matter **4**, 10105 (1992).

129. J. Chakrabarti and H. Löwen, Phys. Rev. E **58**, 3400 (1998).

130. S.L. Carnie and D.Y.C. Chan, Mol. Phys. **51**, 1046 (1984).

131. N. Metropolis, A.W. Rosenbluth, M.N. Rosenbluth, A.N. Teller, and E. Teller, J. Chem. Phys. **21**, 1087 (1953).

132. D.R. Nelson and B.I. Halperin, Phys. Rev. B **19**, 2457 (1979).

133. M.S.S. Challa, D.P. Landau, and K. Binder, Phys. Rev. B **34**, 1841 (1986).

134. H. Weber, D. Marx, and K. Binder, Phys. Rev. B **51**, 14636 (1995).

135. A.H. Marcus and S.A. Rice, Phys. Rev. E **55**, 637 (1996).

136. J.J. Bergers *et al*, Biochemistry **32**, 4641 (1993).

137. T. Furuno, H. Sasabe, and K.M. Ulmer, Thin Solid Films **180**, 23 (1989).

138. H. Yoshimura, T. Scheybani, W. Baumeister, and K. Nagayama, Langmuir **10**, 3290 (1994).

139. T.L. Hill, *Statistical Mechanics* (Addison-Wesley, MA, 1960).

140. T. Alfrey, P. Berg, and H.J. Morawetz, J. Polym. Sci. **7**, 543 (1951).

141. R. M. Fuoss, A. Katchalsky, and S. Lipson, Proc. Natl. Acad. Sci. USA **37**, 579 (1951).

142. H. Wennerström, B. Jönsson, and P. Linse, J. Chem. Phys. **76**, 4665 (1982).

143. M. le Bret and B. H. Zimm, Biopolymers **23**, 287 (1984).

144. M. Deserno and H.H. von Grunberg, Phys. Rev. E **66**, 11401 (2002).

145. P. Linse, J. Chem. Phys. **93**, 1376 (1990).

146. P. Linse and Lobaskin, Phys. Rev. Lett. **83**, 4208 (1999).

147. P. Linse and Lobaskin, J. Chem. Phys. **112**, 3917 (2000).

148. P. Linse, J. Chem. Phys. **113**, 4359 (2000).

149. V. Lobaskin, A.Lyubartsev, and P. Linse, Phys. Rev. E **63**, 20401 (2001).

150. H.H. von Grünberg, J. Colloid Interface Sci. **219**, 339 (1999).

151. H.H. von Grünberg and L. Belloni, Phys. Rev. E **62**, 2493 (2000).

152. H.H. von Grünberg, R. van Roij, and G. Klein, Europhys. Lett. **55**, 580 (2001).

153. H.H. von Grünberg and E.C. Mbamala, J.Phys.: Condens. Matter **12**, 10349 (2000).

154. J.L. Barrat and J.F. Joanny, Adv. Chem. Phys. **94**, 1 (1996).

155. R.D. Groot, J. Chem. Phys. **95**, 1919 (1991).

156. M.J. Stevens, M.L. Falk, and M.O. Robbins, J. Chem. Phys. **104**, 5209 (1996).

157. R.A. Marcus, J. Chem. Phys. **23**, 157 (1955).

158. J. Dobnikar, R. Rzehak, and H.H. von Grünberg, Submitted to Europhys. Lett. (2002).

159. D. Stamou, C. Duschl, and D. Johannsmann, Phys. Rev. E **62**, 5263 (2000).

160. D.Y.C. Chan, J.D. Henry, and L.R. White, J. Colloid Interface Sci. **79**, 410 (1981).

161. S.J. Mejía-Rosales, A. Gil-Villegas, B.I. Ivlev, and J Ruiz-Garcia, J.Phys.: Condens. Matter **14**, 4795 (2002).